Doctoral Dissertation

Surface Modification of Quantum Dots for the Improvement of Their Photoluminescence Properties

Manunya Tepakidareekul

June 2023

Department of Applied Chemistry

Graduate School of Engineering

Osaka University

Surface Modification of Quantum Dots for the Improvement of Their Photoluminescence Properties

(発光特性向上を目的とした量子ドットの表面処理)

2023

Manunya Tepakidareekul

Department of Applied Chemistry

Graduate School of Engineering

Osaka University

Prefaces

The studies presented in this thesis were carried out during 2017–2022 under the guidance of Professor Dr. Susumu Kuwabata at Department of Applied Chemistry, Graduate School of Engineering, Osaka University.

The objective of this thesis is to improve photoluminescence performances of cadmium-free semiconductor quantum dots, which include quantum dots of carbon and the groups 11–13–16 materials via surface modifications. This study explores new synthesis methods, photochemical properties, and surface chemistry of these materials. The author hopes that information obtained in this study will contribute to the further development of science and technology, especially in the field of nanomaterials.

Manunya Tepakidareekul

Department of Applied Chemistry,
Graduate School of Engineering,
Osaka University
Suita, Osaka,
Japan

June 2023

Content

General Introduction

It has been 30 years since research on low-dimensional semiconductors led to the concept of "artificial atoms", or quantum dots (QDs), which have discrete electronic energy levels like isolated atoms.[1,2] In QDs, as shown in Figure 1, the continuous band structure characteristic of bulk semiconductors becomes partially discrete, resulting in differences in chemical and physical properties compared to the bulk. The quantum confinement effect plays a crucial role in determining their band gap energies. Thereby, the optical properties of QDs can be easily tuned by controlling their size, as well as compositions.[3,4] A variety of potential applications of QDs have been proposed, including display, lighting, bioimaging, and chemosensing technologies.[5–7] Although QDs are now well-known materials, development in their synthesis, characterization, and applications remain very active. Whereas early research of QDs has focused on the groups 12–16 semiconductors, alternative materials have been developed to overcome the high toxicity of the group 12 elements, such as cadmium and mercury. Currently, not only groups 13–15 and 11–13–16 compounds but also lead halide perovskite and carbon nanomaterials have become candidates for QDs.

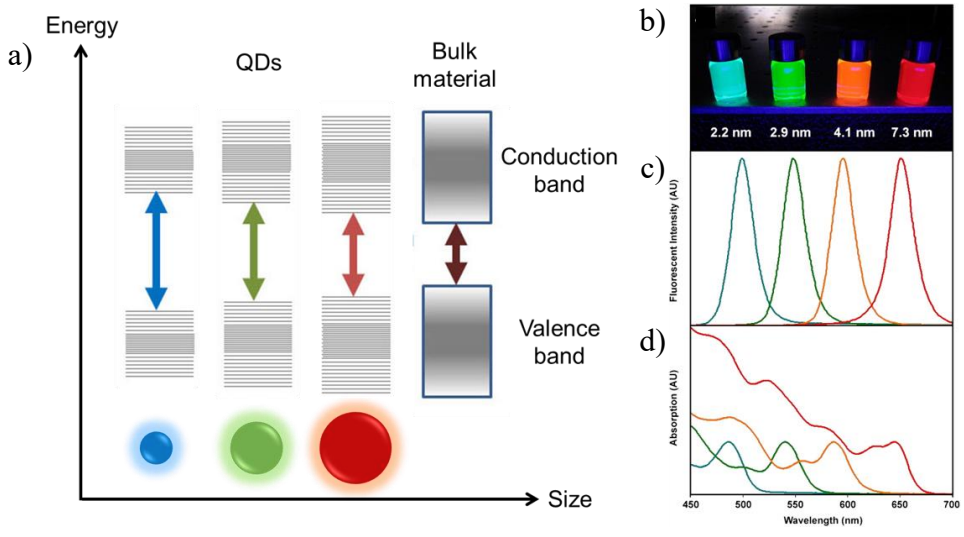

Figure 1 (a) Electronic energy states of QDs and bulk material. (b) Fluorescence images of CdSe QDs with size ranging from 2.2 nm to 7.3 nm, and the corresponding (c) photoluminescence and (d) absorption spectra. (Reprinted from ref [8])

Among these, carbon dots (CDs) are considered as a subset of QDs since their development in the 2000s.[9] However, their synthetic strategies and structural and optical properties are very different from the traditional semiconductor QDs. In terms of materials, the CDs are tiny carbon particles of less than 10 nm in diameter, mainly consisting of sp^2 and sp^3 carbons and small amounts of heteroatoms. Generally, CDs can be classified into three types: amorphous carbon nanodots (CND), crystalline carbon quantum dots (CQD), and graphene quantum dots (GQDs).[10] The GQDs are single or multi-layered crystalline nanoparticles with conjugated π-electron graphene layers that also exhibit quantum confinement (Figure 2a and 2d). The CQDs consisting of multiple layers of graphitic sheets are spherical crystalline nanoparticles that exhibit quantum confinement (Figure 2b and 2e). The CNDs with amorphous structure are thought to be composed of aggregated or cross-linked small molecules or linear polymers (Figure 2c and 2f).[10] Since the CNDs have poor crystallinity, the contribution from the surface states becomes more important. However, some studies have found hexagonal carbon networks in CNDs, which can be interpreted as materials that lies between graphene and fully amorphous structures.[11] Therefore, the emission color of CNDs is mostly determined by surface states rather than quantum confinement effect.

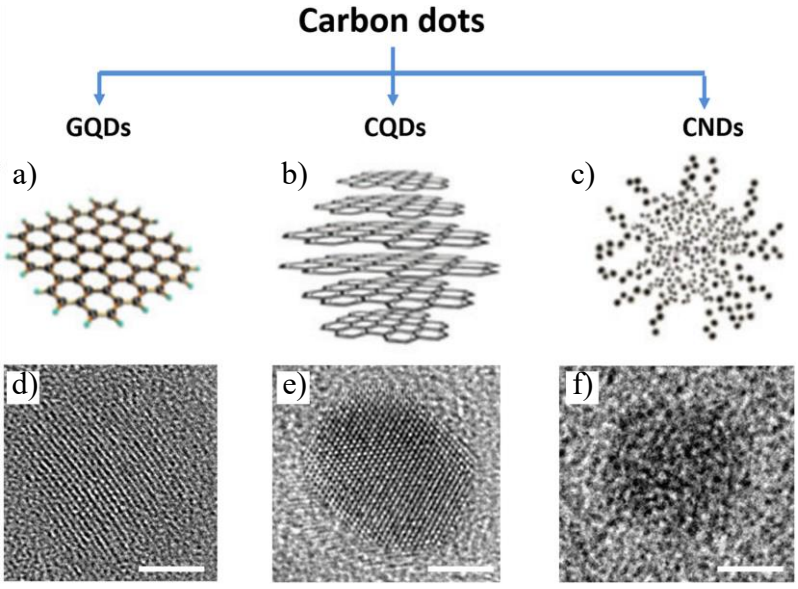

Figure 2 Classification of fluorescent CDs. (a-c) Illustration and (d-f) HRTEM of (a, d) GQDs, (b, e) CQDs and (c, f) CNDs structures. (Reproduced from ref.[12–15])

According to structural and spectroscopic characterizations of CDs, the origin of CDs's photoluminescence (PL) can be explained by two mechanisms: the quantum confinement effect

of sp^2-conjugated carbon core determined by the size of π-conjugated system and the surface state influenced by surface functional groups. Introduction of heteroatoms affects local charge distribution to change electronic energy levels.[10,16,17] By doping heteroatoms, PL and other electro-optical properties of CDs can be tuned; for example, absorption and PL quantum yield (QY) can be enhanced.[18–21] In addition, these heteroatoms provide several functional groups on the surface of CDs that are required for the design of catalysts and chemosensors.

Meanwhile, cadmium-free QDs from ternary groups 11–13–16 QDs, such as silver indium sulfide ($AgInS_2$) and silver gallium sulfide QDs ($AgGaS_2$), have been intensively studied due to their tunable electronic properties and intense luminescence.[22–25] However, the PL of these QDs mainly originated from defect states that locate in the bandgap, not from the transition between conduction and valence bands. These emissions are known as a donor-acceptor pair (DAP) PL, whose mechanism is shown in Figure 3a.[26,27] Therefore, these QDs exhibit a broad PL spectrum due to defects in the crystal and/or on the surface of the QDs, resulting in lack of the monochromaticity that is essential for optoelectronic devices. Several methods have been developed to eliminate the defect levels, including composition tuning and surface passivation with thiol ligands[25] or wide-bandgap inorganic materials (zinc sulfide, ZnS).[22] However, the broadband emission remained unchanged, although the PLQY was significantly increased to 80%. In 2018, Uematsu and Kuwabata et al. successfully generated narrow band emission by coating the surface of $AgInS_2$ QDs with gallium sulfide (GaS_y) shell. This material can effectively remove the defect levels on the $AgInS_2$ cores, and exhibit a narrow-band emission with a PLQY as high as 56%.[28] However, the GaS_y shell was amorphous and easily damaged by hydration, resulting in regeneration of DAP PL. Therefore, surface modification of these core/shell QDs is highly required to improve their PL performance and durability.

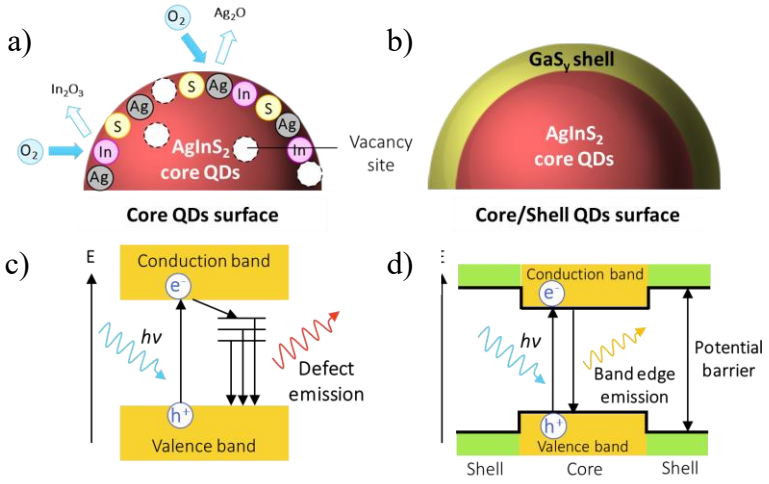

Figure 3 (a, b) Illustrations and (c, d) band alignments of the groups 11–13–16 semiconductor QD (a, c) core and (b, d) that coated by GaS_y shell.

Generally, there are several approaches to enhance the PL properties and stability utilizing surface modification as shown in Figure 4. Figure 4a shows coating the core QDs with another kind of semiconductor materials which possess a band gap sufficient to confine charge carrier. Moreover, stabilizing ligands such as trioctylphosphine (TOP) can be added to improve the PL properties of core/shell QDs as shown in Figure 4b. For example, $AgInS_2/GaS_y$ core/shell QDs possess unsaturated sulfur sites on the surface of QDs. These sites can trap electrons and holes, leading to broadband emission and reduced PLQY. The addition of TOP eliminated these defect sites and improved PLQY by a factor of 2 or more. Furthermore, coating the core/shell QDs by polymer or inorganic materials is also an effective strategy to protect the materials from the environment (Figure 4c). The purpose of this study is to adopt these methods to understand the surface structure of CDs and the groups 11–13–16 semiconductor QDs, and to improve their optical properties.

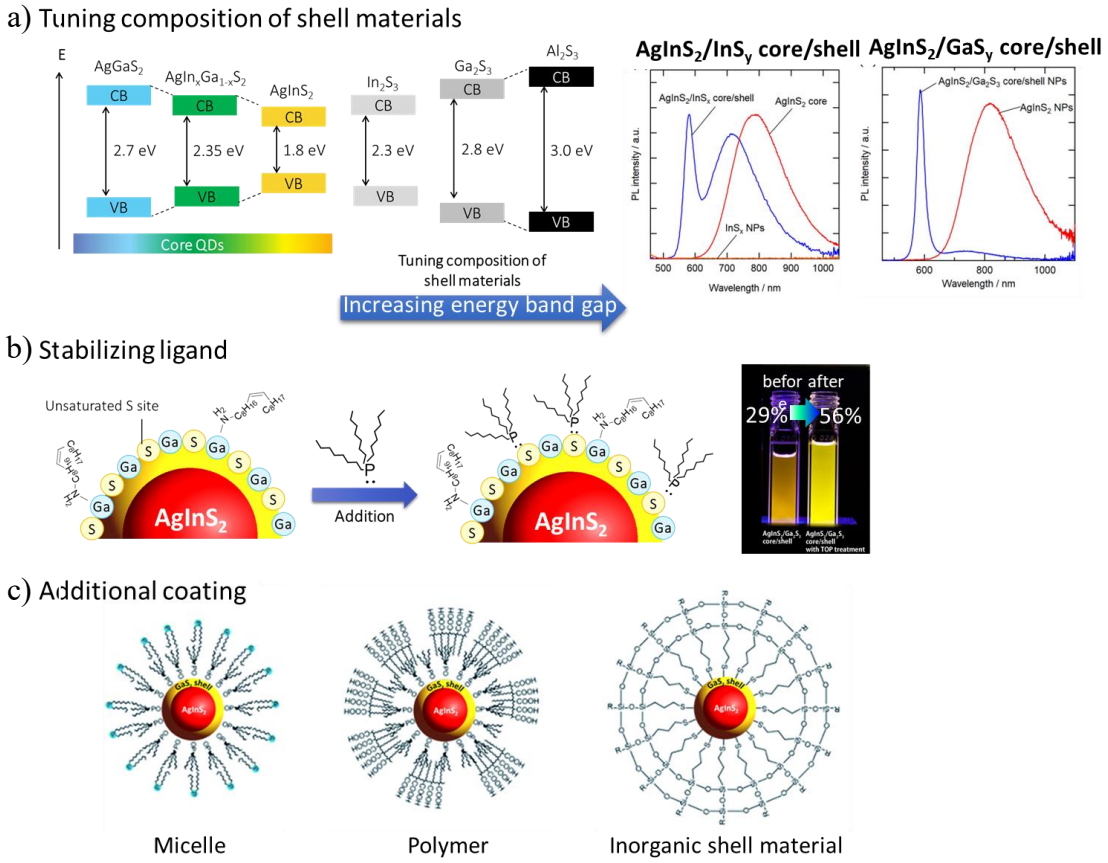

Figure 4 Surface modification methods (a) tuning composition of shell materials,[28] (b) addition of stabilizing ligand,[28] and (c) additional coating on the top of the surface of core/shell QDs.[29–32]

Present works

In my dissertation, I present new surface modification approaches for improving PL properties of CDs and the groups 11–13–16 semiconductor QDs/GaS_y core/shell QDs. The paper consists of three main chapters as follows:

Chapter 1: The photoelectrochemical studies of multicolor-emitting nitrogen–sulfur co-doped CDs are described. The key factor to control their PL properties and sensing behavior toward metal ions is surface functional groups, which can be altered by a heteroatom doping.

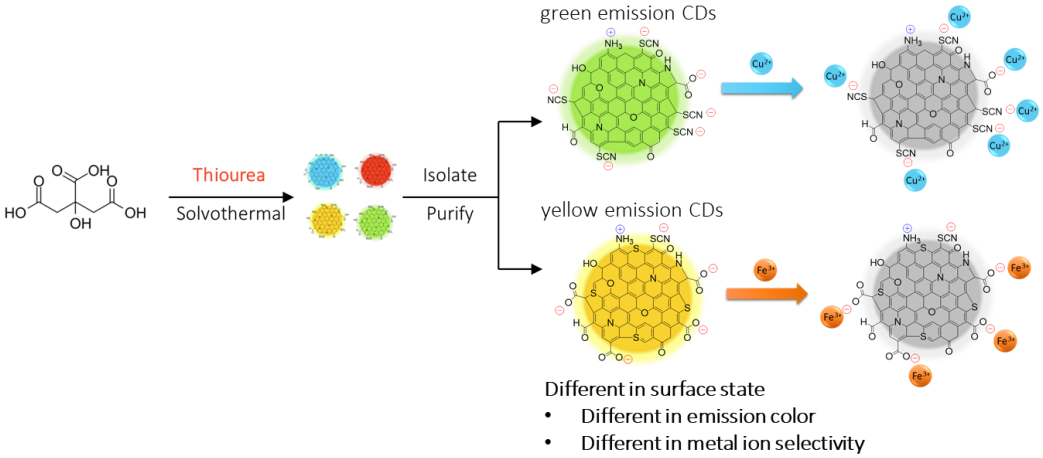

Chapter 2: The PL stability of $AgInS_2/GaS_y$ core/shell QDs, which are susceptible to damage due to amorphous nature of GaS_y shell, is improved by encapsulation of the QDs into a nanostructure of indium-fumarate metal organic frameworks (InMOFs). The damage to the shell during the encapsulation reaction can be avoided by the optimization of the synthesis-solution pH. Thus, encapsulated QDs maintained the original spectral shape, and the PL quantum yield (QY) did not change at all after 7 days at least.

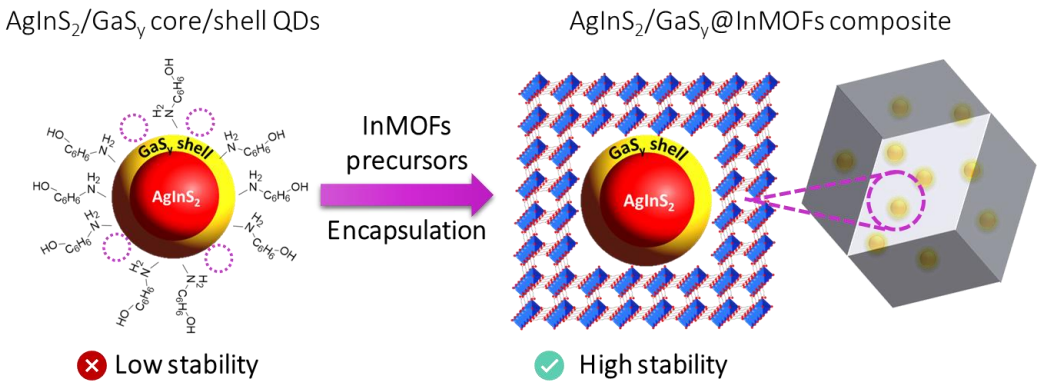

Chapter 3: A new method to synthesize $AgIn_xGa_{1-x}S_2$ (AIGS) quaternary QDs with high product yield has been developed. Narrow-band emission occurred after GaS_y shell coating, and further chloride treatment reduced defect band emission and produced strong PL.

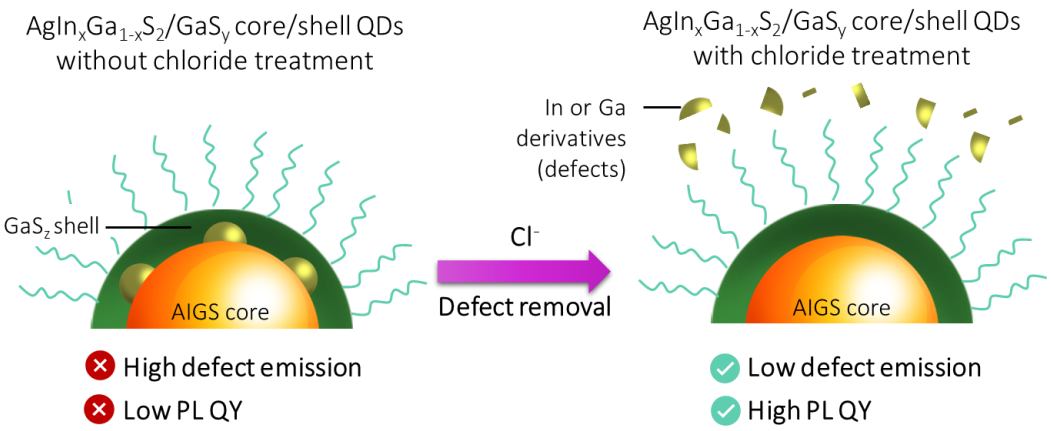

- High defect emission
- Low PL QY

- Low defect emission
- High PL QY

Chapter 1

Synthesis of multicolor-emitting nitrogen–sulfur co-doped carbon dots and their photoelectrochemical studies for sensing applications

1.1 Introduction

Carbon dots (CDs), a new type of fluorescent nanomaterials, have garnered plenty of interest over the last decade because of their distinctive properties such as emission tunability, high fluorescence quantum yield, chemical inertness, and biocompatibility. CDs are characterized as tiny carbon compounds with a size of less than 10 nm that are largely made up of sp^2 and sp^3 carbons with a little quantity of heteroatoms. To alter emission qualities, these heteroatoms provide energy structure modifications.[10,33,34] Although numerous approaches to prepare CDs have been devised, the solvothermal method is considered to be one of the simplest processes. When a combination of carbon sources, including phenylenediamine, citric acid, urea, hydroquinone, ethylenediamine, and even lemon juice, is reacted in common solvents such as ethanol, DMF, acetone, and formamide, CDs with varied emission colors are generated owing to heteroatom variation.[35–37] Basically, photon absorption and emission occur in the sp^2-conjugated sections of the carbon centers, and the photoluminescence (PL) property depends on the size.[16,38,39] Doping heteroatoms change the electron orbitals of both sp^2 moieties and surface functional groups, resulting in changes in the PL characteristics.[16,40,41] For example, researchers observed that doping sulfur atoms together with nitrogen enhances the PL intensity.[19–21] As a result, nitrogen–sulfur co-doped CDs have received extensive research and are used in a variety of applications such as bioimaging,[42–44] lighting,[45,46] drug delivery,[47,48] and chemosensors.[21,49–51] Typically, PL quenching depends on specific chemical features of the CDs, such as surface functional groups and the redox potential of energy levels. Hence, examinations of PL intensity variations due to the addition of various quenchers will offer extensive information about the CDs. Sun et al. created nitrogen–sulfur co-doped CDs from L-cysteine and utilized them to detect Co^{2+}

upon the addition of Co^{2+}, and the complexation between the surface functional groups of the CDs with Co^{2+} occurred and exhibited the quenching of the PL.[52] Also, Sun et al. created nitrogen–sulfur co-doped CDs from heparin sodium and utilized them for sensing Fe^{3+}.[53] The majority of these experiments have been conducted with blue color emission CDs, but only a few reports has been tested with other hues. Because the emission color and surface qualities are so closely coupled, if the sensitivity and selectivity against various chemicals varies depending on the emission color, which would be useful for both understanding CDs and designing better chemosensors, is worth investigation.

The study in this chapter aims to provide one-pot synthesis of the CDs with green and yellow emissions by solvothermal synthesis using citric acid and thiourea in the DMF solution. During the process, the precursors undergo hydrolysis and carbonization to form numerous types of carbon dots, which are isolated using column chromatography. To characterize the CDs, structural and optical approaches are used. In addition, PL properties and sensing mechanism of these CDs were investigated by PL quenching upon the addition of electrochemically active species in various situations.

1.2 Experimental section

1.2.1 Materials

Citric acid was supplied by TCI. Thiourea, dimethylformamide (DMF), 2-amino-3-chloro-1,4-napthoquinone, disodium anthraquinone-1,5-disulfonate, silver nitrate ($AgNO_3$), cadmium nitrate ($Cd[NO_3]_2 \cdot 4H_2O$), cobalt (II) chloride ($CoCl_2 \cdot 6H_2O$), nickel (II) nitrate ($Ni[NO_3]_2 \cdot 6H_2O$), and lead (II) nitrate ($Pb[NO_3]_2$), and zinc nitrate ($Zn[NO_3]_2 \cdot 6H_2O$) were purchased from Fujifilm Wako Chemicals. Copper (II) perchlorate ($Cu[ClO_4]_2 \cdot 6H_2O$), iron (III) chloride ($FeCl_3 \cdot 6H_2O$), and manganese (II) chloride ($MnCl_2 \cdot 4H_2O$) were purchased from Kishida chemicals. Next, iron (II) chloride ($FeCl_2 \cdot 4H_2O$) was supplied by Kanto chemicals. Dichloromethane (CH_2Cl_2), Methanol (MeOH), Ethyl acetate (EtOAc), and diethyl ether (Et_2O) were purchased from Fujifilm

Wako Chemicals. Water used in the present study was purified by a Milli-Q Integral 3 (Merck) with a resistivity of greater than 18.2 MΩ·cm.

1.2.2 Instrument

The morphologies of the prepared CDs were studied by a Hitachi H-7650 transmission electron microscope (TEM). The average particle size was determined by measuring at least 200 particles in TEM images. The KBr pellet technique was used to record Fourier transform infrared (FT-IR) spectra on a Perkin Elmer Spectrum 100 FT-IR Spectrometer. X-ray diffraction (XRD) patterns were captured using a powder X-ray analysis system (Rigaku, SmartLab) equipped with a parallel-beam/parallel-slit analyzer. X-ray photoelectron spectra (XPS) were collected with an X-ray photoelectron spectrometer (Shimadzu, KRATOS AXIS-165x) fitted with an aluminum target. A Jasco FP-8600 spectrofluorometer was used to capture the PL spectra. A Jasco V-670 spectrophotometer was used to record the ultraviolet-visible (UV–vis) absorption spectra. The PL lifetimes were calculated from time-resolved spectra obtained using a Hanamatsu Quantaurus-Tau C11367-22. The absolute PL quantum yield (QY) was evaluated using a PMA-12 (Hamamatsu) equipped with an integrating sphere.

1.2.3 Synthesis of CDs

The CDs were synthesized by mixing 4.2 g (0.02 mol) of citric acid and 7.6 g (0.10 mol) of thiourea with 100 mL of DMF. Before transferring the mixed solution to a Teflon-lined autoclave, it was agitated for 15 minutes. After heating the solution at 160°C for 24 h, it was allowed to cool to an ambient temperature. A 0.45 μm Polytetrafluoroethylene syringe filter was used to filter out large particles from the crude solution. Following that, a 1:5 Et_2O: EtOAc mixture was added in excess to precipitate big particles, which were removed by centrifugation. The supernatant was collected and purified using column chromatography with gradient elution method using CH_2Cl_2 and MeOH. Next, the CDs were separated into four portions that revealed four various colors

of blue, green, yellow, and orange, which were labelled as b-CDs, g-CDs, y-CDs, and o-CDs, before being distributed in the water.

1.2.4 PL quenching by quinone derivatives

Aqueous solutions of the g-CDs and y-CDs were separately prepared at the concentration of 0.4 mg/mL. 2-amino-3-chloro-1,4-napthoquinone and disodium anthraquinone-1,5-disulfonate were separately dissolved in water at the concentration of 1.25 mM, which was the stock solutions of the quenchers. Next, PL spectra of the CDs were determined in the absence and presence of the quenchers.

1.2.5 Metal selectivity tests

The 0.1 M aqueous solutions of $AgNO_3$, $Cd(NO_3)_2$, $CoCl_2$, $Cu(ClO_4)_2$, $FeCl_3$, $FeCl_2$, $MnCl_2$, $Ni(NO_3)_2$, $Pb(NO_3)_2$, and $Zn(NO_3)_2$ were prepared separately as stock solutions. These metal-ion solutions were mixed with the solutions of the CDs (0.4 mg/mL) with the concentration of up to 5 mM, and the PL intensities were measured using the spectrofluorometer. For specific combinations, PL decay curves were measured and the variations in lifetimes and PL intensity were compared. The PL quenching tests were also performed in different temperatures to investigate the interaction between the CDs and quenchers.

1.3 Result and discussion

1.3.1 Characterization of CDs

Citric acid and thiourea, which are precursors for the solvothermal synthesis of the CDs, undergo dehydration and carbonization at higher temperatures (>160°C) to form photoluminescent CDs consisting of multiple aromatic rings. The as-prepared solution revealed white PL under UV irradiation, and its PL peak wavelength varies depending on the excitation wavelength (Figure 1-1a). These results showed that numerous different types of CDs were produced during heating (Figure 1-1b) and column chromatography was conducted to separate the crude product into four sections

exhibiting blue, green, yellow, and orange color emissions (Figure 1-1c). Because the quantities of b-CDs and o-CDs were low, a quantifiable amount could not be obtained after an extra purifying step. Therefore, the g-CDs that exhibited the highest PLQY (Table 1-1, in acetonitrile), and the y-CDs that were the major product under the present synthetic conditions, were chosen for further analysis.

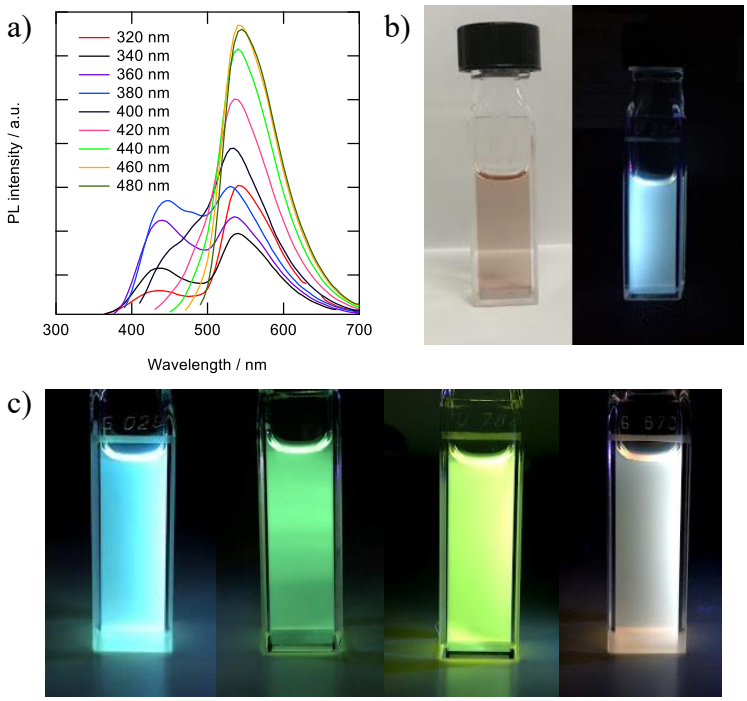

Figure 1-1 (a) Photoluminescence spectra of as-prepared CDs measured in aqueous solution at different excitation wavelengths (pH 7.0) and (b) CD solution as prepared in the presence of ambient light and 365 nm UV light. (c) The solutions of the b-CDs, g-CDs, y-CDs, and o-CDs after purification process under 365 nm UV irradiation.

Table 1-1 Optical properties of g-CDs and y-CDs.

CDs	**λ_{ex} (nm)**	**λ_{em} (nm)**	**PLQY (%)**			
			CH_2Cl2	CH_3CN	MeOH	H_2O
g-CDs	420	540	3	58	36	17
y-CDs	450	565	6	20	15	5

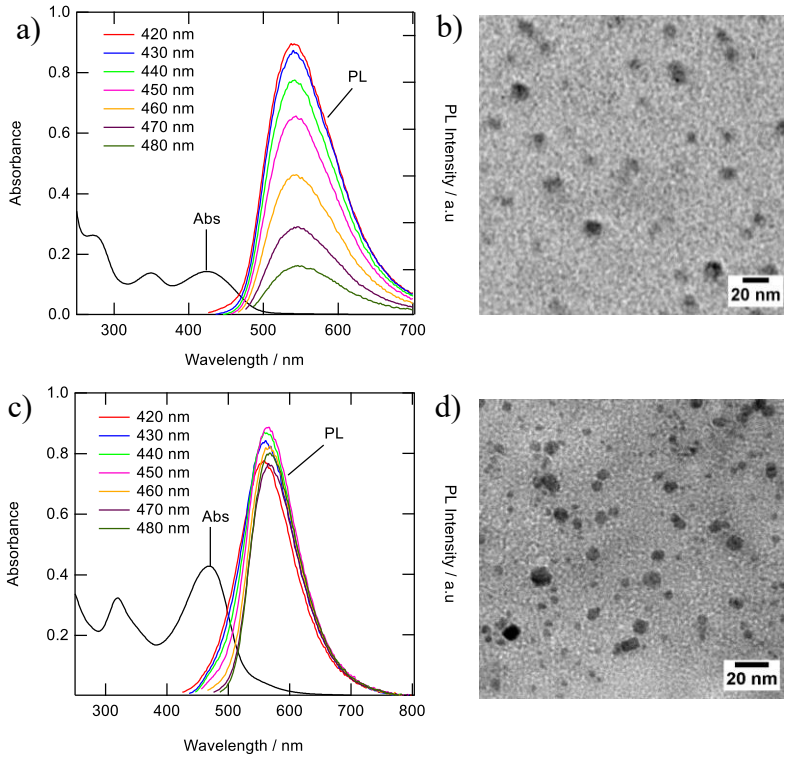

Figure 1-2 (a, c) UV–vis and PL spectra, and (b, d) TEM images of the g-CDs (a, b) and y-CDs (c, d). The PL spectra were recorded as a function of different excitation wavelengths in aqueous solution (pH 7.0).

The UV–vis absorption spectra of the g-CDs and y-CDs reveal distinct absorption profiles (Figure 1-2a and 1-2c). The absorption bands corresponding to the π–π* transition of the graphitic sp^2 carbon and the n–π* transition of the conjugated C=O appeared in the UV region. Furthermore, typical absorption bands centered at 425 nm and 470 nm for the g- and y-CDs were observed. These bands could be attributed to the n–π* transition of the conjugated C=N and C=S bonds, which is usually present in the nitrogen–sulfur co-doped CDs prepared by a solvothermal process using citric acid and thiourea.[20,54,55] Hence, CDs are thought to have several emission states in a single particle, resulting in the excitation wavelength dependency of the emission spectra illustrated in Figure 1-3a and 1-3b. When the excitation wavelength is tuned to UV, the chromophore with C=O bonds is stimulated, producing blue color emission (400–450 nm).[116,17,38–41] Conversely, when the same CDs were stimulated around the significant absorption peaks locating in the visible region (400–460 nm for the g-CDs and 430–490

nm for y-CDs), green (540 nm) and yellow (567 nm) emissions were generated, respectively. Positions of these PL peaks were independent on the stimulation wavelength (Figure 1-2a and 1-2c), and the shapes of PL excitation spectra of each sample (Figure 1-3c and 1-3d) were comparable to the absorption spectra in the wavelength region longer than 300 nm (Figure 1-2). These findings revealed that the CDs' electronic levels had degraded to some extent. However, they were different from semiconductor quantum dots, which had a band structure and a distinct quantum size effect, which is obvious from the similarity in the particle diameters between the g-CDs (8.3 nm) and y-CDs (7.0 nm) (Figure 1-2c and 1-2d).

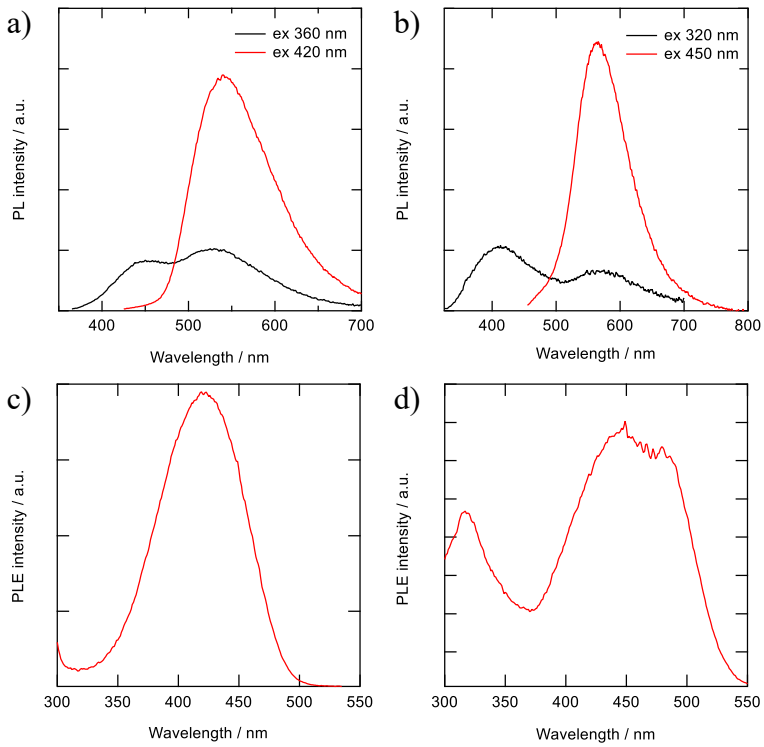

Figure 1-3 PL spectra of the (a) g-CDs and (b) y-CDs were recorded with varied excitation wavelengths in an aqueous solution (pH 7.0). PL excitation spectra of the (c) g-CDs and (d) y-CDs were recorded at PL peak wavelengths in an aqueous solution (pH 7.0, 420 nm for g-CDs and 450 nm for y-CDs).

The FT-IR and XPS spectra are shown in Figure 1-4 and 1-5, respectively. The FT-IR spectra showed that both types of CDs have several kinds of hydrophilic moieties, such as N–H (approximately 3500 cm^{-1}), O–H (3194 cm^{-1}), COOH (1712 cm^{-1}), and CONR (1670 cm^{-1}) resulting in good dispersity in aqueous media (Figure 1-4).

Meanwhile, the stretching vibration of –SCN (2070 cm^{-1}), C=C (1575 cm^{-1}), and C=N (1403 cm^{-1}) groups were observed, confirming the presence of polyaromatic structure formed during the reaction process. A comparison of the two spectra reveals two crucial facts. First, the y-CD's O–H stretching vibration band, which occurred about 3200 cm^{-1}, was wider than that of the g-CDs, indicating the presence of multiple kinds of hydroxyl groups on the surface of the y-CDs due to a higher degree of oxidation.[16] Secondly, the relative intensity of –SCN moiety of the y-CDs was significantly weaker than that for the g-CDs, showing that these groups in the y-CDs were transformed into sulfone or thiophene.

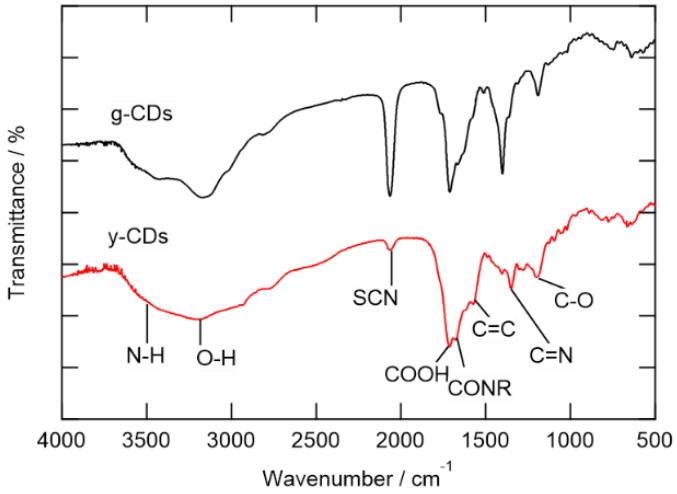

Figure 1-4 FT-IR spectra of the g-CDs and y-CDs.

The presence of nitrogen and sulfur was verified by XPS analysis for both the g- and y-CDs. The spectra of the C1s region could be deconvoluted into three peaks, which were assigned to C–C or C=C (284.4 eV), C–O or C–N or C-S (286.0 eV), and C=O (288.1 eV) groups (Figure 4). The spectra in the N1 s region exhibited two peaks, located at 399.4 and 401.4 eV, and were assigned to pyrrolic N or N–H and graphitic N, respectively. The g-CDs revealed a single kind of sulfur (S 2p), yielding two peaks (168.1 and 169.3 eV) that are assigned to S 2p 3/2 and 2p 1/2 of –C–SO_x–C– sulfone bridges.[20,54–56] The spectrum for the y-CDs exhibited small peaks at lower energy levels (164.3 eV, which could be assigned to thiophene, consistent with the FT-IR data. As a result, the sulfur content of the y-CDs was greater (4.83%) than that of the g-CDs

(3.66%), as indicated in Table 1-2. As previously reported, these findings suggested that sulfur plays an important role in defining PL characteristics.[19–21]

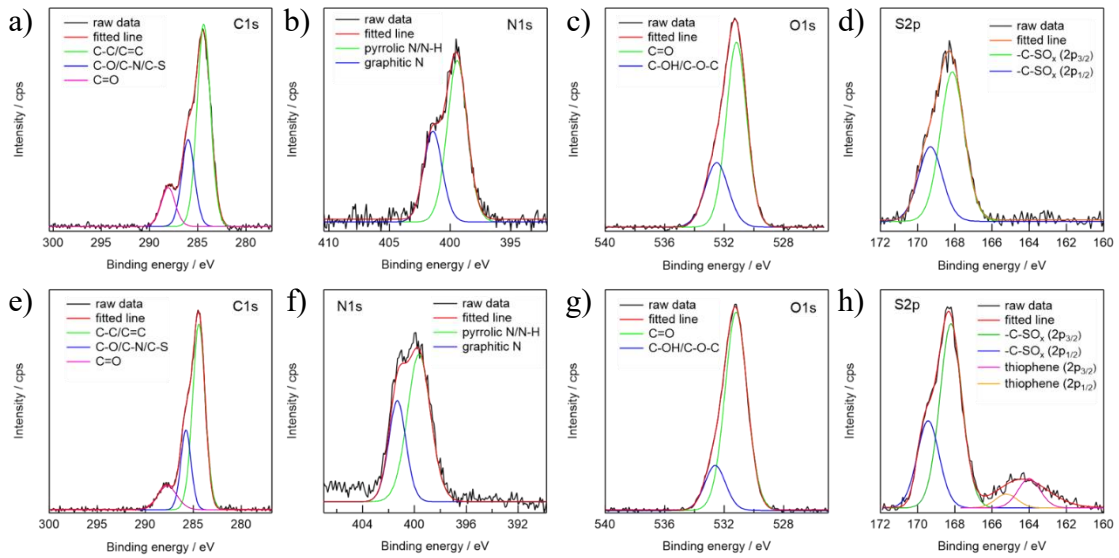

Figure 1-5 XPS spectra of the g-CDs and y-CDs for (a, e) C 1s, (b, f) N 1s, (c, g) O 1s, and (d, h) S 2p regions.

Table 1-2 Chemical composition determined by XPS

Atomic concentration (%)	C	N	O	S
g-CDs	55.16	10.93	30.26	3.66
y-CDs	55.83	9.86	29.49	4.83

1.3.2 PL quenching mechanism

One of the possible applications of CDs is a chemosensor, particularly for detecting metal ions that take the merit of a variety of surface functional groups on the CDs. While certain CDs have excellent selectivity against metal ions, the mechanism of PL intensity variations has not been well examined. Typically, PL quenching of CDs by electrochemically active substances can be either dynamic or static. The former (dynamic quenching) is an electron or energy transfer process that occurs when a photoexcited CD collides with a ground state quencher, and the amplitude of the quenching is determined by the interaction of the CDs and the quenchers.[57,58] In the latter case (static quenching), the quenchers are attached to the ground state CDs, which

generate non-luminescent complexes. The static process exhibits a higher magnitude of the quenching (higher sensitivity against the quencher) because of the absence of the slow diffusion process. In this case, the magnitude of the quenching is typically determined by the potential gap of the corresponding orbitals (in case of electron transfer) or spectral overlap (in case of Förster energy transfer) of donors and acceptors. For understanding the phenomenon, the correlation between the PL intensity variations and the concentration of the quencher, which is known as the Stern–Volmer-type plot, is frequently used.

$$\frac{I_0}{I} = 1 + K_S[Q]$$

where I_0 and I are the PL intensities in the absence and presence of quencher, respectively. K_S is the quenching constant and $[Q]$ is the concentration of the quencher, which is an analyte in the chemosensing. In the beginning, I examined the effect of electrostatic interactions between the CDs and analytes. Ionic quinone derivatives were utilized to analyze the electrostatic effects and identify the ionic charge of the CDs to avoid the complexation of the analytes with a specific functional group of the CDs. Figure 1-6 reveals the PL intensity variations of the CDs (the g- and y-CDs) in the presence of quinone derivatives. The quenching coefficients (K_S) for cationic 2-amino-3-chloro-1,4-naphthoquinone were as high as $5.04\times10^3\ M^{-1}$ and $5.22\times10^3\ M^{-1}$ for the g-CDs and y-CDs, respectively. When anionic anthraquinone-1,5-disulfonate was combined with the g-CDs and y-CDs, no noticeable PL quenching was seen. Because the spectrum overlaps between the quencher's optical absorption and the PL of the CDs are low, the fluorescence resonance energy transfer cannot be occurred in these cases.[45] Therefore, the photoinduced electron transfer from the CDs to the quenchers as a quenching process seems possible. Furthermore, the cationic and anionic quenchers possess very similar reduction potentials to one another, i.e., −0.170 V for anthraquinone-1,5-disulfonate[59] and −0.177 V for 2-amino-3-chloro-1,4-naphthoquinone as a function of the standard hydrogen electrode at pH = 7.[60] These findings pointed to the anionic environment of CDs derived from carboxylate and thiocyanate groups. The magnitudes of quenching by the cationic quencher were

between the dynamic (~10^2 M^{-1}) and static (~10^5 M^{-1}) processes, showing substantially strong interaction with the cationic quenchers. As a result, the repulsive force created by the overlap of electric double layers becomes greater than that of tiny molecules, resulting in the PL's intactness in the presence of anionic quenchers.

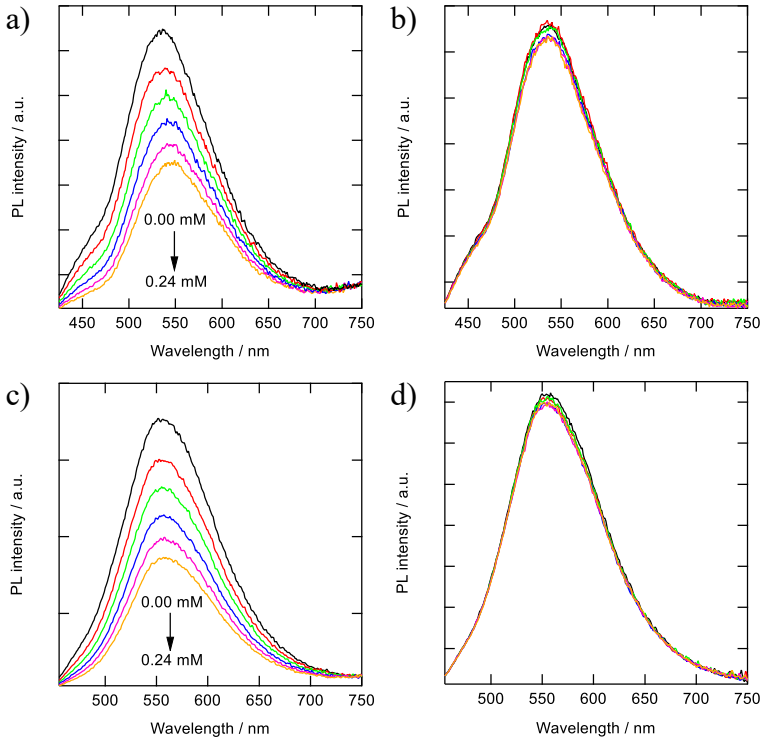

Figure 1-6 PL intensity variations of the (a, b) g-CDs and (c, d) y-CDs in the presence of (a, c) 2-amino-3-chloro-1,4-naphthoquinone and (b, d) anthraquinone-1,5-disulfonate in aqueous solution (pH 7.0).

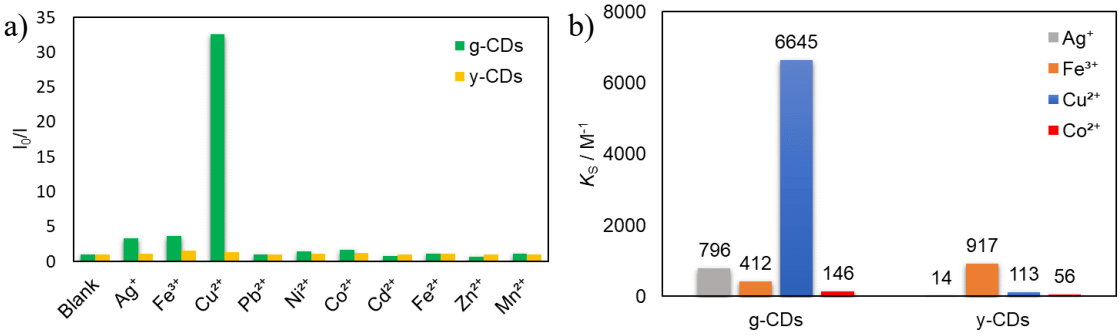

Figure 1-7 (a) Quenching efficiency of the g-CDs (green bars) and y-CDs (yellow bars) upon the addition of 5 mM various metal ions. (b) K_S values recoded for the g-CDs and y-CDs by the addition of the selected metal ions.

The selectivity of the CDs for metal detection was examined by adding various metal ions in 5 mM (Figure 1-7a). The magnitudes of quenching significantly varied by metal ions, which were evaluated as a function of I_0/I. Basically, attractive force is expected between anionic CDs and metal cations. However, several metal ion species (Ag^+, Co^{2+}, Cu^{2+}, and Fe^{3+}) exhibited high to moderate quenching magnitudes. Among these, the PL intensity variations of the g-CDs and y-CDs by the addition of the selected four metal ion species were shown in Figure 1-8 and Figure 1-9, respectively. The values for K_S (the slopes of the Stern–Volmer-type plots) were summarized in Figure 1-7b. Notably, the g-CDs exhibited the highest K_S (6.645 M^{-1}) for Cu^{2+}, which was moCre than 10 times higher than that observed for Co^{2+} (146 M^{-1}). In contrast, the y-CDs recorded the highest K_S by Fe^{3+} (917 M^{-1}), and that by Cu^{2+} was very low (113 M^{-1}) indicated irregular variations in the magnitude of PL quenching, i.e., the highest K_S (6645 M^{-1}) was obtained by Cu^{2+} (0.34 V vs. SHE), whereas that by Ag^+ (0.80 V) and Fe^{3+} (0.77 V) were 10 times lower (796 M^{-1} and 412 M^{-1}, respectively). Even when the intensity of the electrostatic interactions is considered, i.e., Fe^{3+} ions should have the highest attractive force with negatively charged g-CDs of the three. These results indicated that the high selectivity of the g-CDs toward the detection of Cu^{2+} is due to the unique structure of the g-CDs, which is the presence of thiocyanates groups on their surface, which is known to improve the adsorption of specific metal cations like Cu^{2+}.[54,61] These arguments favored the development of non-luminescent complexes as the mechanism of quenching rather than electron transfer. The limit of detection was calculated based on the standard deviation of the blank samples and the slope of calibration curve,[62] and it was found to be 10 μM, which is higher than those given in other reports. However, g-CDs can still be used as sensor to determine excess Cu^{2+} content in drinking water based on world health organization standard.[63]

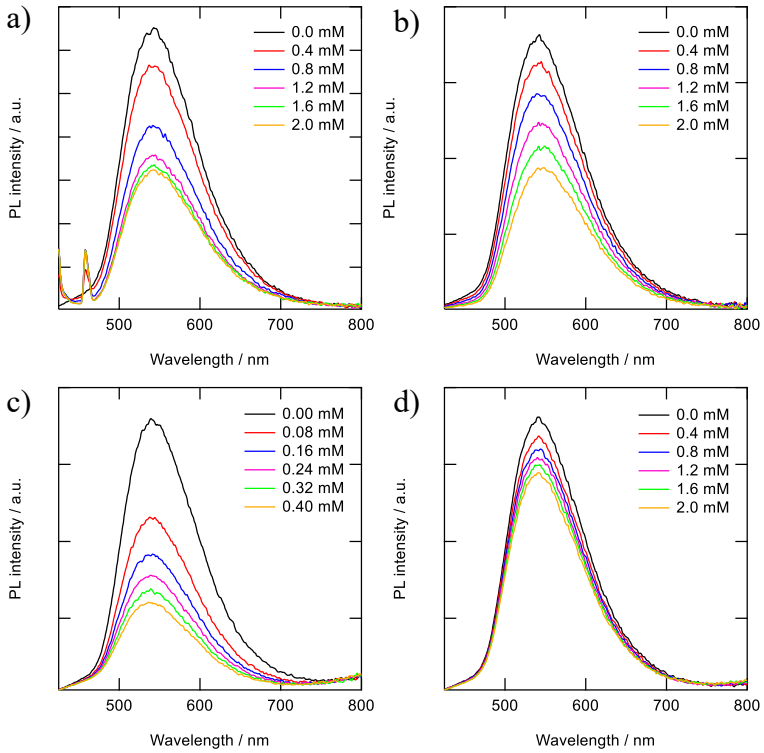

Figure 1-8 Variations in photoluminescence spectra for the g-CDs by the addition of (a) Ag^{+}, (b) Fe^{3+}, (c) Cu^{2+}, and (d) Co^{2+} in aqueous solution (pH 7.0).

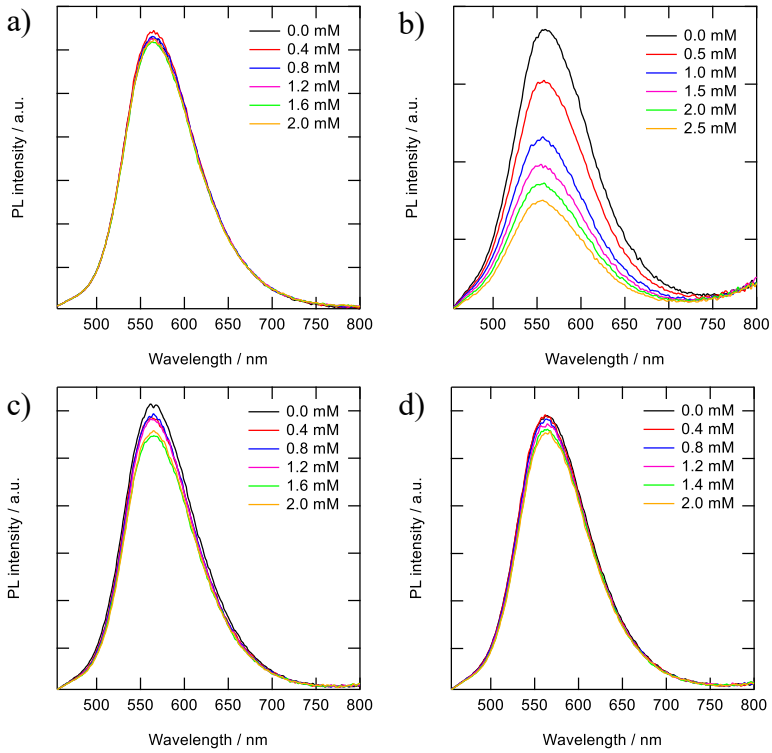

Figure 1-9 Variations in photoluminescence spectra for the y-CDs by the addition of (a) Ag^{+}, (b) Fe^{3+}, (c) Cu^{2+}, and (d) Co^{2+} in aqueous solution (pH 7.0).

In the case of the y-CDs, the highest K_S was recorded by Fe^{3+} (0.77 V), and it decreased by Cu^{2+} (0.34 V) and Co^{2+} (−0.277 V) in this order. However, among these metal ions, Ag^{+}, which has the highest reduction potential (0.80 V), did not exhibit PL quenching. These findings suggested that the magnitudes of quenching had no bearing on the reduction potentials. The limit of detection was found to be 0.11 mM, which is much higher than in other reports. This result indicates that the metal resistance of y-CDs due to the lack of specific surface functional groups. Therefore, by further modification, y-CDs can be used as fluorescence dye for bioimaging.

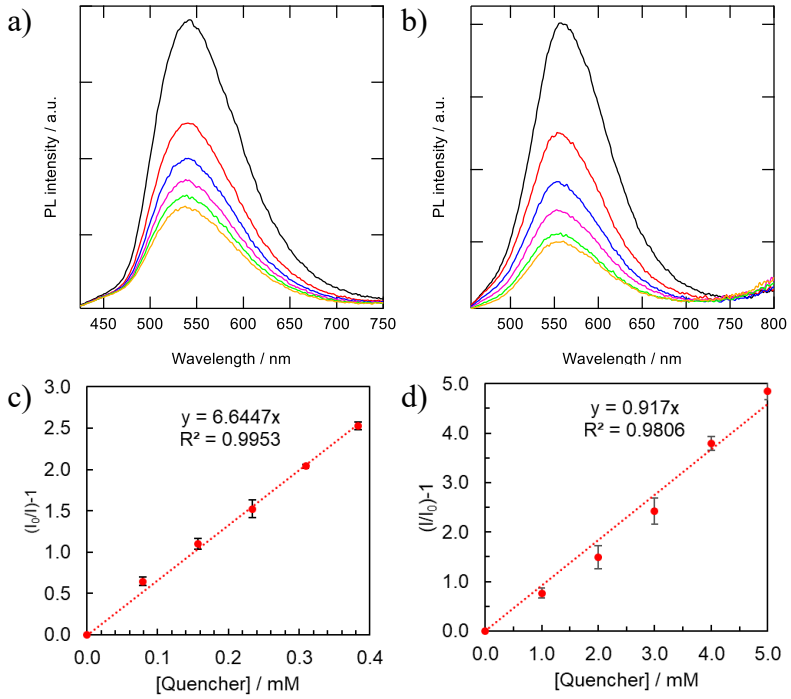

Figure 1-10 Variations in PL spectra (a, b) and the corresponding Stern–Volmer-type plots of the quenching (c, d) for the combinations of the g-CDs with Cu^{2+} (a, c) and the y-CDs with Fe^{3+} (c, d).

Figure 1-10 and 1-11 showed the PL spectra and the decay curves for the g-CDs and y-CDs in the presence of Cu^{2+} and Fe^{3+}, respectively. As previously stated, the PL intensities of the CDs declined as metal concentration increased, resulting in the straight line in the Stern–Volmer-type graphs (Figure 1-10c and 1-10d). Conversely, the PL decay curves maintained unchanged (Figure 1-11a and 1-11b), supporting the formation of non-luminescent complexes rather than electron transfer as expected from the lack of relevance to the reduction potential of the quenchers. The quenching of the g-CDs was

discovered to have an evident contribution from static quenching due to the drop in K_S values with increasing temperature (Figure 1-11c). Conversely, the small increase of the K_S value, which was discovered for the quenching of the y-CDs at a higher temperature, indicated the presence of the dynamic quenching (Figure 1-11d). In any event, the quenching of CDs by metal ions was regulated by metal ion binding and the creation of non-luminescent complexes.

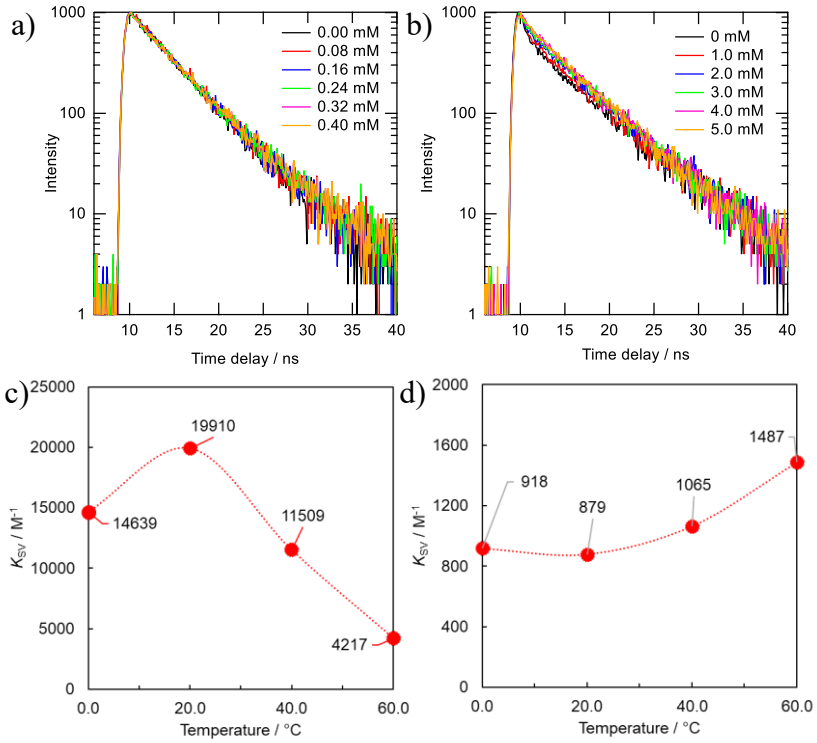

Figure 1-11 (a, b) PL decay curves and (c, d) variations in K_S values under different temperatures for the combinations of (a, c) the g-CDs with Cu^{2+} and (c, d) the y-CDs with Fe^{3+}.

1.4 Conclusion

A solvothermal technique utilizing citric acid and thiourea dissolved in DMF was used to effectively produce nitrogen–sulfur co-doped CDs. By using column chromatography via a gradient elution approach, crude compounds were purified and separated, and CDs with green and yellow emissions were obtained and studied. TEM observation showed that the two types of CDs were similar in size: 8.3±1 nm and 7.1±2 nm for the g-CDs and y-CDs, respectively. These findings suggested that changes in emission color were not caused by the quantum confinement effect. The XRD, IR, and

XPS spectra indicated that the CDs exhibited comparable functional groups, such as carboxylic, amino, thiocyanate, and polyaromatic carbons, but the ratios of these moieties varied depending on the emission colors. The PL quenching tests performed by the addition of ionic electron acceptors (quinone derivatives) demonstrated that the two types of carbon dots possessed anionic functional groups on their surface. They were susceptible to metal ions in different ways because of the differences in surface functional groups. Cu^{2+} considerably quenched the g-CDs, while Fe^{3+} was the most effective in quenching the y-CDs. A detailed analysis of the quenching by metal ions showed that it was caused by the formation of non-luminescent complexes rather than by the electron transfer between the CDs and metal ions.

Chapter 2

Encapsulation of $AgInS_2/GaS_y$ quantum dots in In–fumarate metal organic frameworks for stability

2.1 Introduction

Over the past decades, ternary groups 11–13–16 QDs have received attention owing to the moderately high PL quantum efficiency of the QD cores (>50%) and the advantage of cadmium-free materials that render them environmentally friendly alternatives for cadmium-based counterparts. Therefore, a variety of potential applications have been proposed, i.e., lighting, display, and bioimaging technologies.[64–70] Among theses QDs, $AgInS_2$ QDs have been considered as the most promising materials owing to their adjustable electronic properties and intense luminescence.[22–25] However, $AgInS_2$ QDs exhibit a broad PL spectrum because of the presence of defects in the crystal and/or on the surface of QDs, resulting in deficiency in monochromaticity, which is significantly important for optical devices.[71] Considerable efforts have been devoted to eliminate these defect levels, which include compositional tuning to remove the point defects in the crystals and surface passivation using thiol ligands[25] or wide-bandgap inorganic materials [zinc sulfide (ZnS)][22] to remove the surface defects. Whereas these attempts have increased the PLQY to the level of 80%, the broadband PL spectra remain unchanged. In this context, the research group to which I belong has found that the GaS_y shell effectively removes the defect levels on the $AgInS_2$ cores, and the core/shell QDs exhibit a narrowband emission with a PLQY of as high as 56%.[28] The spectral width of the $AgInS_2/GaS_y$ core/shell QDs are almost comparable or still narrower than other types of cadmium-free QDs, such as indium phosphide[72,73] and silver sulfide[74,75] QDs. Such narrowband emission can be demonstrated in the visible spectral range by compositional tuning.[76,77] According to the high-resolution transmission electron microscopy (HRTEM) and scanning TEM observations, GaS_y shell is found to be amorphous. Because the choice of a highly crystalline material is

generally a fundamental design concept for making good-quality QDs, GaS_y exhibits a very unusual nature as a shell material, which enables passivation of $AgInS_2$ QDs. Amorphous materials typically exist at a higher energy state than crystalline materials. Therefore, core/shell QDs with amorphous shells are expected to be less stable than those protected by crystalline shells. In fact, the $AgInS_2/GaS_y$ core/shell QDs are easily damaged by exposure to light, moisture, and oxygen, resulting in the decrease in the PL properties. Therefore, the formation of an independent protection layer at the top of the GaS_y shells is still required when QDs are used in severe conditions. In this sense, mechanical protection using solid materials as substitute for the easily detachable organic ligands is promising. Among these materials, solids with an intrinsic coordinating nature are preferable. Metal–organic frameworks (MOFs) are a novel class of materials consisting of metal ions or clusters coordinated to polytopic organic linkers that exhibit specific features in numerous applications, including catalysis,[78] gas storage,[79] sensing,[80] and molecular separation.[81] In addition, MOFs have been reported to be potentially useful as a host material for fluorescence dye,[82] carbon dots,[83] and cadmium-containing QDs.[84]

To prevent possible alloying of GaS_y and the resulting deterioration of the band-edge PL, I considered the type of metal constituent of MOFs, and, in particular, focused on the MOFs that consisted of fumarate and oxide clusters of the group 13 metals (Al, Ga, and In). A well-known Al-fumarate MOF [Matériaux de l'Institut Lavoisier-53 MOFs (MIL-53)] was first investigated for gas storage (CO_2, CH_4, and H_2) and gas-separation purposes.[85–88] Subsequently, its analogs, which consisted of oxide clusters of In and Ga, were synthesized using the solvothermal method.[89] These MOFs consists of a group 13 metal center that contained six octahedrally coordinating oxygen atoms. Four of these atoms were components of the fumarate linkers, and the remaining two were derived from hydroxyl groups. These hydroxyl groups bridged the neighboring metal centers to form a one-dimensional chain of M–O–M. The fumarate linkers represented the cross linking between the one-dimensional M–O–M chain, resulting in the formation of rhombic channels alongside the chain. In that report, In- and Ga-fumarate MOFs and

their variants were synthesized by a solvothermal approach using DMF, ethanol, and methanol as solvents. Among these MOFs, the Ga-fumarate MOFs were synthesized under severer conditions (60 °C–180 °C; typically, 80 °C in an autoclave) using DMF as a solvent, whereas the In-fumarate MOFs (InMOFs) were synthesized under relatively mild conditions (typically 20 °C or 40 °C) using ethanol or methanol. Because of the mildness of the synthetic conditions, which was advantageous for preserving PL of the preformed $AgInS_2/GaS_y$ core/shell QDs, I selected the InMOFs as the first candidate for the matrix to encapsulate the band-edge emitting $AgInS_2/GaS_y$ core/shell QDs. InMOFs have been reported to exhibit high thermal stability and moisture resistance. Therefore, the encapsulation of $AgInS_2/GaS_y$ QDs in the matrix of InMOFs was expected to improve the stability of $AgInS_2/GaS_y$ QDs if the band-edge emission was maintained during the incorporation reaction.

In this chapter, I described my attempt to encapsulate $AgInS_2/GaS_y$ core/shell QDs into the nanostructures of InMOFs by growing the MOFs on the core/shell QDs. Prior to the encapsulation reaction, the capping ligand of the QDs were changed from the original oleylamine (OLA) to an amino alcohol, which is one of the solvents available for synthesizing InMOFs. The growth conditions of the InMOFs were engineered so that the spectrally narrow band-edge emission of the $AgInS_2/GaS_y$ core/shell QDs could be maintained during the encapsulation reaction. The resulting composites were characterized using TEM, XRD, and a set of optical measurements.

2.2 Experimental section

2.2.1 Materials

Ag(OAc) (Mitsuwa Chemicals Co., Ltd.), $In(OAc)_3$ (Sigma–Aldrich), $Ga(acac)_3$ (Aldrich), $In(NO_3)_3{\cdot}3H_2O$ (Mitsuwa Chemicals Co., Ltd.), 1-dodecanethiol (DDT, Wako), 1,3-dimethylthiourea (DMTU, TCI), hydrochloric acid (37%, Kishida Chemical Co., Ltd.), 6-amino-1-hexanol (6AH, Sigma–Aldrich), fumaric acid (TCI), tetramethylammonium hydroxide (TMAH, 10% in methanol; TCI), and dehydrated

methanol (Wako) were used without further purification. OLA (Aldrich) was used after vacuum distillation in the presence of calcium hydride.

2.2.2 Instruments

The reaction-mixture temperature was directly measured using a thermocouple and was controlled by a heating mantle equipped with a proportional–integral–derivative controller. The UV–vis absorption and PL spectra of the samples were recorded using a double-beam UV–vis spectrophotometer (JASCO, Japan, V-670) and a fluorescence spectrometer (JASCO, Japan, FP-8600), respectively. The PLQYs were measured using a diode-array spectrometer equipped with an integrating sphere (Hamamatsu, Japan, PMA12). The fluorescence-decay processes were recorded using a time-correlated single-photon counting setup (Hamamatsu, Japan, Quantaurus-Tau). The size and morphology of the QDs were observed using a TEM instrument (Hitachi, Japan, H-7650) at an acceleration voltage of 100 kV. HRTEM images were taken by JEM-ARM-200F (JEOL, Japan) at an acceleration voltage of 200 kV. Carbon-coated copper TEM grids (Oken-shoji, Japan, HRC-C10) were used to prepare the TEM samples. XRD patterns were obtained using a powder X-ray diffractometer (Rigaku, Japan, SmartLab) equipped with a parallel-beam/parallel-slit analyzer. The composition of the composites was analyzed using an inductively coupled plasma atomic emission spectroscopy (ICP-AES) instrument (Shimadzu, Japan, ICPS-7510).

2.2.3 Synthesis of OLA–capped $AgInS_2$ core QDs

OLA–capped $AgInS_2$ (OLA–$AgInS_2$) QDs were synthesized according the literature with a slight modification.[76] Typically, Ag(OAc) (0.8 mmol), $In(OAc)_3$ (0.8 mmol), and DDT (2.4 mmol) were mixed with OLA (16 mL) in a two-necked round-bottom flask. The mixture was degassed under vacuum at 120 °C for 5 min. The solution was rapidly heated to 140 °C under an Ar atmosphere, followed by dropwise injection of 2 mL of 0.8 M DMTU dissolved in OLA using a syringe pump at an injection rate of 4 mL/h. The solution temperature was maintained at 140 °C for 30 min after the injection

was completed. The solution was then cooled to room temperature and centrifuged to remove large particles. In the purification process, the OLA–$AgInS_2$ QDs were precipitated using the smallest possible amount of methanol followed by centrifugation, and the precipitate was dispersed again in hexane.

2.2.4 Synthesis of OLA–capped $AgInS_2/GaS_y$ core/shell QDs

OLA–capped $AgInS_2$ (OLA–$AgInS_2$) QDs were synthesized according the literature with a slight modification.[76] Typically, Ag(OAc) (0.8 mmol), $In(OAc)_3$ (0.8 mmol), and DDT (2.4 mmol) were mixed with OLA (16 mL) in a two-necked round-bottom flask. The mixture was degassed under vacuum at 120 °C for 5 min. The solution was rapidly heated to 140 °C under an Ar atmosphere, followed by dropwise injection of 2 mL of 0.8 M DMTU dissolved in OLA using a syringe pump at an injection rate of 4 mL/h. The solution temperature was maintained at 140 °C for 30 min after the injection was completed. The solution was then cooled to room temperature and centrifuged to remove large particles. In the purification process, the OLA–$AgInS_2$ QDs were precipitated using the smallest possible amount of methanol followed by centrifugation, and the precipitate was dispersed again in hexane.

2.2.5 Ligand exchange of QDs

The OLA–$AgInS_2/GaS_y$ QDs (0.4 mL) were precipitated using ethanol followed by centrifugation. The precipitate was mixed with an ethanolic solution of 6AH (1.0 mL; 0.5 M) and heated until the solution became clear. Excess hexane was added to precipitate the 6AH–capped $AgInS_2/GaS_y$ (6AH–$AgInS_2/GaS_y$) QDs. The solid QDs were recovered by centrifugation and dispersed in methanol (0.4 mL).

2.2.6 Synthesis of QDs/InMOFs composites

$In(NO_3)_3{\cdot}3H_2O$ (0.158 g, 0.5 mmol) was dissolved in methanol in a 20-mL glass vial (5 mL), and the solution pH was varied by adding TMAH to achieve pH = 1.8, 2.4, 3.0, and 3.3. This solution was subsequently mixed with the methanolic solution of the

6AH–$AgInS_2/GaS_y$ QDs (0.3 mL) and stirred for 3 min. The methanolic solution of fumaric acid (0.058 g, 0.5 mmol) was added to the solution that contained the QDs and In^{3+} ions, and the solution mixture was left undisturbed for 10 min. The orange powder of the $AgInS_2/GaS_y$ core/shell QDs incorporated into the InMOFs ($AgInS_2/GaS_y$@InMOFs composite) were collected by centrifugation followed by three times of washing using methanol and drying overnight under a reduced pressure. Synthesis of the InMOFs only was performed using the same procedure without TMAH and QDs.

2.3 Result and discussion

2.3.1 Optical properties and morphology of $AgInS_2/GaS_y$ QDs

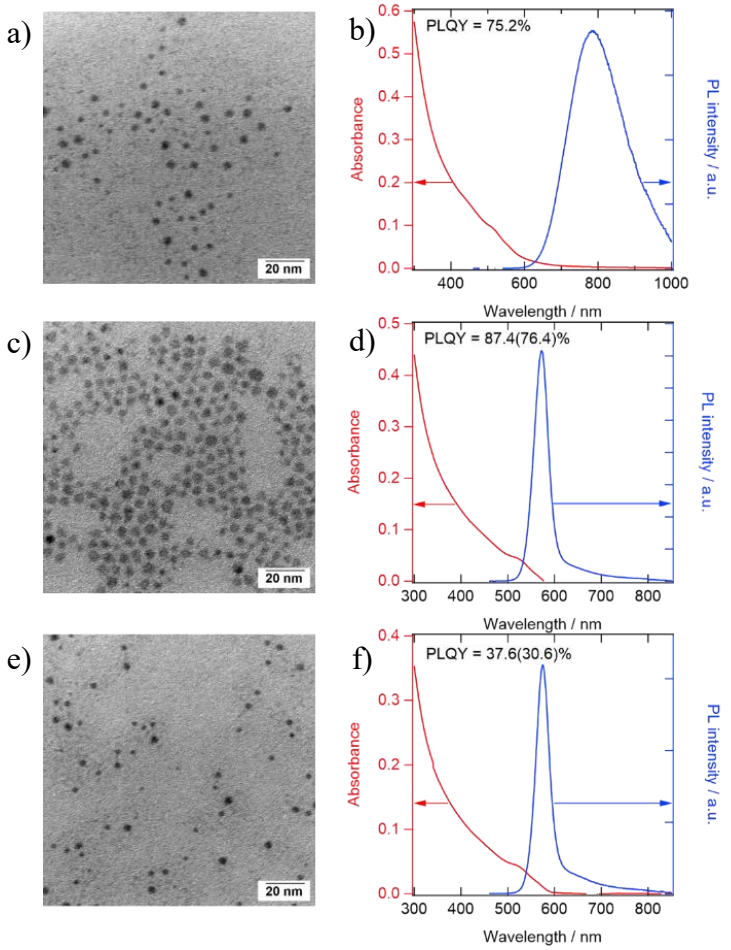

Figure 2-1 (a, c, e) TEM images and (b, d, f) UV-vis and PL spectra of the (a, b) OLA-$AgInS_2$ QDs, (c, d) OLA–$AgInS_2/GaS_y$ QDs, and (e, f) 6AH–$AgInS_2/GaS_y$ QDs. The PLQYs are displayed in the spectra that indicate the values corresponding to the band-edge emission in brackets.

Figure 2-1a and 2-1c show the TEM images of the OLA–$AgInS_2$ QDs and band-edge-emitting OLA–$AgInS_2$/GaS_y QDs, respectively. Figure 2-1b and 2-1d show the corresponding optical spectra. After formation of the GaS_y shell, the average particle size of the QDs increased from 3.9 to 4.7 nm. Simultaneously, the spectrally broad PL values of the OLA–$AgInS_2$ QDs were completely changed to a narrow band-edge emission centered at 574 nm. The full width at half maximum (FWHM) of the PL spectra decreased from 180 to 36 nm. The overall PLQY slightly increased from 75.2% to 87.4%, and the value was 76.4% when the wavelength region was limited to the band-edge emission. These results indicated that the defect sites on the surface of the $AgInS_2$ QDs were almost completely removed by coating with GaS_y shells. In the synthesis of InMOFs in methanol, the OLA–capped QDs were only soluble in low-polarity solvents such as hexane and chloroform and were insoluble in methanol. Therefore, changing the solubility nature of the QDs was necessary using the ligand exchange prior to the formation of the composite. I previously used pyridine and its derivative to disperse the CdSe/ZnS core/shell QDs in alcohol and DMF, and these attempts were partially successful. Meanwhile, the PLQY of the QDs decreased to less than half.[90,91] However, the $AgInS_2$/GaS_y core/shell QDs became totally non-luminescent after the ligand exchange to pyridine probably because of the insufficient capping by the weakly coordinating bulky ligands, which led to hydrolysis of the GaS_y shells. As a result of our attempts to find suitable capping ligands, 6AH was determined to maintain the PL after the ligand exchange. Figure 2-1e and 2-1f show the TEM image and optical spectra of the 6AH–$AgInS_2$/GaS_y core/shell QDs, which were taken after they were subjected to the ligand exchange reaction. The core/shell QDs maintained their particle shape, and no traces of aggregation were found during the reaction. In contrast, the solubility was significantly changed. The QDs became insoluble in hexane and alternatively became well soluble in methanol, which indicated the attachment of 6AH by directing its hydroxyl group outward. The shapes of the absorption and PL spectra before (Figure 2-1d) and after (Figure 2-1f) the ligand exchange process was mostly identical, whereas the value of PLQY decreased from 87.4% to 37.6%. The decrease in PLQY might be

caused by the increase in the number of nonradiative recombination centers on the surface of the shell due to the decrease in the density of the surface ligands.[92,93] However, PLQY in the band-edge-emission moiety remained at 30.6%, and this value was sufficiently high to proceed with the subsequent experiments.

2.3.2 Encapsulation of QDs in InMOFs

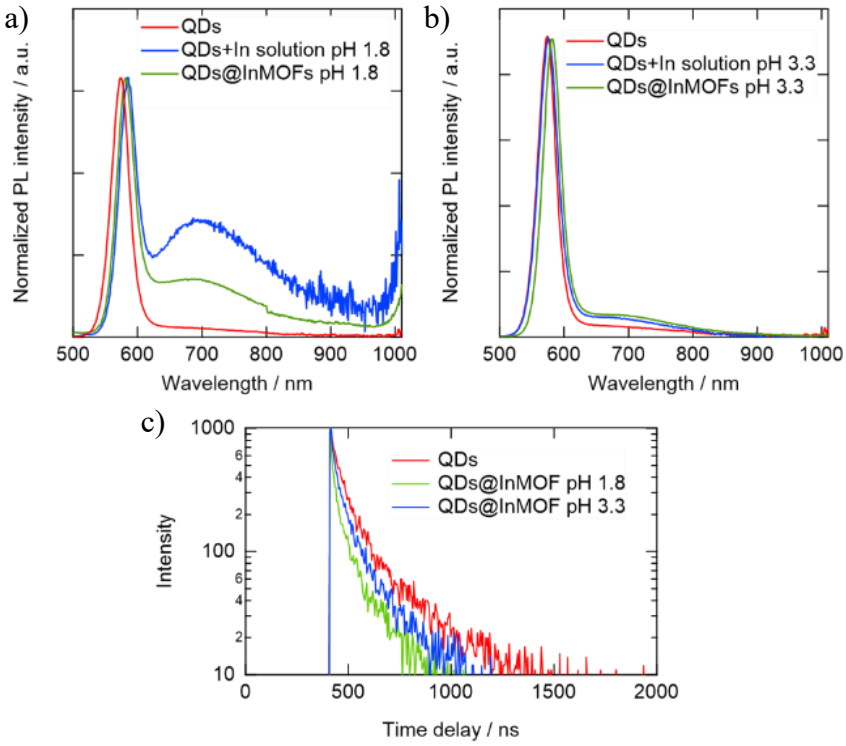

Figure 2-2 Intensity-normalized PL spectra of (red lines) the 6AH–capped QDs solution, after mixing with (blue lines) the $In(NO_3)_3$ solution and (green lines) PL spectra of the solid sample of the QDs@InMOFs composites. The pH value of the $In(NO_3)_3$ solution is (a) uncontrolled (pH = 1.8) and (b) increases to pH = 3.3 by TMAH. (c) PL-decay curves of (red) the 6AH–capped QDs solution and (solid samples) QDs@InMOFs composites prepared at (green) pH = 1.8 and (blue) pH = 3.3.

Figure 2-2a shows the PL spectra of the as-prepared 6AH–$AgInS_2/GaS_y$ core/shell QDs, those after mixing with the methanolic solution that contained $In(NO_3)_3$, and those after encapsulation by InMOFs. Unfortunately, the PL spectrum of the core/shell QDs varied, and the broad defect emission significantly increased to 689 nm after mixing with the methanolic solution of $In(NO_3)_3$, probably due to the damage of the GaS_y shells.

The causes of the deterioration of the QDs were the low-pH value (pH = 1.8) of the $In(NO_3)_3$ solution, which resulted from the hydrolysis of $In(NO_3)_3$ that generated protons in the solution,[94] and the GaS_y shells that were considered to be dissolved by releasing hydrogen sulfide under this low-pH condition. To avoid shell degradation, the acidity of the $In(NO_3)_3$ solution was reduced by adding TMAH, which is the simplest ammonium base that has been occasionally used during synthesis of MOFs, before mixing it with the QD solution.[95–97] Although increasing the pH value to the original methanolic solution of the 6AH–QDs (pH = 9.2) was ideal, the condition of higher than pH = 3.4 resulted in the formation of In hydroxide [$In(OH_3)$]. Therefore, I performed fine tuning and set the value at pH = 3.3, which could maintain the band-edge emission while preventing hydroxide formation. The value of PLQY was increased from 37.6% (6AH–QDs) to 49.9% after mixing with the $In(NO_3)_3$ solution (Figure 2-2b). The enhancement of PLQY appeared to result from the interaction of the GaS_y shell with the Lewis acidic In(III) species, which could passivate the unsaturated sulfur sites on the surface of the metal chalcogenide semiconductors.[98] Subsequently, the aforementioned two samples [with uncontrolled (1.8) and controlled pH (3.3)] were subjected to encapsulation by the InMOFs. In both cases, the pale orange powder was obtained after the QDs/$In(NO_3)_3$ mixture solution was mixed with a solution of fumaric acid, indicating the formation of InMOFs under both pH conditions, as will be mentioned later using XRD patterns and TEM images. No residual QDs were found in the solution phase or as a dark-color precipitate after the pale orange powder was removed. The composite sample, which was synthesized without pH control, exhibited a nonnegligible increase in the broadband defect emission (Figure 2-2a), whereas the ratio of the defect emission slightly decreased compared with the spectrum before encapsulation by InMOFs. In contrast, the pH-controlled sample mostly maintained its spectral shape with no obvious increase in the defect emission after encapsulation by the InMOFs. The PLQY of the sample (pH = 3.3) was 12.6%, and the band-edge peak wavelength was 581 nm with an FWHM value of 33 nm, i.e., the peak wavelength was red-shifted by 7 nm from 574 nm, and the FWHM was reduced from 36 nm compared with that of the

6AH–capped QDs in methanol (Table 2-1). The red shift in the emission spectra of the composites could be attributed to the Stark effect, which was caused by the changes in the dielectric environment around the QDs, which was previously observed as a solvatochromic effect of the QDs.[99] Whereas the aggregation-induced red shift has been frequently reported,[100] severe aggregation was not observed, as will be mentioned later using the TEM images.[101] In addition, the FWHM became slightly narrower after incorporation into the InMOFs.

Table 2-1 Optical parameters of PL for QDs, InMOFs, and QDs@InMOFs composites.

Samples	**Particle Size (nm)**	**Emission (nm)**	**FWHM (nm)**	**PLQY (%)**	
				Band Edge	Overall
OLA-$AgInS_2$	3.29±0.51	786	180.3	-	75.2
OLA-$AgInS_2/GaS_y$	4.89±0.74	574	35.9	76.4	87.4
6AH-AgInS2/GaS_y	3.60±0.64	575	36.4	30.6	37.6
InMOFs	536±90	-	-	-	-
QDs@InMOFs pH 1.8	266±27	581	33.3	1.4	3.7
QDs@InMOFs pH 2.4	34.2±8.3	581	33.6	4.6	8.9
QDs@InMOFs pH 3.0	34.2±7.3	581	32.6	5.3	10.7
QDs@InMOFs pH 3.3	40.8±10.4	581	33.4	8.1	12.6

To the best of our knowledge, the decrease in FWHM of the PL upon solidification of the QDs has not been reported. However, as an example of a similar phenomenon, a previous report was presented on the narrowing of the PL spectral width of the CdSe QD ensemble when the sample temperature was reduced from 300 to 4 K

due to the decrease in the spectral diffusion resulting from the smaller fluctuations of local environments.[102] These results allowed the speculation that in the InMOFs, the fluctuations in the dielectric environment around the QDs were smaller than those in the solvents, which led to the decrease in both the spectral diffusion and PL line width. More importantly, the changes in the PL property, i.e., the changes in the local environment around the QDs, provided evidence that direct interaction between the QDs and InMOFs occurred. Figure 2-2c shows the PL-decay curves of the 6AH-capped QDs and QDs@InMOFs composites. These curves could be well fitted using the following biexponential equation:

$$I(t) = A_1 exp\left(-\frac{t}{\tau_1}\right) + A_2 exp\left(-\frac{t}{\tau_2}\right)$$

where $I(t)$ is the intensity at time t, A_1 and A_2 represent the normalized amplitudes, and τ_1 and τ_2 represent the lifetime constants of the PL emission of each component. A summary of the fitting results is listed in Table 2-2. For the 6AH-capped QDs, the fast (61.1 ns) and slow (349.4 ns) components were present, which were on the same order but longer than the OA-capped QDs (Table 2-2). These changes appeared to be due to the variations in the electric environment around the QDs. The decay curves of the QDs@InMOFs solid samples, which were synthesized without pH control, indicated the decrease in the lifetimes (22.6 and 168.4 ns in the shorter and longer lifetime components, respectively) compared with those of the 6AH-capped QDs. These results indicated the generation of defects on the QD surface due to the QD damage under the low-pH condition. In contrast, for the QDs@InMOFs synthesized at pH = 3.3, the decrease in the lifetime was less significant (41.7 and 254.0 ns in the first and second components, respectively), which implied that the surface of the QDs was better maintained than that of the samples prepared at pH = 1.8.

Table 2-2 PL decay components for pristine QDs and QDs@InMOFs composites

Sample	λ_{PL} (nm)	$<\tau>$ (ns)	τ_1 <ns>	A_1	τ_2 <ns>	A_2	X^2
OLA–$AgInS_2/GaS_y$	573	84.26	46.18	945.36	172.39	109.43	1.00
6AH–$AgInS_2/GaS_y$	575	189.85	61.06	861.57	349.43	121.5	1.15
QDs@InMOFs pH 1.8	581	101.86	22.56	936.46	168.41	146.69	0.94
QDs@InMOFs pH 3.3	581	139.16	41.67	905.61	254	126.14	0.90

2.3.3 Optical and structural properties of QDs@InMOF composite

Figure 2-3 shows the diffuse reflection spectra of the QDs@InMOFs solid samples (converted using the Kubelka–Munk function) and the PL spectra prepared at different pH conditions from pH = 1.8 (uncontrolled) to pH = 3.3. All composite samples exhibited absorption features of the $AgInS_2/GaS_y$ core/shell QDs, which demonstrated a monotonic increase toward a shorter wavelength with an onset at 600 nm (Figure 2-3a). However, the Kubelka–Munk intensity of the pH = 1.8 sample was significantly lower than those of the other three composites prepared at a pH value higher than 2.4. The decrease in the absorption suggested the dissolution of the QDs under the strong acidic condition, which was sufficiently significant to damage not only the amorphous GaS_y shells but also the $AgInS_2$ cores. The damage of the nanoparticles was mitigated at a higher pH range, and the PLQY steadily increased with the increase in the pH value (Table 2-1). Meanwhile, pH = 3.3 represented the highest possible condition to prevent the formation of $In(OH)_3$.

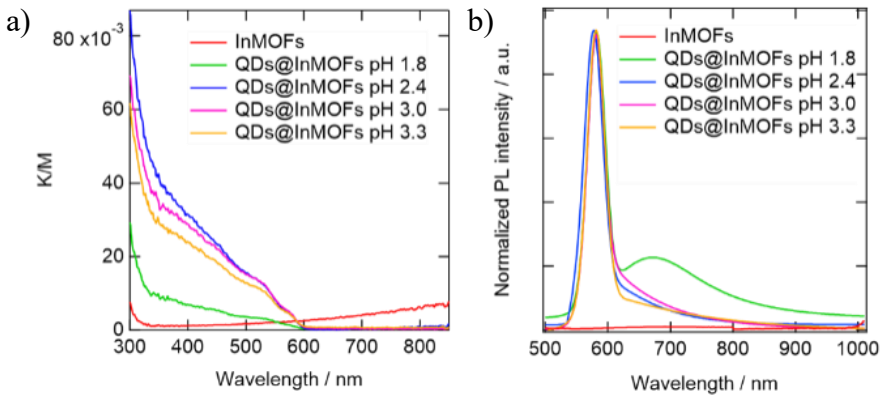

Figure 2-3 (a) Diffuse reflection and (b) PL spectra of the InMOFs and QDs@InMOFs composite under different synthetic pH values.

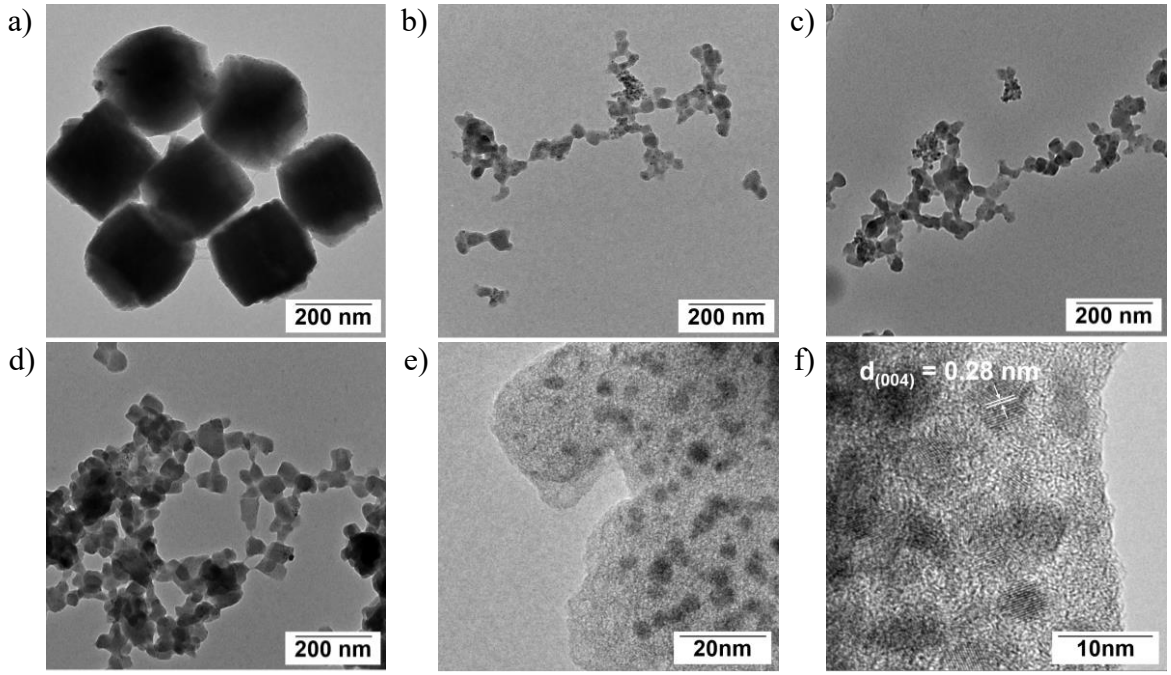

Figure 2-4 TEM images of the QDs@InMOFs composite synthesized at pH values of (a) 1.8, (b) 2.4, (c) 3.0, and (d) 3.3. (e) and (f) HRTEM images of the QDs@InMOFs composite (pH 3.3).

The morphology of the QDs@InMOFs composites prepared at different pH conditions were investigated using 100-kV TEM (Figure 2-4a to 2-4d) and HRTEM (Figure 2-4e and 2-4f). Under all conditions, rhombic polyhedral objects were observed, which were the crystalline particles of the InMOFs, whereas the size of the objects was significantly different according to their pH values. The QDs were barely visible as dark spots in the 100-kV TEM images, which randomly dispersed over the InMOFs

structures. The structures prepared at pH = 1.8 (uncontrolled) exhibited a clearly faceted shape with an average size of 266 nm. At higher pH values, the structure size decreased to 34.2 nm in the samples with pH = 2.4 and 3.0 and to 40.8 nm in those with pH = 3.3 when the individual component of the interconnected structure was measured. The connected structures of the pH-controlled samples reflected higher surface energy that was caused by both the small size and the deprotonation of the terminal fumaric acid moieties and adsorption of TMAH cation, which altered the affinity (or surface energy) of methanol.[103] The generation of smaller structures at higher pH values could be explained by the deprotonation of fumaric acid, which accelerated the In-fumarate complexation when these species were mixed. Under such condition, nucleation rapidly occurred to deplete the raw materials before growth, resulting in the formation of smaller MOFs crystals.[104] The XRD patterns indicated the formation of the InMOFs in all pH conditions (Figure 2-5). The deterioration of the structure was not found for all samples whereas the measurements were performed in air in a dry condition.

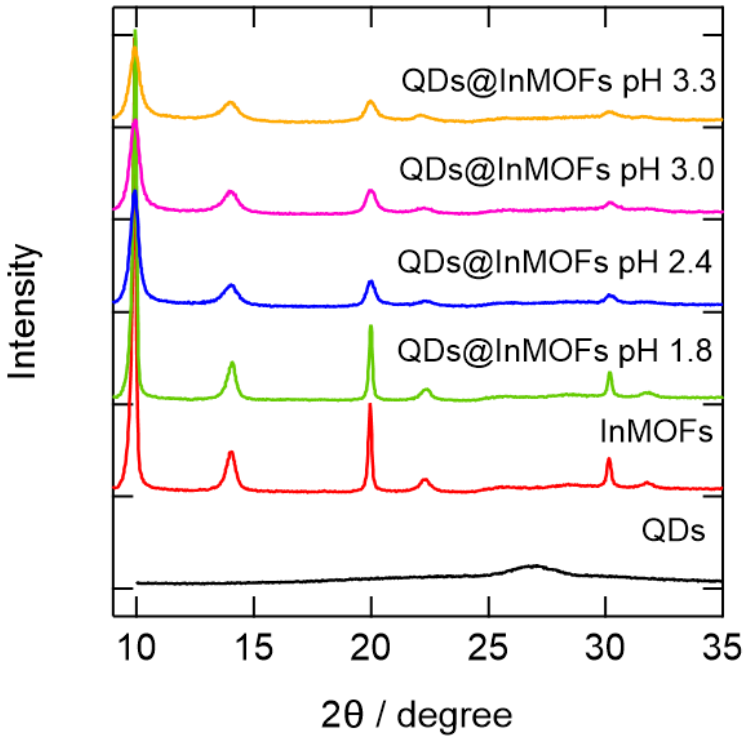

Figure 2-5 XRD patterns of the $AgInS_2/GaS_y$ core/shell QDs, InMOFs, and QDs@InMOFs composites at different synthetic pH values.

More importantly, the pale orange color of the composites did not change during washing with methanol, which suggested that the QDs were encapsulated in InMOFs instead of just attaching to their surface. The QD encapsulation was confirmed by the HRTEM images (Fig. 2-4e and 2-4f), which exhibited the morphology of the QDs@InMOFs synthesized at pH = 3.3. Because the QDs contained heavier elements (Ag, In, and Ga) at higher density than the InMOFs, they appeared as circular dark places because of compositional contrast. At higher magnification, 0.28-nm lattice fringes, which corresponded to the (004) plane of the tetragonal $AgInS_2$, were visible in these dark places, whereas no traces of crystalline structures were observed in the InMOF matrices (Figure 2-4f). According to previous reports, observation of the crystal structure of MOFs by HRTEM were generally difficult because of the severe damage by high electron dose unless the materials were cooled to liquid-nitrogen temperature to prevent bond cleavage and destruction of local structures.[105,106] The presence of QDs in the structure was further evidenced by the detection of Ag, Ga, and S using ICP measurements. The atomic ratios were similar to one another (Table 2-3).

Table 2-3 The atomic ratio (%) of each component in QDs@InMOFs composites

Sample	S	Ag	In	Ga
QDs@InMOFs pH 1.8	1.47	0.55	97.50	0.47
QDs@InMOFs pH 2.4	1.78	0.49	97.26	0.48
QDs@InMOFs pH 3.0	2.43	0.70	96.16	0.72
QDs@InMOFs pH 3.3	2.61	0.69	96.03	0.67

2.3.4 PL stability of the QDs@InMOFs composite

The relatively low stability of the GaS_y shell when stored in the solution has been a matter of concern for practical applications.[77] Whereas this low stability has gradually been improved, e.g., by making thicker shells,[107] a fundamental solution is still required for better usability of these materials. The deterioration issue is more significant after the QDs are subjected to the ligand exchange. Figure 2-6a shows the relative PLQY

values of the overall emission range and band-edge emission during storage at 25 °C. The methanolic solution of the 6AH–capped $AgInS_2/GaS_y$ QDs rapidly deteriorated within hours and finally became nonluminescent after 24 h. The speed of deterioration was much faster than that reported in our recent study, which indicated the non-ignorable effects of the ligand exchange to shorter 6AH and storage in high-polarity solvents. On the other hand, the relative PLQY values of the QDs@InMOFs composite stored as a solid remained constant, and no decrease in the band-edge PL was observed for 7 days. These results revealed that the QDs@InMOFs composite exhibited significantly higher stability than the 6AH-capped QDs, and the InMOFs acted as a protecting layer for the GaS_y shells without damaging their properties when the two species made contact. Whereas the stability in a longer time span is under investigation, the same sample partly maintained the band-edge emission after storage for 10 months (Figure 2-6b).

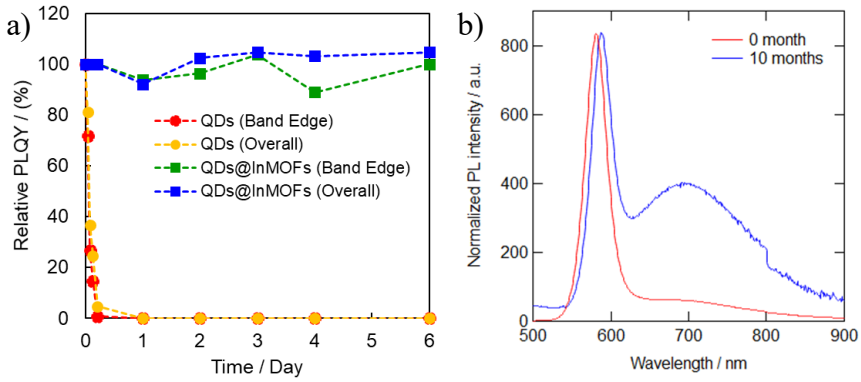

Figure 2-6 (a) Variations in PLQY of the 6AH-capped QDs (in methanol) and QDs@InMOFs composite synthesized at pH = 3.3. The variations in the overall and band-edge PLQY are separately displayed. (b) PL spectra of QDs@InMOFs at different time.

2.4 Conclusion

In summary, I have successfully improved the stability of $AgInS_2/GaS_y$ QDs that exhibited band-edge emission via encapsulation of the QDs into In-fumarate MOFs. Before encapsulation, the QDs were ligand-exchanged to 6AH to improve their dispersibility in methanol, which was used for the growth of InMOFs. The pH value of the solution was increased to 3.3 to prevent damage to the GaS_y shell when the QDs

were mixed with the solution of In nitrate and fumaric acid. The resulting QDs@InMOFs composites preserved the PL characteristics of the $AgInS_2/GaS_y$ QDs, and the PLQY value of the solid sample was 12.6%. The structural characterizations using TEM indicated that the QDs were homogeneously distributed in the InMOFs, and the XRD patterns indicated that no traces of alterations were observed in the crystal structure of the InMOFs even when they formed composites with the QDs. Although the structural weakness of the amorphous GaS_y shells has been a matter of concern, the stability of the encapsulated QDs was significantly higher than that of the QDs in the methanol solution, and the band-edge PL remained unchanged after 7 days. These results indicated that the InMOFs are useful for protecting the QDs without causing alteration of the GaS_y shell properties.

Chapter 3

Facile high-yield synthesis of Ag-In-Ga-S quaternary quantum dots and coating with gallium sulfide shells for narrow band-edge emission

3.1 Introduction

The synthesis of AIGS quaternary QDs is still challenging because of the difference in their chemical reactivity. Typically, silver possesses the highest activity toward the reaction with sulfur compared to indium. As a result, silver sulfide (Ag_2S) nanoparticles are preferentially formed, reducing the product yield of the target QDs. Therefore, suppression of silver reactivity has been used to overcome this issue using alkanethiols, which strongly bind with Ag^+.[108] However, the reduction of reactivity decreases the nucleation speed, leading to the formation of polydisperse QDs. Therefore, the reactivity of Ag^+ needed to be maintained to produce QDs with monodispersity. In recent studies, the synthesis of $AgIn_xGa_{1-x}S_2$ alloy QDs in tetragonal phase, which emit green PL after coating the GaS_y shell, was demonstrated by heating the mixture of Ag(OAc), $In(OAc)_3$, and gallium tris(N,N'-diethyldithiocarbamate) [$Ga(DDTC)_3$].[77,107] In this case, the Ag(I) and In(III) were involved in the reaction of $Ga(DDTC)_3$, which is an efficient source of GaS_y by itself, to produce $AgIn_xGa_{1-x}S_2$ QDs. However, the reaction produced an unacceptable amount of precipitate, and product yield was only 15% based on Ag.

In this chapter, I demonstrated a new approach for synthesizing the $AgIn_xGa_{1-x}S_2$ alloy QDs at high product yield (60%) without generating any precipitate. The rapid nucleation of the Ag_2S intermediate nanoparticles and the conversion to $AgIn_xGa_{1-x}S_2$ QDs occurred in one batch by injecting the Ag(OAc) solution into the mixture solution of dithiocarbamate complexes of the In(III) and Ga(III). The resulting $AgIn_xGa_{1-x}S_2$ core QDs exhibited an orange-colored emission whose spectral shape is characteristic of the defect emission of the groups 11–13–16 semiconductor QDs.[77,109,110] After

coating of the GaS_y shells, the core/shell QDs exhibited an intense band-edge emission in the green region with the PLQY higher than 50%.

3.2 Experimental section

3.2.1 Materials

Ag(OAc) and $InCl_3$ were purchased from Mitsuwa Chemical. diethylammonium *N,N'*-diethyldithiocarbamate (DEA–DDTC) and 35% hydrochloric acid (HCl) solution were purchased from Fujifilm–Wako. $GaCl_3$ and tri-*n*-butylphosphine (TBP) was purchased from TCI. $In(OAc)_3$ and $Ga(acac)_3$ were obtained from Sigma–Aldrich–Merck. OLA (Fujifilm-Wako) was purified by vacuum distillation in the presence of calcium hydride (Fujifilm-Wako).

3.2.2 Instruments

UV–vis absorption and PL spectra were obtained using a JASCO V-670 UV–vis spectrophotometer and a JASCO FP-8600 spectrofluorometer, respectively. PLQY measurements were carried out by a Hamamatsu PMA12 spectrofluorometer equipped with an integrating sphere. PL decay curves were recorded using a time-correlated single-photon counting setup (Hamamatsu, Quantaurus-Tau). The QD morphologies were observed using a TEM instrument (Hitachi, H-7650) at an acceleration voltage of 100 kV, whereas a HRTEM images were captured using a 200 kV TEM (JEOL, JEM-2100). Powder XRD analysis was performed on a Rigaku SmartLab X-ray diffractometer equipped with a parallel beam/parallel slit analyzer. The surface chemical electronic state and composition of the QDs were measured by a Shimadzu KRATOS AXIS-165x XPS equipped with an aluminum target. The chemical composition of QDs was determined by an inductively coupled plasma atomic emission spectrometer (ICP-AES, Shimadzu, ICPS-7510) after repeated isolation of the QDs and mineralization in a hot concentrated nitric acid.

3.2.3 Synthesis of $Ga(DDTC)_3$ and $In(DDTC)_3$

In a nitrogen glove box, $GaCl_3$ (1 g) was dissolved in dehydrated toluene (100 mL), followed by addition of DEA–DDTC (3.8 g) with vigorous stirring. The solution was stirred for another 3h and took out from the glove box. Toluene and diethylammonium chloride residue were totally removed by a rotary evaporator, and the white powder was further dried under 100 Pa at 60 °C for 1h. The powder was dissolved in the least amount of chloroform with heating, and then cooled to room temperature. White needle-like crystals were gradually generated, which were further incubated in the refrigerator (5 °C) overnight. The product was recovered by filtration with a yield ca. 90% To synthesize $In(DDTC)_3$, $InCl_3$ and dehydrated tetrahydrofuran was used instead of $GaCl_3$ and toluene, respectively.

3.2.4 Synthesis of $AgIn_xGa_{1-x}S_2$ core QDs

$In(OAc)_3$ (0.15 mmol, 43.5 mg) and $Ga(DDTC)_3$ (0.4 mmol, 205 mg) were mixed with OLA (10 mL) in a 50 mL two-necked flask, followed by heating at 80 °C under vacuum for 5 min. After completely dissolving the white powders, the flask was filled with argon and the controller was set at either 150 °C, 180 °C, or 200 °C (Sample 1–3, Table 3-1). The actual heating rate was 30 °C/min on average whereas it was not actively controlled. Separately, Ag(OAc) (0.25 mmol, 41.7 mg) was dissolved in OLA (1 mL) and the solution was loaded in a gastight syringe. When the temperature of the In/Ga solution reached to 130 °C, the Ag(OAc) solution was swiftly injected into the flask. The temperature was dropped by ca. 5 °C upon injection but immediately recovered and increased to the set temperature. After heating for another 20 min. The solution was cooled under 50 °C and the nanoparticle portion was isolated by precipitating with acetone and ethanol, then dispersed in hexane. In order to study the effects of the starting material, $InCl_3$ and $In(DDTC)_3$ were used instead of $In(OAc)_3$. The reaction temperature was set at 200°C (sample 4-9, Table 3-1)

3.2.5 Formation of GaS_y shell

For sample 1–3, $Ga(acac)_3$ (0.15 mmol, 55 mg), $Ga(DDTC)_3$ (0.05 mmol, 26 mg), and DMTU (0.15 mmol, 10 mg) were dissolved in 10 mL of OLA, to which the 1/5

amount of the $AgIn_xGa_{1-x}S_2$ core were introduced. Under an Ar atmosphere, the mixture solution was heated rapidly to 230 °C and subsequently increased to 280 °C at a rate of 2 °C/min. The heating mantle was removed off and the solution was cooled under 100 °C. A 50 μL of 35% HCl aqueous solution was injected into the flask, followed by dehydration by vacuum at 100 °C. The solution heated again to 260 °C and the temperature was maintained for 30 min. After cooling to room temperature, an excess methanol was added to precipitate the nanoparticle portion. The solid was recovered by centrifugation and dissolved in chloroform.

For sample 4–8, the $GaCl_3$– OLA solution (0.2 mmol/mL) was used instead of HCl solution. When the core/shell QD solution reached 280 °C, 1.5-mL OLA solution of $GaCl_3$ was injected. The heating was continued for another 30 min. Afterward, the purification of the core/shell QDs was performed the same way as sample before.

For sample 9, 1 mL of $GaCl_3$ OLA solution (0.2 mmol/mL) and powdery $Ga(DDTC)_3$ (0.1 mmol, 52 mg) were mixed with OLA (9 mL) and evacuated at 80 °C. Under Ar atmosphere, the temperature controller was set to 230 °C. When the actual temperature reached 160 °C, the $AgIn_xGa_{1-x}S_2$ core dissolved in hexane was injected drop wise, typically taking 1 min. The temperature was rapidly increased to 230 °C, and afterward to 280 °C at a rate of 2 °C/min. When the solution temperature reached 280 °C, 1-mL of the $GaCl_3$/OLA solution was injected. The heating was continued for another 30 min before cooling to room temperature. Afterward, the purification of the core/shell QDs was performed the same way as before.

3.2.6 Alkylphosphine treatment (Applied to the sample 4 and 5)

0.1 mL of TBP was added to the 1-mL chloroform solution of the $GaCl_3$-treated, purified core/shell QDs, which was incubated at room temperature. The PLQY increased gradually and remained unchanged in 1 h.

Table 3-1 List of synthetic conditions and optical properties of $AgIn_xGa_{1-x}S_2$ core and $AgIn_xGa_{1-x}S_2/GaS_y$ core/shell QDs.

Sample No.	Core				Core/shell			
	Materials and conditions	**Peak**	**FWHM**	**QY**	**Materials and conditions**	**Peak**	**FWHM**	**QY**
1	Ag(OAc) (0.25 mmol), $In(OAc)_3$ (0.15 mmol), and $Ga(DDTC)_3$ (0.4 mmol); 150 °C	601 nm	127 nm	9%	Core + $Ga(acac)_3$ (0.15 mmol), $Ga(DDTC)_3$ (0.05 mmol), DMTU (0.15 mmol), and post HCl (0.48 mmol); 260 °C for 30 min.	499 nm	35 nm	21%
2	Ag(OAc) (0.25 mmol), $In(OAc)_3$ (0.15 mmol), and $Ga(DDTC)_3$ (0.4 mmol); 180 °C	588 nm	112 nm	21%	Core + $Ga(acac)_3$ (0.15 mmol), $Ga(DDTC)_3$ (0.05 mmol), DMTU (0.15 mmol), and post HCl (0.48 mmol) 260 °C for 30 min.	504 nm	31 nm	20%
3	Ag(OAc) (0.25 mmol), $In(OAc)_3$ (0.15 mmol), and $Ga(DDTC)_3$ (0.4 mmol); 200 °C	594 nm	113 nm	22%	Core + $Ga(acac)_3$ (0.15 mmol), $Ga(DDTC)_3$ (0.05 mmol), DMTU (0.15 mmol), and post HCl (0.48 mmol); 260 °C for 30 min.	507 nm	31 nm	25%
4	Ag(OAc) (0.25 mmol), $InCl_3$ (0.15 mmol), and $Ga(DDTC)_3$ (0.4 mmol); 200 °C	655 nm	139 nm	25%	Core + $Ga(acac)_3$ (0.15 mmol), $Ga(DDTC)_3$ (0.05 mmol), DMTU (0.15 mmol), and post $GaCl_3$ (0.3 mmol); 280 °C for 30 min.	503 nm	33 nm	25%
5	Ag(OAc) (0.25 mmol), $InCl_3$ (0.2 mmol), and $Ga(DDTC)_3$ (0.4 mmol); 200 °C	619 nm	131 nm	34%	Core + $Ga(acac)_3$ (0.15 mmol), $Ga(DDTC)_3$ (0.05 mmol), DMTU (0.15 mmol), and post $GaCl_3$ (0.3 mmol) 280 °C for 30 min.	506 nm	35 nm	44%
6	Ag(OAc) (0.25 mmol), $InCl_3$ (0.25 mmol), and $Ga(DDTC)_3$ (0.35 mmol); 200 °C	614 nm	132 nm	42%	Core + $Ga(acac)_3$ (0.15 mmol), $Ga(DDTC)_3$ (0.05 mmol), DMTU (0.15 mmol), and post $GaCl_3$ (0.35 mmol); 280 °C for 30 min.	514 nm	34 nm	54%
7	Ag(OAc) (0.25 mmol), $InCl_3$ (0.3 mmol), and $Ga(DDTC)_3$ (0.3 mmol); 200 °C	534 nm 640 nm	37 nm 155 nm	25%	Core + $Ga(acac)_3$ (0.15 mmol), $Ga(DDTC)_3$ (0.05 mmol), DMTU (0.15 mmol), and post $GaCl_3$ (0.35 mmol); 280 °C for 30 min.	543 nm	37 nm	75%
8	Ag(OAc) (0.25 mmol), $InCl_3$ (0.2 mmol), $In(DDTC)_3$ (0.1 mmol), and $Ga(DDTC)_3$ (0.3 mmol); 200 °C	633 nm	135 nm	47%	Core + $Ga(acac)_3$ (0.15 mmol), $Ga(DDTC)_3$ (0.05 mmol), DMTU (0.15 mmol), and post $GaCl_3$ (0.3 mmol); 280 °C for 30 min.	532 nm	35 nm	60%
9	Ag(OAc) (0.25 mmol), $InCl_3$ (0.2 mmol), $In(DDTC)_3$ (0.05 mmol), and $Ga(DDTC)_3$ (0.3 mmol); 200 °C	651 nm	150 nm	30%	$Ga(DDTC)_3$ (0.1 mmol), $GaCl_3$ (0.2 mmol) *Core QDs injected at 160 °C, and post $GaCl_3$ (0.2 mmol); 280 °C for 30 min.	528 nm	31 nm	53%

3.3 Result and discussion

3.3.1 Synthesis of $AgIn_xGa_{1-x}S_2$ core QDs by Ag source injection (Sample 1–3)

In conventional method,[77] the synthesis ofthe $AgIn_xGa_{1-x}S_2$ core QDs was performed by heating a mixture of Ag(OAc), $In(OAc)_3$, and $Ga(DDTC)_3$ at 150 °C. A brown turbid dispersion solution containing large particles was produced as byproducts, which needed post-synthetic size segregation (Figure 3-1a). Most of these precipitates consisted of Ag_2S nanoparticles with an average size of 17 nm and a broad size distribution. (Figure 3-2) Small black spots attached to some particles are considered Ag metal nanoparticles generated by photoreduction.

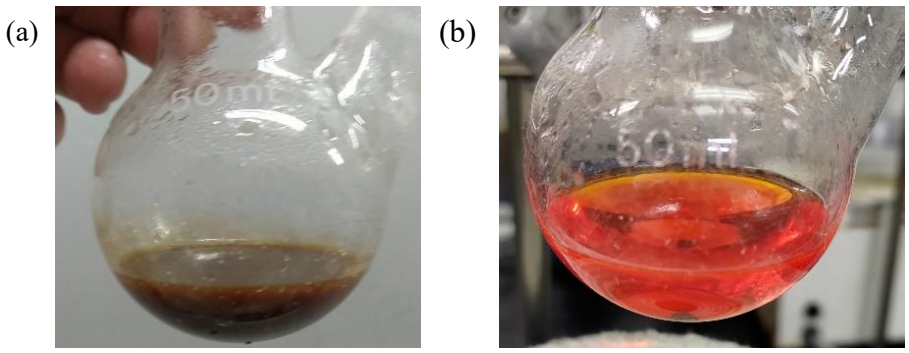

Figure 3-1 Photographs of the flask just after cooling to room temperature: (a) procedure that mixes all necessary precursors, (b) procedure involving injection of Ag(OAc) (present study).

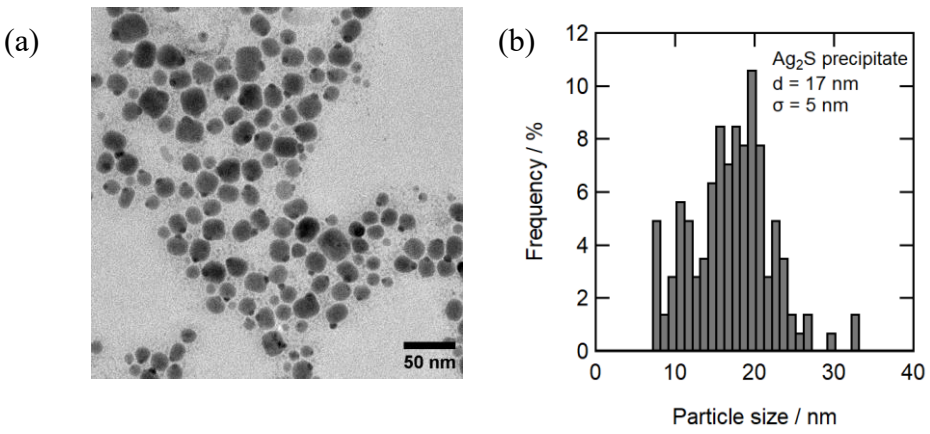

Figure 3-2 (a) TEM images of precipitate produced by heating a mixture of Ag(OAc), $In(OAc)_3$, and gallium tris(*N,N'*-diethyldithiocarbamate) ($Ga(DDTC)_3$), and (b) the corresponding size histogram.

On the contrary, the Ag source injection approach developed in this study yielded a clear orange–red solution despite using the same reagents as in the previous $AgIn_xGa_{1-x}S_2$ synthesis (Figure 3-1b and Figure 3-3a).[77] This solution exhibited an orange-colored PL with a broad spectral shape characteristic of defect PL (Figure 3-3b).

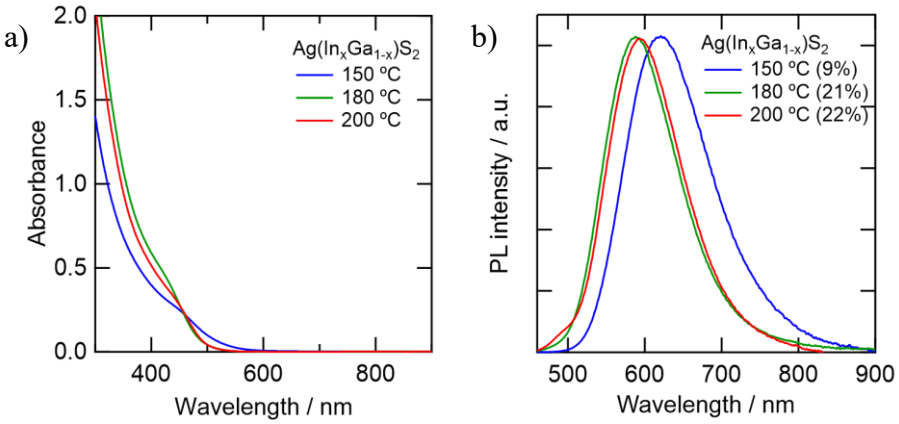

Figure 3-3 (a) UV-vis and (b) PL spectra (Ex = 450 nm) for the $AgIn_xGa_{1-x}S_2$ core synthesized at different temperatures; (blue, sample 1) 150 °C, (green, sample 2) 180 °C, and (red, sample 3) 200°C.

The XRD pattern showed the presence of tetragonal $AgIn_xGa_{1-x}S_2$, whereas its feature was slightly vague at 150 °C (Figure 3-4). When the reaction temperature was raised to 180 °C, the crystallinity was improved while maintaining the tetragonal feature. Interestingly, this contrasts with the previous finding that heating at 180 °C resulted in orthorhombic $AgInS_2$ QDs whose diameter is more than 6 nm,[76] and such core QDs were unfavorable for band-edge PL. Unlike the previous results, the injection approach maintained a small particle size of 3.4 nm even when synthesized at 180 °C and 3.9 nm at 200 °C (Figure 3-5). The absorption edge and defective PL wavelengths blue-shifted by 30 nm due to this temperature change.

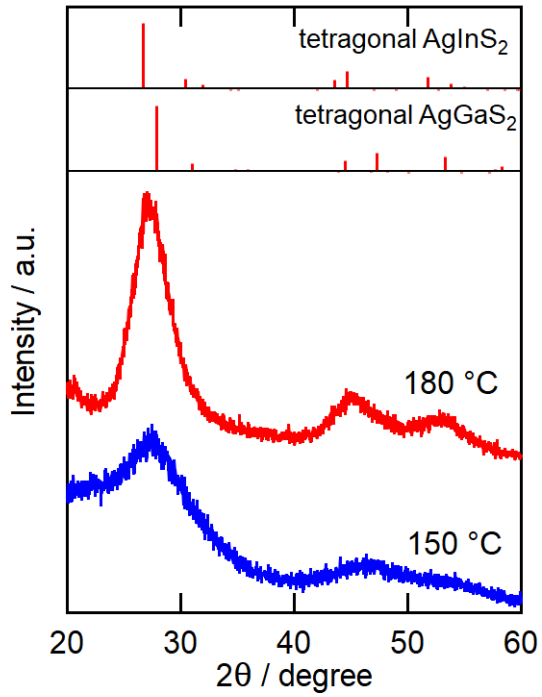

Figure 3-4 XRD patterns of $AgIn_xGa_{1-x}S_2$ QDs synthesized at (blue line) 150 °C and (red line) 180 °C. The reference data were obtained from ICSD 070-5629 and 073-1233 for $AgInS_2$ and $AgGaS_2$, respectively, both in the tetragonal phase.

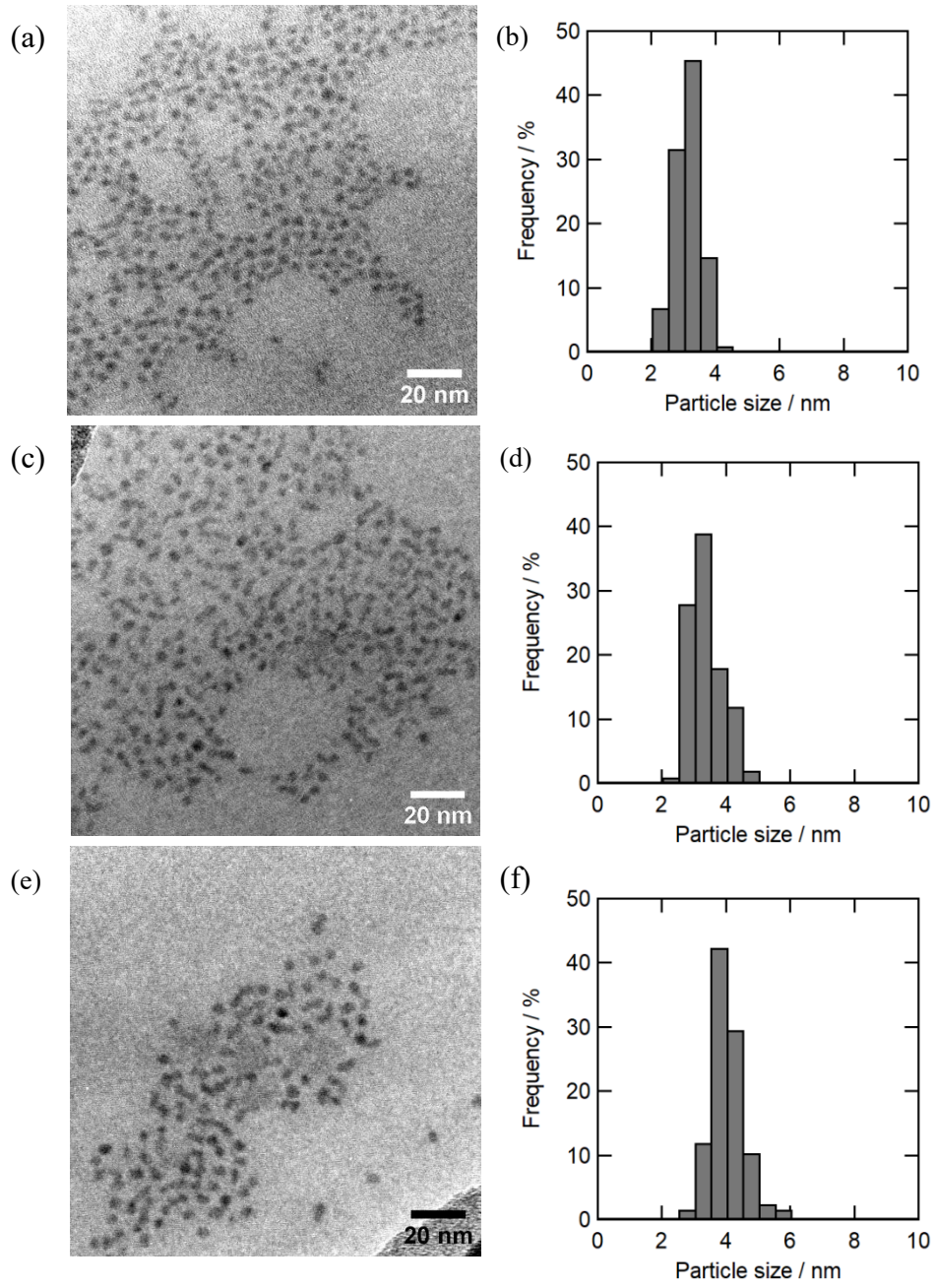

Figure 3-5. TEM images (a, c, e) and size histograms (b, d, f) of $AgIn_xGa_{1-x}S_2$ core QDs synthesized at (a, b) 150 °C (3.2 ± 0.3 nm), (c, d) 180 °C (3.4 ± 0.5 nm), and (e, f) 200 °C (3.9 ± 0.5 nm) using $In(OAc)_3$ as an indium source.

3.3.2 GaS_y shell formation and hydrochloride acid treatment

The synthesis of the GaS_y shells was conducted following the recent report by using a mixture of the purified $AgIn_xGa_{1-x}S_2$ core QDs, gallium acetylacetonate [$Ga(acac)_3$], 1,3-dimethylthiourea (DMTU), and $Ga(DDTC)_3$.[77,107] These reagents and materials were dispersed

in OLA and heated rapidly to 230 °C, thereafter to 280 °C at a rate of 2 °C/min to prevent self-nucleation of GaS_y. Figures 3-6a and 3-6b show the UV-vis and PL spectra for the $AgIn_xGa_{1-x}S_2/GaS_y$ core/shell QDs. New PL peaks with narrower spectral widths, which can be attributed to the band-edge PL, appeared on the blue sides of the defective emissions. However, the residual defect emissions were substantially high, especially when the core QDs were synthesized at lower temperatures. In addition, the PLQYs of the three samples were lower than the QDs that were prepared with the same chemicals but by mixing them all.[77] These results indicated that the structure of the QDs synthesized by injecting Ag source was somewhat different from those prepared with the mixture precursor, whereas the XRD patterns indicated the pure tetragonal $AgIn_xGa_{1-x}S_2$. According to the TEM image, the cores prepared by heating the mixture precursor were surrounded by large amorphous objects, which were attributed to excess indium gallium sulfide.[77] Contrary to these results, the Ag source injection produced well-defined particles due to a balanced use of raw materials, as described below (Figure 3-5). However, these "more exposed" particles are considered more susceptible to oxidation and other damage during purification, which may create trap levels.

A remedy to this problem lies with chloride ions. More accurately, the post-heating of the core/shell QDs above 260 °C in the presence of either hydrochloric acid (HCl, in the basic procedure) or gallium chloride ($GaCl_3$, in the modified procedure) significantly improved the PL properties. Figure 3-6c and 3-6d show the optical properties after the HCl treatment, which was added as a concentrated aqueous solution into the as-reacted crude solution of the core/shell QDs, followed by dehydration in a vacuum at 100 °C. The chloride ion is considered to exist as oleylamine hydrochloride, and no obvious variations in PL properties are observed at this stage. The improvement of band-edge PL purity and PLQY occurs during the subsequent heating at 260 °C.

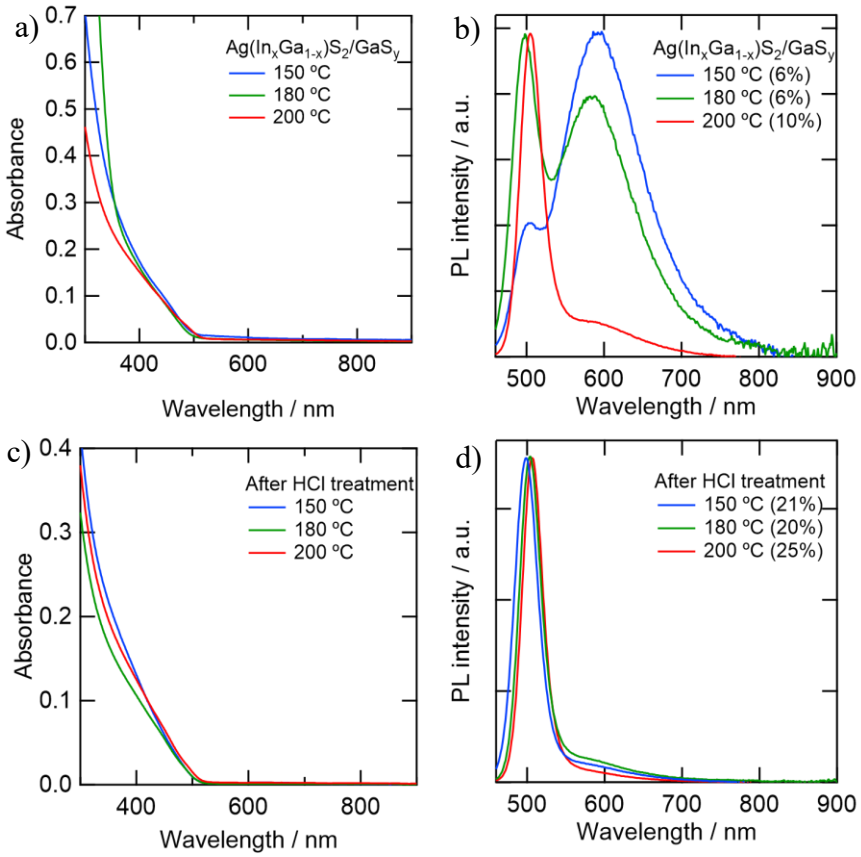

Figure 3-6 (a) UV-vis and (b) PL spectra of the corresponding QDs after the formation of GaS_y shell. (c) UV-vis and (d) PL spectra after the heat treatment with HCl. The vertical scales of the PL spectra were normalized at the highest positions. The PLQY values were displayed in each figure in parentheses.

The heat treatment of chalcogenide semiconductors in the presence of chloride has occasionally been reported as a method for improving the photovoltaic performance of CdTe-based solar cells. It was first applied to the CdTe layers produced by vapor deposition,[111,112] and afterward to the deposit of colloidal CdTe nanoparticles,[113] both of which reported similar performance improvements. Although multiple mechanisms have been proposed, such as doping, recrystallization, and grain boundary modification, a close analysis revealed that the grain boundary passivation by incorporating chlorides was a key factor in improving the cell performance.[114] In view of the surface treatment, chloride anion is classified as X-type in Green's classification of ligands.[115] It can also become Z-type, i.e., $GaCl_3$, when bound to the redundant gallium(III) species that is expected to be present in the gallium-rich reaction mixture for shell synthesis (DMTU is less than 1.5 equivalent of $Ga(acac)_3$. According to previous reports, several Z-type ligands improve the PL intensity of chalcogenide and

phosphide QDs.[116,117] We have also reported a significant improvement in the PL intensity of $AgIn_xGa_{1-x}S_2$ QDs after the treatment with zinc chloride ($ZnCl_2$).[118] However, in that study, $GaCl_3$ was ineffective on $AgIn_xGa_{1-x}S_2$ cores when mixed with these QDs and stored at an ambient temperature overnight.[118] The $GaCl_3$ treatment was also applied to $AgIn_xGa_{1-x}S_2/GaS_y$ core/shell QDs at different temperatures (25 °C and 280 °C, Figure 3-7). The results show that the band edge PL ratio and PLQY values increase when treated at a high temperature. Therefore, the mechanism of the chloride treatment appears to involve reactions beyond surface passivation, seemingly including the diffusion of chloride ions into the GaS_y shell. This reaction promotes the rearrangement of the elements at the core/shell boundary, thereby passivating the electronic trap states.

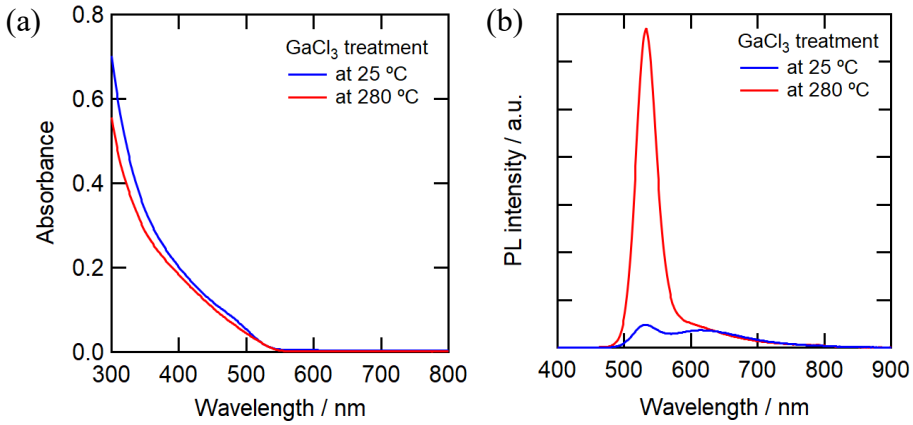

Figure 3-7 (a) UV–vis and (b) PL spectra of $AgIn_xGa_{1-x}S_2/GaS_y$ core/shell QDs after stirring in the presence of $GaCl_3$ at 25 °C for 2h and at 280°C for 30 min. PLQYs of each sample were 13% (25 °C) and 54% (280 °C). The PL spectra are standardized with PLQY values.

3.3.3 Synthesis of $AgIn_xGa_{1-x}S_2$ core QDs by $InCl_3$ and PL peak shift (Sample 4–8)

As mentioned above, the core/shell QDs, whose cores were synthesized using $In(OAc)_3$, exhibit the band-edge PL at ~500 nm. Since the wavelength region of the ideal green for display application is around 530 nm, I attempted the redshift by increasing the In-to-Ga ratio. However, changing the molar ratio of $In(OAc)_3/Ga(DDTC)_3$ hardly changed the bandgap of the QDs under the injection method. In several attempts, I replaced the indium source ($In(OAc)_3$) with $InCl_3$ or a mixture of $InCl_3$ and $In(DDTC)_3$, which successfully varied the PL

peak wavelength after the GaS_y shell formation. Figure 3-8 shows the UV–vis and PL spectra of the $AgIn_xGa_{1-x}S_2$ core and $AgIn_xGa_{1-x}S_2/GaS_y$ core/shell QDs synthesized under different conditions. Interestingly, some parts of the samples exhibit band-edge emissions, either as distinct peaks or shoulders, before the formation of the GaS_y shells (Figure 3-8b), which will be discussed below in relation to the core formation mechanism. From these samples, the chloride source for the post-synthetic treatment was changed from the HCl aqueous solution to an OLA solution of $GaCl_3$ to prevent the possible damage to the shell by water and acid, whereas the materials for GaS_y shell was identical. Because the dehydration process is unnecessary, the $GaCl_3$ solution may be injected into the core/shell QD solution without cooling down, which simplifies the experimental procedures.

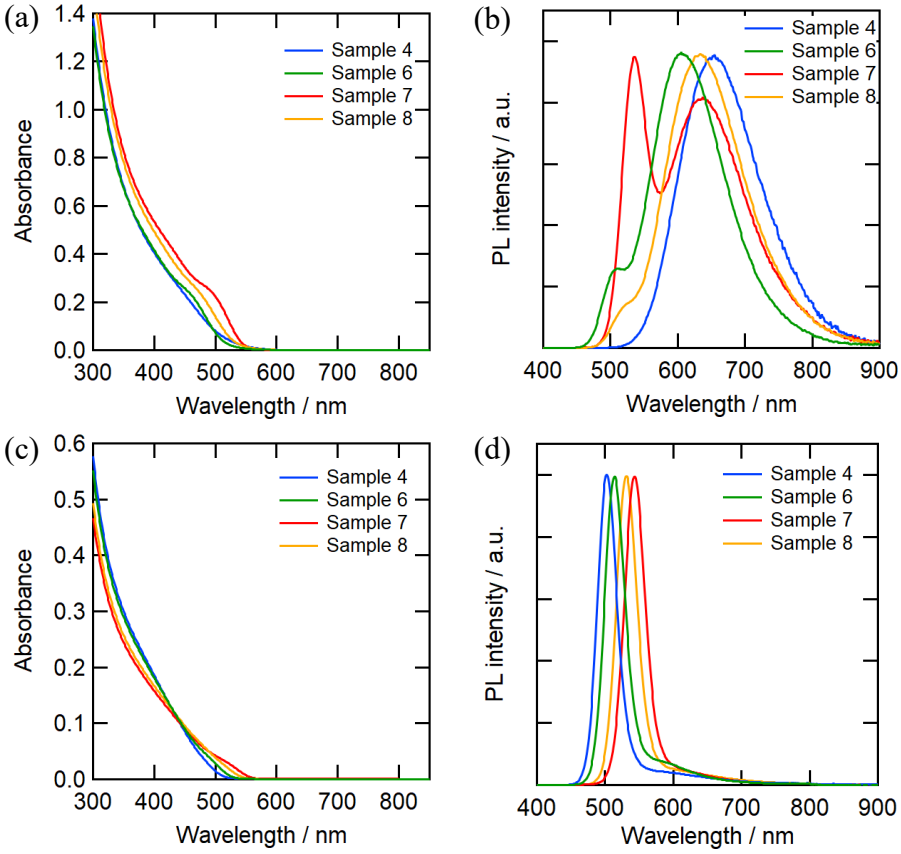

Figure 3-8 (a) UV–vis and (b) PL spectra (Ex = 350 nm) for the $AgIn_xGa_{1-x}S_2$ core synthesized under different conditions. In/Ga ratios of each sample were 0.375 (sample 4), 0.714 (sample 6), and 1.0 (samples 7 and 8), but sample 8 partly uses $In(DDTC)_3$ as the indium source. Experimental details are listed in **Table 3-1**. (c) UV–vis and (d) PL spectra of corresponding QDs after GaS_y shell formation and treatment with $GaCl_3$. Intensities of PL spectra are normalized at the highest positions.

The PL peak wavelengths of the core/shell QDs strongly depend on the In-to-Ga ratios of the materials used in the core synthesis (Figure 3-8d and 3-9a). However, even after optimizing the $GaCl_3$ treatment conditions, the PLQY values apparently decrease with the blue-shifting of the band-edge PL (Figure 3-9b**)**. According to the Ga_2S_3 bandgap in the bulk state (2.8 eV), the band offsets between the $AgIn_xGa_{1-x}S_2$ core and the GaS_y shell, which is essential to maintain the type I band alignment, become insufficient as the core bandgap increases. The highest PLQY value (75%) occurs at 543 nm, whereas it decreases to 25% for the QDs of the peak at 503 nm. The full-width at half maximum (FWHM) values of the band-edge PL obtained by the developed procedures demonstrated values of 33–37 nm, which are equivalent to the record-narrow values for the green-emitting InP core/shell QDs.[72] Furthermore, the spectra were distinctly narrower than those of our previous $AgIn_xGa_{1-x}S_2/GaS_y$ core/shell QDs prepared with the mixture precursor (FWHM = 42 nm at 517 nm).[77] Since the In-to-Ga ratio determines the PL wavelength, the narrow PL spectra indicate that the Ag source injection approach is suitable for obtaining compositionally uniform $AgIn_xGa_{1-x}S_2$ core QDs.

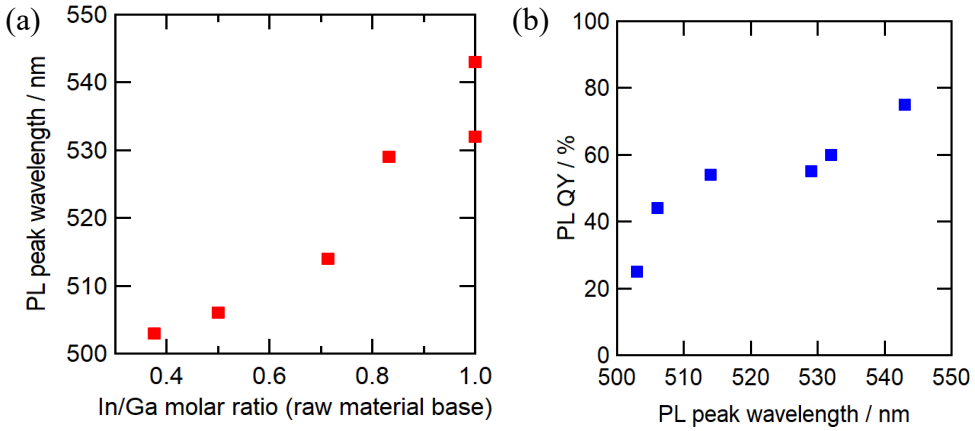

Figure 3-9 (a) PL peak wavelength of $AgIn_xGa_{1-x}S_2/GaS_y$ core/shell QDs as a function of In-to-Ga ratio, and (b) PLQY values as a function of PL peak wavelengths. In/Ga = 1.0 contains two data points corresponding to samples 7 and 8. Sample 8 uses $In(DDTC)_3$ as part of the indium sources.

3.3.4 Formation mechanism of $AgIn_xGa_{1-x}S_2$ core QDs

For the discussion of $AgIn_xGa_{1-x}S_2$ QD generation, the solutions were sampled for analysis at several reaction periods after the injection of Ag(OAc); 130 °C, 160 °C, and several times after reaching 200 °C. The colorless solution instantaneously changed to black upon

injection of Ag(OAc), suggesting the rapid nucleation of Ag_2S. According to the literature, metal–DDTC complexes activated by amines produce metal sulfides very efficiently by releasing thiocyanate derivatives.[119]

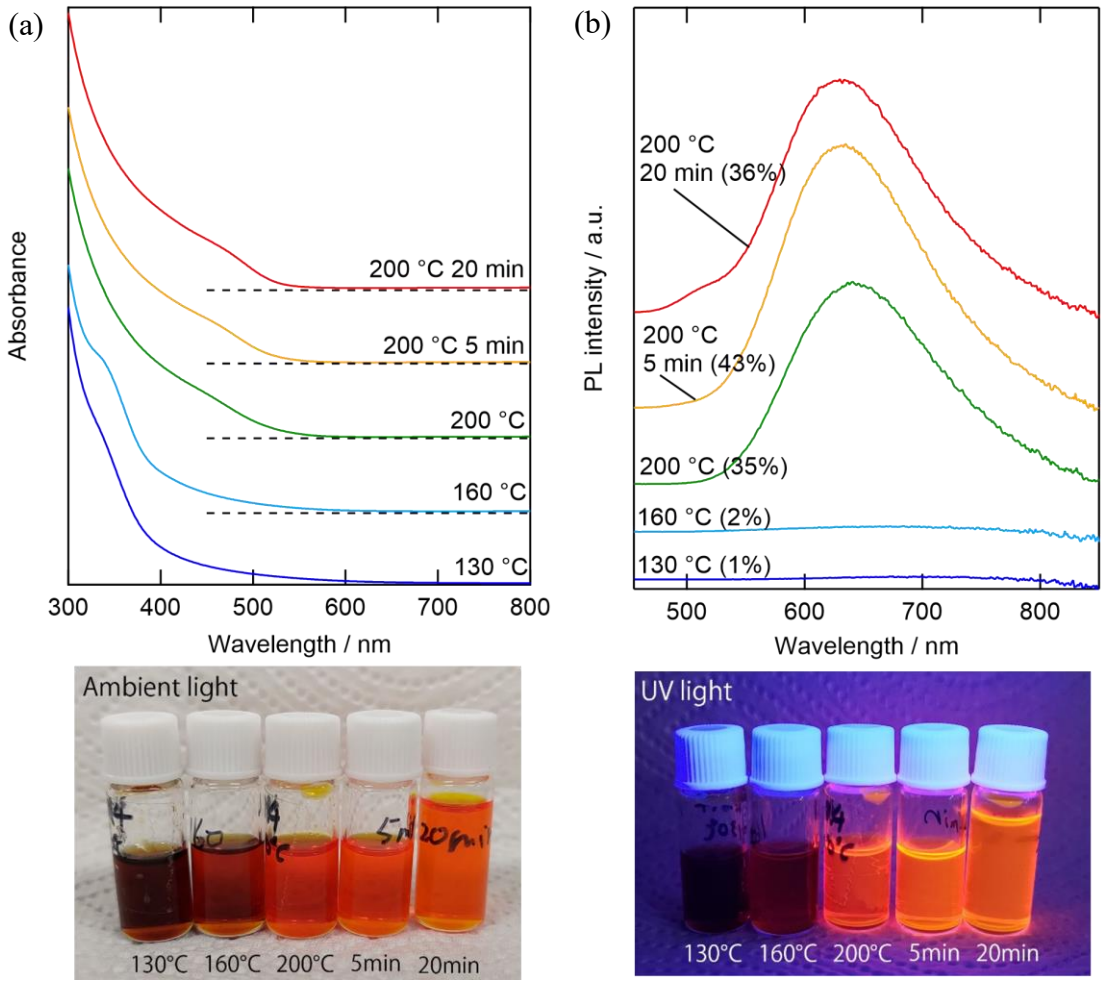

Figure 3-10 (a) UV-vis and (b) PL spectra of nanoparticles sampled intermittently during synthesis; immediately after the injection of $Ag(OAc)_3$ (130 °C), 160 °C, 200 °C, 5 min, and 20 min after reaching 200 °C. The PLQY values are displayed in each figure in parentheses. Photographs of the corresponding samples under ambient light and UV irradiation (as-prepared OLA solution) are shown below the spectra. The synthesis conditions are the same as for sample 8 in Table 3-1.

It is reasonable to consider that $Ga(DDTC)_3$, whose Ga–S bonds were partially dissociated at 130 °C, forms free ligands, which make a complex with the injected Ag^+. In fact, the solutions sampled at 130 °C and 160 °C were colored brown and hardly luminescent (Figure

3-10). The absorption tails ranging >700 nm are peculiar to Ag_2S nanoparticles whose bandgap in the bulk state is 1.3 eV. However, the XRD patterns of the corresponding samples did not indicate the presence of crystalline Ag_2S (Figure 3-11). The broad peaks at 29° and 48° are unexpectedly similar to the features of indium gallium alloy sulfide, whereas their In-to-Ga ratio might differ from the reference ($In_{1.5}Ga_{0.5}S_3$). Compositionally, the nanoparticles at 130 °C and 160 °C contained a significant amount of Ag and more than 1.5 equivalents of S with respect to In + Ga (Table 3-2). Therefore, it is reasonable to consider that the nanoparticles contain non-crystalline silver sulfide and crystalline indium gallium sulfide as part of the components. The TEM images of the samples at 130 °C and 160 °C show interconnected particle-like objects, which make size evaluation difficult (Figure 3-12a and b). Although the raw materials are often depleted after instantaneous nucleation, which triggers Ostwald ripening (a particle growth mechanism for growing larger particles by dissolving smaller particles to produce polydisperse particles), this growing mode does not appear to occur.[120,121]

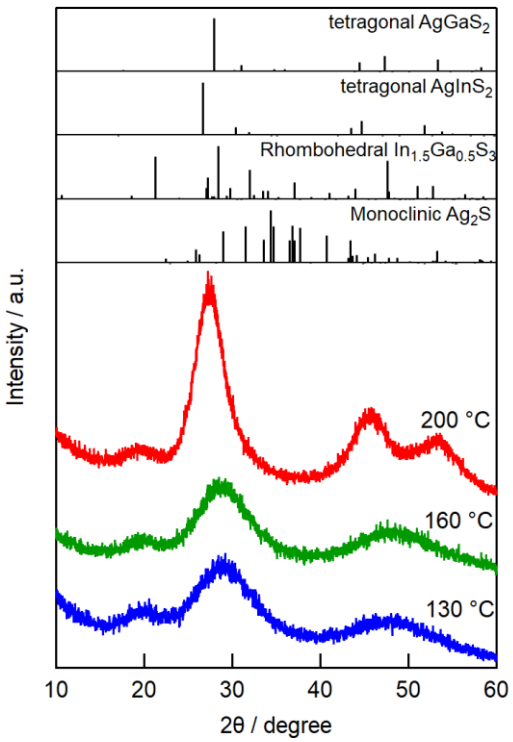

Figure 3-11 XRD patterns of nanoparticles sampled intermittently during synthesis; at 130 °C, 160 °C, and 200 °C. The reference data were obtained from ICSD 070-5629 ($AgInS_2$), ICSD 073-1233 ($AgGaS_2$), ICSD 077-0490 (rhombohedral $In_{1.5}Ga_{0.5}S_3$), and ICSD 080-5476 (monoclinic Ag_2S).

Table 3-2 Composition ratios calculated from ICP–AES data (Ag = 1).

	Ag	**In**	**Ga**	**S**
130 °C	1.00	0.86	0.90	3.50
160 °C	1.00	0.75	0.90	3.19
200 °C	1.00	1.09	1.04	4.23

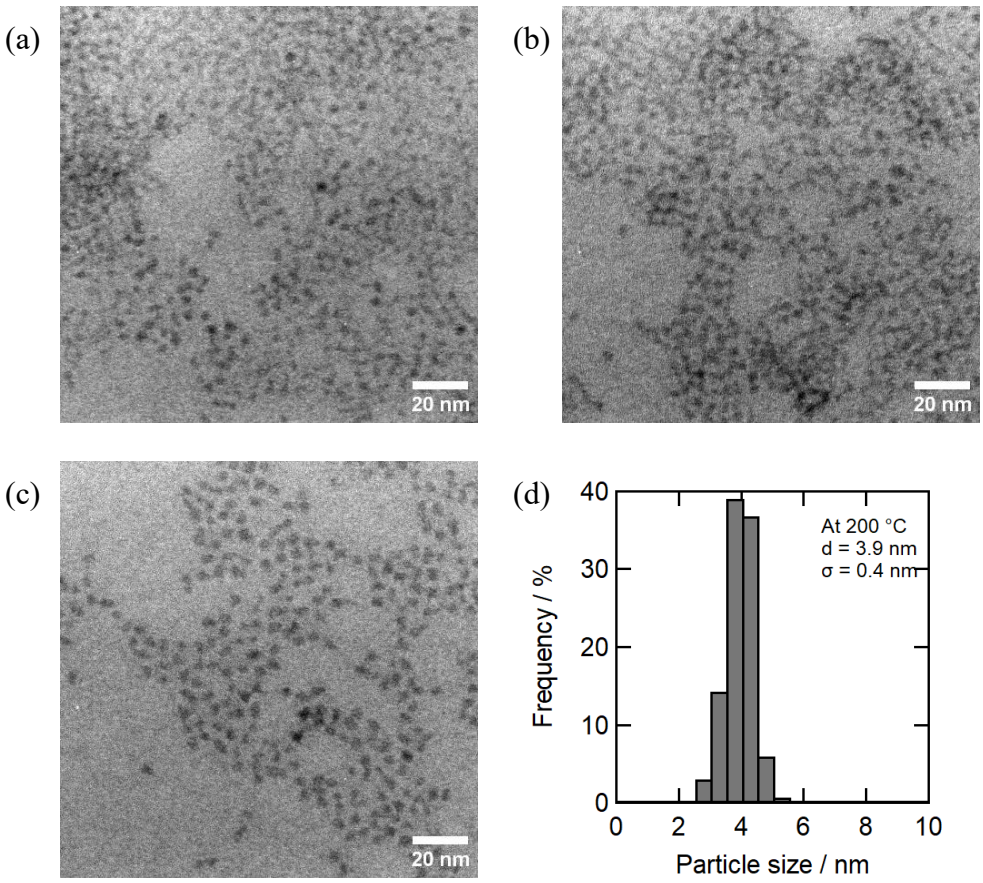

Figure 3-12 TEM images of nanoparticles sampled intermittently during synthesis; at (a) 130 °C, (b) 160 °C, and (c) 200 °C (0 min). (d) Size histogram of the particles at 200 °C (0 min). At 130 °C and 160 °C, particle sizes were not measurable due to severe interparticle linkage.

The absence of the Ostwald process is considered to be due to the deposit of indium gallium sulfide on the preformed Ag_2S nanoparticles, which acts as a barrier to growth. As the reaction temperature increases, the black solution gradually changes to red, which can be confirmed spectrally as the blueshift of the absorption tails (Figure 3-10a). Concomitantly, the

orange-colored PL appears, and its intensity was strengthened during annealing at the highest temperature (200 °C) (Figure 3-10b). These phenomena indicate that $AgIn_xGa_{1-x}S_2$ QDs were formed by alloying the central Ag_2S and $In_xGa_{1-x}S_{1.5}$ deposit (Figure 3-13), as supported by the XRD pattern (Figure 3-11). The TEM image of the 200 °C sample shows nanoparticles more clearly and independently than those sampled at the lower temperatures (Figure 3-12c), and the particle size at this stage is already almost the same as the core QDs after heating for 20 min. As anticipated from the composition analyses, the In-to-Ga ratio of the $AgIn_xGa_{1-x}S_2$ QDs, which determines the bandgap, is mostly determined before the alloying, i.e., at the stage of $Ag_2S/In_xGa_{1-x}S_{1.5}$ core/shell-like structure (Table 3-2). Therefore, the controllability and uniformity of the deposit composition are significantly important, which seems to be why wavelength tuning was successful by replacing $In(OAc)_3$ with $InCl_3$. The presence of the free ligands at the injection temperature of Ag(OAc) (130 °C) anticipates the ligand exchange between the complexes. Perhaps, $InCl_3$ is more favorably ligand-exchanged with $Ga(DDTC)_3$ than $In(OAc)_3$, generating partially substituted complexes of $InCl_2(DDTC)$ or $InCl(DDTC)_2$ and their gallium derivatives. However, the necessity to use $In(DDTC)_3$ as part of the indium source (samples 8 and 9) was unclear at this stage, and it may give a wider choice for the bandgap tuning because this approach allows setting the amount of DDTC independent of the In-to-Ga ratio.

Since the amount of In + Ga in the raw materials is higher than that of Ag, the indium gallium alloy sulfide deposits excessively with respect to the amount of Ag_2S, which is evident in the composition ratio at 130 °C and 160 °C before alloying occurs. The expected reaction equation, $Ag_2S + 2In_xGa_{1-x}S_{1.5} \rightarrow 2Ag(In_xGa_{1-x})S_2$, predicts that some deposits of indium gallium alloy sulfide remain after Ag_2S is completely transformed into $AgIn_xGa_{1-x}S_2$. Because InS_y shell is effective for generating band-edge PL,[28] this core/shell-like structure is thought to be responsible for the narrow shoulder peak in the PL spectrum of the core QD (Figure 3-8b). While stoichiometry based on raw material has not yet been achieved, a major advantage over our recent study is the absence of black–brown precipitates. This simplified the post-synthetic purification and improved the product yield from 15% (previously) to 60% (on the basis of Ag). Contrary to the general strategies based on suppressing Ag reactivity, this method accelerated

the Ag_2S formation by an instantaneous injection of the Ag(I) into a solution of $Ga(DDTC)_3$ heated at 130 °C. At this temperature, $Ga(DDTC)_3$ is expected to produce free *N,N'*-diethyldithiocarbamate (DDTC), which works as an efficient sulfur source.

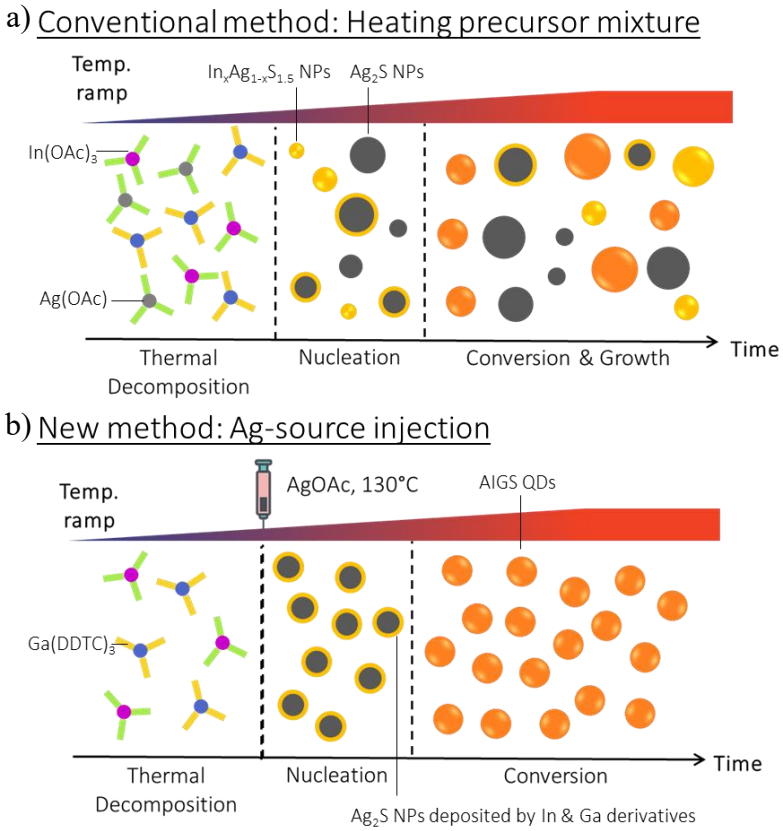

Figure 3-13 Schematic illustrations of the synthesis of $Ag(In_xGa_{1-x})S_2$ QDs: (a) heating of precursor mixture (previous study) and (b) Ag source injection (present study). Practically, In and Ga sources were introduced as dithiocarboxylate complexes, chloride, or acetate, which seemed partially dissociated or the ligands exchanged with one another. For simplicity of the schemes, they appeared as individual elements, but I consider that the bonding between groups 13 and 16 elements accelerates the reaction.

3.3.5 Structural characterization of core/shell QDs

Figure 3-14a shows the XRD patterns of the core, core/shell QDs, and the samples after the $GaCl_3$ treatment. As with Figure 3-11 at 200 °C, the cores' peaks are located between $AgInS_2$ and $AgGaS_2$, both in the tetragonal phase. A remarkable point in the core/shell QDs' spectrum (before the $GaCl_3$ treatment) is the sharp peak at 20.8°, which had occasionally

appeared when the DDTC complexes were used. The peak was previously assigned to the decomposition product.[118] Actually, the sample in this stage is stickier in a dry state than in the other two stages (core and after the $GaCl_3$ treatment) despite the repeated purification steps for analysis using acetone and hexane. The existence of impurities, which may be bound chemically on the QDs, is predictable from the X-ray photoelectron spectroscopy (XPS) result (Figure 3-14 b–g), showing minimal signals of Ag and In compared with Ga (the estimated compositions are listed in Table 3-3). Additionally, the peak position of Ga 2p, as well as Ga 3d, of the core/shell sample shifts to lower energy (higher electron density) compared with that of the core and $GaCl_3$-treated core/shell samples, and the position (1115.7 eV) is rather close to that of $Ga(DDTC)_3$ (1115 eV).[77] These results suggest that the core/shell QDs before $GaCl_3$ treatment were covered with an adlayer whose thickness is comparable to the analysis depth of XPS. The layer comprising gallium, sulfur, and probably carbon is indicated by a higher carbon content of the core/shell QDs (77 atomic%) than that of the core (60 atomic%) and $GaCl_3$-treated QDs (69 atomic%) (Table 3-4). Chlorine was not detected after the $GaCl_3$ treatment, supporting our perceptions that this treatment involves reactions more than surface passivation, but a structural change. The $GaCl_3$ treatment mostly dissipates the peak at ~20.8° in the XRD pattern, decreases the Ga and S contents (Table 3-3), and recovers the apparent Ag content by removing the adlayer. Although the Ag content in the XPS result is slightly higher than expected, it may be due to the spatial distribution of each element. The inductively coupled plasma atomic emission spectroscopy (ICP-AES) analysis of the same sample (after the $GaCl_3$ treatment, isolated and mineralized by concentrated HNO_3) reveals a value that can be interpreted as $Ag(In_{0.45}Ga_{0.55})S_2/Ga_{0.65}S_{0.84}$ if each element is distributed according to the formal composition (Table 3-5).

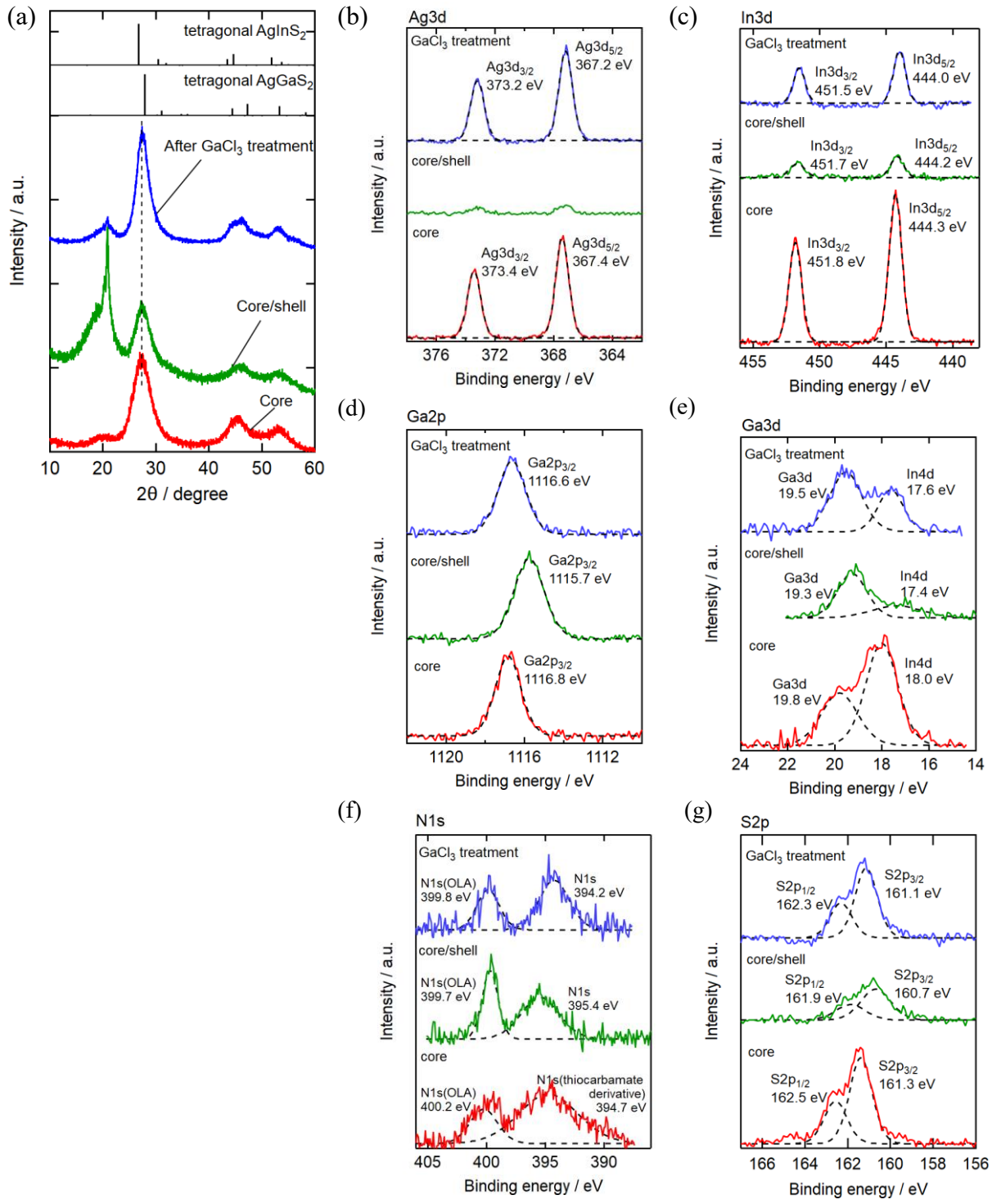

Figure 3-14 (a) XRD patterns and (b)–(g) XPS spectra of $AgIn_xGa_{1-x}S_2$ core and $AgIn_xGa_{1-x}S_2/GaS_y$ core/shell QDs, and samples after $GaCl_3$ treatment (sample 8 in Table 1) for (b) Ag 3d, (c) In 3d, (d) Ga 2p, (e) Ga 3d, (f) N 1s, and (g) S 2p regions. The reference data of the XRD patterns were obtained from ICSD 070-5629 and 073-1233 for $AgInS_2$ and $AgGaS_2$, respectively, both in the tetragonal phase.

The dashed lines in the XPS spectra are fitting curves by Voigt functions, and peak energies are displayed near the respective fitting curves.

Table 3-3 Composition ratios calculated from XPS data in atomic%.

	Ag	**In**	**Ga**	**S**
Core	21.2 (1.00)[a]	21.8 (1.03)	8.0 (0.377)	49.0 (2.31)
Core/shell	5.3 (1.00)	8.9 (1.68)	24.5 (4.62)	61.3 (11.6)
$GaCl_3$-treated	26.4 (1.00)	9.8 (0.371)	10.8 (0.409)	53.0 (2.01)

[a]Composition ratios (Ag = 1.00) were listed in parentheses.

Table 3-4 Composition ratios for all atoms detected in XPS in atomic%.

	Ag	**In**	**Ga**	**S**	**C**	**N**	**O**
Core	3.3	3.4	1.2	7.6	60.1	10.8	13.6
Core/shell	0.3	0.6	1.6	4.0	76.9	8.1	8.5
$GaCl_3$-treated	3.6	1.3	1.5	7.2	68.9	8.1	9.4

Chlorine was not detected even in $GaCl_3$-treated samples.

Table 3-5 Composition ratios (Ag = 1.00) deduced from ICP-AES measurements of purified samples.

	Ag	**In**	**Ga**	**S**
Core	1.00	0.98	0.85	3.35
Core/shell	1.00	0.99	6.29	11.40
$GaCl_3$-treated	1.00	0.45	1.20	2.84

The TEM and high-resolution TEM (HRTEM) images of the samples prepared from $Ga(DDTC)_3$, $InCl_3$, and $In(DDTC)_3$ (sample 8) are shown in Figure 3-15 and 3-16. Distinct particle images were obtained for all samples. The size and monodispersity of the cores remained (d = 4.1 nm, σ = 0.5 nm) despite changes in the raw materials from $In(OAc)_3$ to $InCl_3$. Unexpectedly, the size increment of the core/shell QDs before the $GaCl_3$ treatment is minimal

(0.4 nm, from 4.1 to 4.5 nm), whereas the reaction condition is the same as in recent reports, where a 0.5–1 nm-thick shell was applied. Probably, the surface structure of the core QDs prepared by the Ag source injection method differs from those prepared by all-mixed precursors, making adhesion difficult. Also, it may relate to the need for $GaCl_3$ treatment to obtain sufficient band-edge PL. Conversely, clear lattice fringes are observed at each stage in the HRTEM images. The presence of amorphous GaS_y shells is indicated by the amorphous annular dark areas around the crystalline cores, whose thickness is 0.5–1 nm for the $GaCl_3$-treated core/shell QDs.

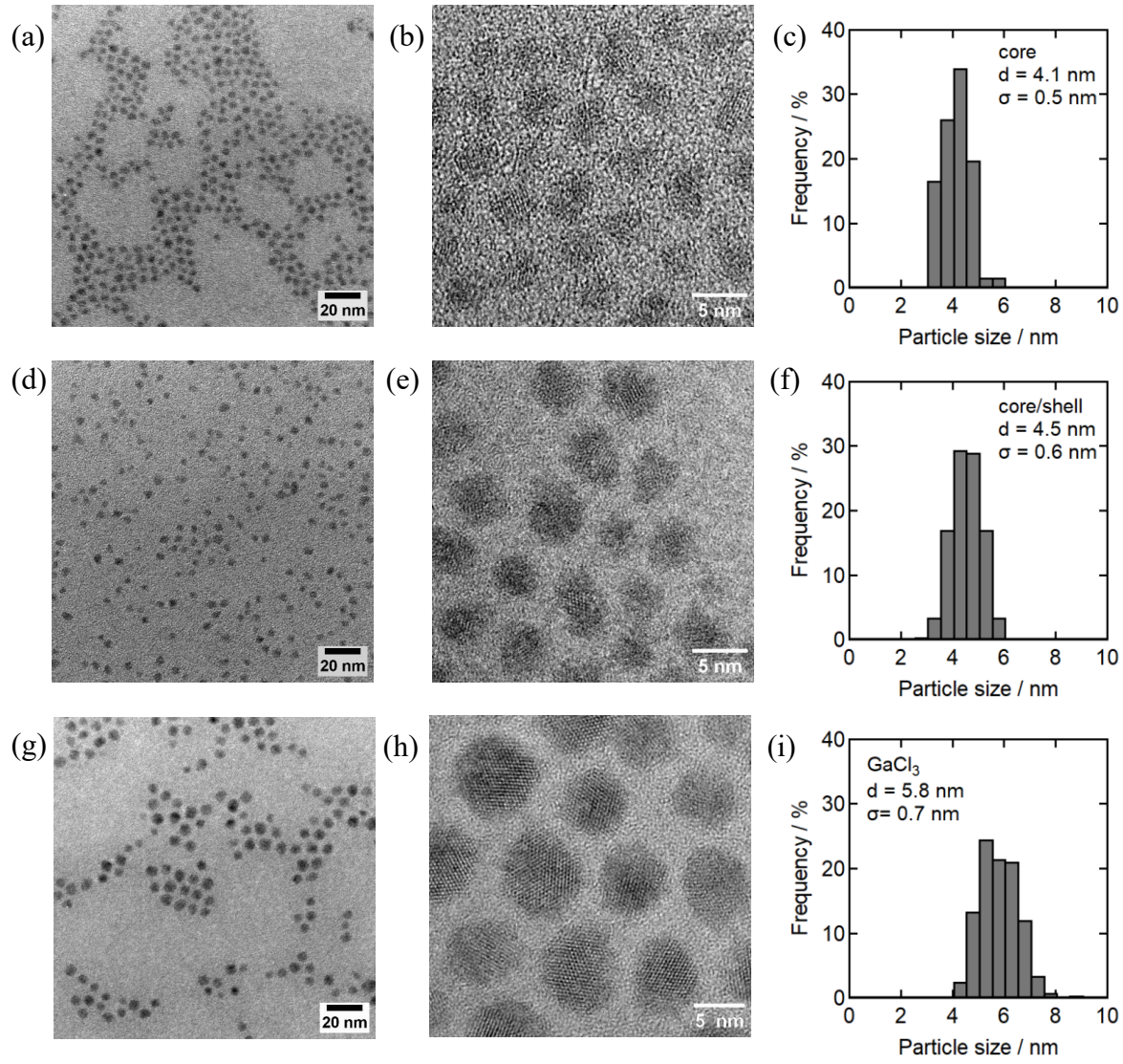

Figure 3-15 (a, d, g) TEM and (b, e, h) HRTEM images and size histogram of (a, b, c) $AgIn_xGa_{1-x}S_2$ core, (d, e, f) $AgIn_xGa_{1-x}S_2/GaS_y$ core/shell QDs, and (g, h, i) core/shell QDs after $GaCl_3$ treatment (sample 8 in Table 3-1). A higher magnification version of (h) is displayed in Figure 3-16.

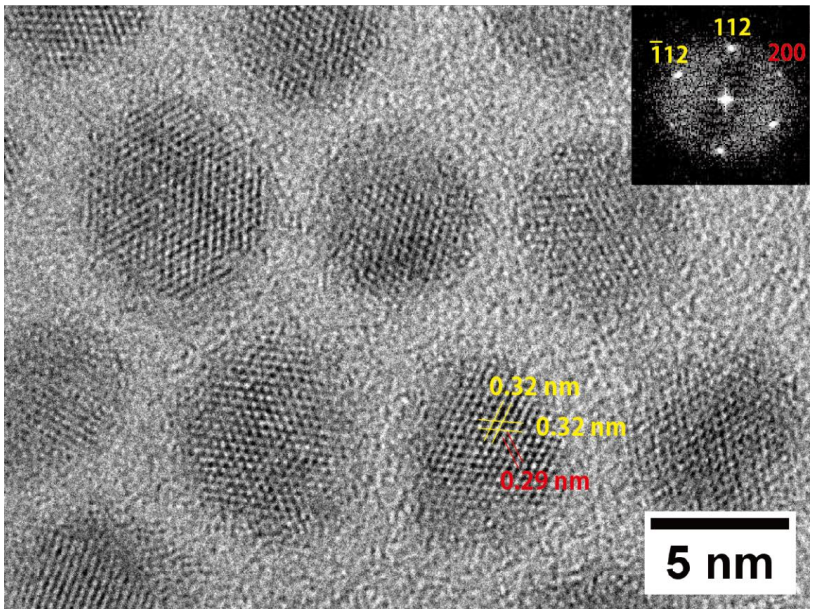

Figure 3-16 HRTEM image of $AgIn_xGa_{1-x}S_2/GaS_y$ core/shell QDs after $GaCl_3$ treatment (Sample 8 in Table 3-1) with d-spacings. The inset is the corresponding indexed fast Fourier transform (FFT) image.

The shell thickness is still smaller than that of typical CdSe and InP core/shell QDs, and it may be insufficient for carrier confinement considering the small band gap difference between $AgIn_xGa_{1-x}S_2$ core (2.34 eV corresponding to the PL peak at 530 nm) and GaS_y shell (2.8 eV in the bulk state) due to an expected broadening of wavefunction by tunneling effect. Therefore, there should be room for PL intensity improvement if the shell surface is more insulated. As the group I belong to have reported severally, alkylphosphines efficiently increase the band-edge PL by removing the sulfur-related electron-accepting sites and/or preferentially binding to the surface gallium sites.[28] Actually, an obvious increase in the PL intensity is captured by adding a small amount of TBP to the chloroform solution of the core/shell QDs after $GaCl_3$ treatment (Figure 3-17). When sample 8 (Table 3-1) is treated with TBP, the PLQY value increases from 60% to 77%. Sample 7 originally exhibited a PLQY value of 75% and was treated the same way; a near-unity PLQY value (99%) was achieved for the first time in this system. These results indicate the high potential as practical light conversion materials, as well as a narrow PL linewidth that is almost comparable with cadmium-based QDs. The increase in the PLQY value involves changes in the PL decay profiles (Figure 3-18). The $GaCl_3$-treated core/shell QDs exhibited two-lifetime components (51.5 ns and 187 ns), which was longer than our previous reports for the $AgIn_xGa_{1-x}S_2/GaS_y$ core/shell QDs synthesized by

heating mixture precursors (17 ns and 82 ns), suggesting a decrease in nonradiative transitions.[77] When the PLQY value increased from 58% to 74% (i.e., a 27% increase) by the TBP treatment, the two sets of lifetimes changed from 51.5 ns and 187 ns to 64.8 ns and 238 ns, corresponding to 25% and 27% increase from the as-prepared core/shell QDs, respectively (Table 3-6). Therefore, the increase in the PLQY by the TBP treatment can be attributed to the reduced nonradiative trap states. The minor variation in the contributions of the short- and long-lifetime components may be attributed to the insulating nature of the TBP ligand, which affects the wave function of an exciton.

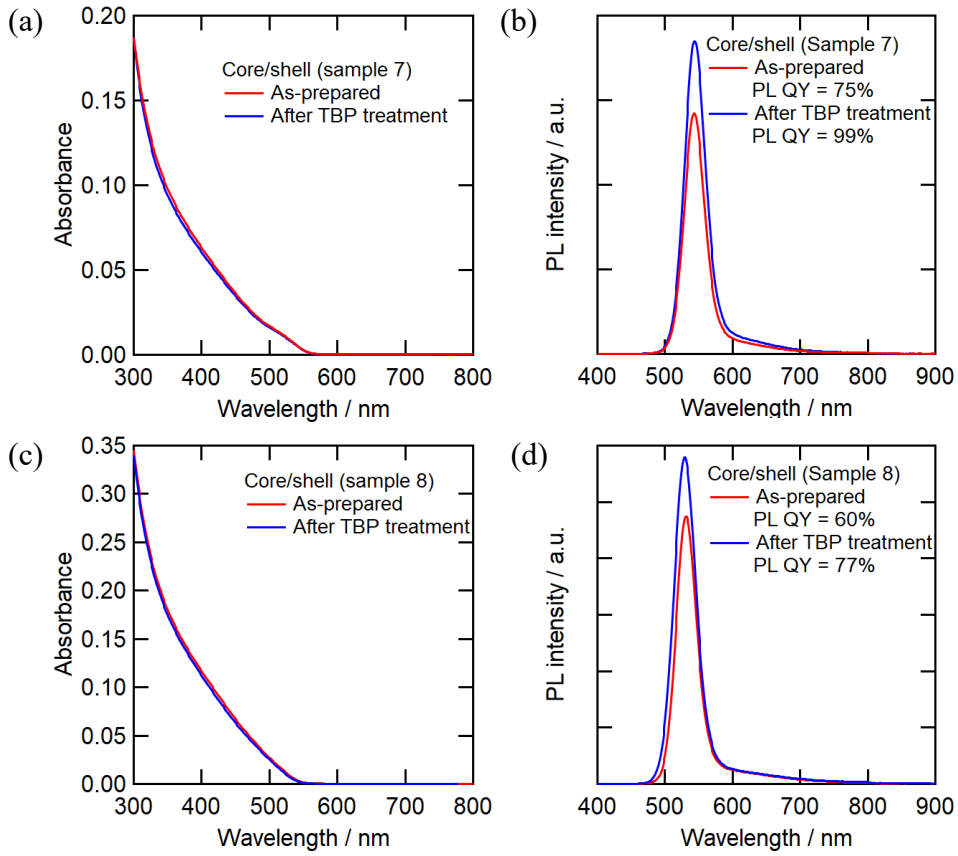

Figure 3-17 ((a) and (c)) UV–vis and ((b) and (d)) PL spectra (Ex = 350 nm) of $AgIn_xGa_{1-x}S_2/GaS_y$ core/shell QDs; (red) as-prepared and (blue) after TBP treatment. Figures (a) and (b) are the graphs for sample 7 and Figures (c) and (d) are for sample 8 in Table 3-1. Intensities of the PL spectra were standardized by the values of PLQY, which are indicated in each graph.

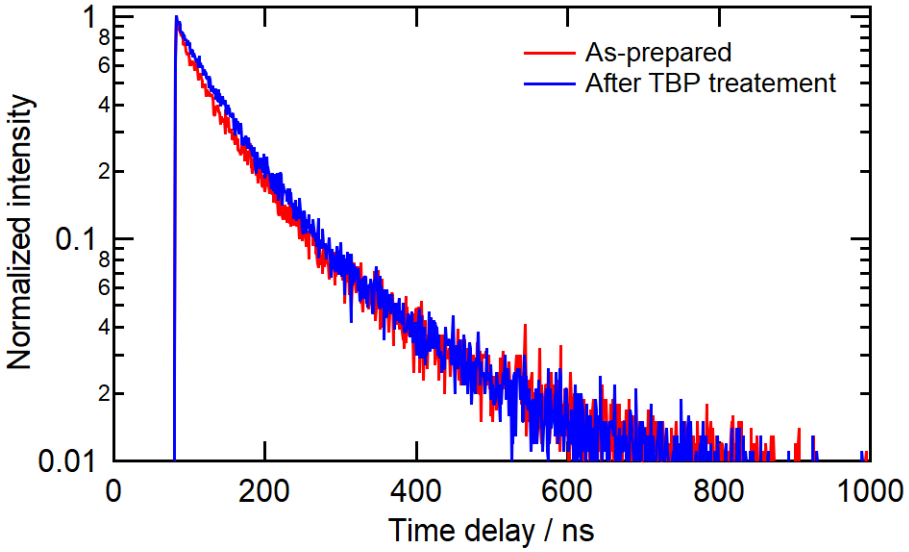

Figure 3-18 PL decay curves of $AgIn_xGa_{1-x}S_2/GaS_y$ core/shell QDs prepared by the same condition as sample 8 before and after the treatment with TBP measured at PL peak wavelength (533 nm) with the excitation at 405 nm. The value of PLQY was 58% (as-prepared) and 74% (after TBP treatment).

Table 3-6 Variations in PL lifetime components before and after TBP treatment (the data corresponding to Figure S11).

	A_1	τ_1/ns	A_2	τ_2/ns	χ^2
Core/shell	0.80	51.5	0.20	187	1.23
After TBP treatment	0.88	64.8	0.12	238	1.15

The curves were fitted with bi-exponential equation:

$$I(t) = A_1 \exp\left(-\frac{t}{\tau_1}\right) + A_2 \exp\left(-\frac{t}{\tau_2}\right)$$

where *I(t)* is the PL intensity at time *t*, A_1 and A_2 are amplitudes, and τ_1 and τ_2 are lifetimes.

3.3.6 Narrowing of PL peak width

Notably, sample 9 exhibited the narrowest FWHM (31 nm at 528 nm, 138 meV), which was narrower than that of sample 8 (35 nm at 532 nm, 153 meV) and even energetically narrower than that of sample 3 (31 nm at 507 nm, 150 meV) (Figure 3-19). In this attempt, a mixture of $Ga(DDTC)_3$ and $GaCl_3$ was used as the shell precursors for the shell in place of

$Ga(acac)_3$ and DMTU, which is considered to react more efficiently. However, when the core QDs were preliminarily mixed with $GaCl_3$, severe aggregation occurred at around 100 °C during heating. In this temperature region, the core QDs are not yet protected by the shell and can therefore be in direct contact with $GaCl_3$. This situation promoted Ostwald ripening, which was not noticeable when the $GaCl_3$ was added after shell formation as a post treatment. To address this issue, I injected the core QDs at a sufficiently high temperature (160 °C). At this temperature, the same ligand exchange is expected to occur between $Ga(DDTC)_3$ and $GaCl_3$ as occurred between $Ga(DDTC)_3$ and $InCl_3$ in the core synthesis, producing a partial substitute such as $Ga(DDTC)_2Cl$. These complexes are expected to bind to the core QDs more efficiently than $Ga(DDTC)_3$ because of the vacancy in the coordination sites. Due to the instantaneous protection by these activated shell precursors, the core QDs successfully maintained their morphology and composition to generate the narrowest PL spectrum. As proof of this argument, the FWHM was not narrowed (37 nm) when the same experimental procedures were applied with $Ga(acac)_3$ and DMTU (Figure 3-20). These results indicated that the order of introducing the reagents is not the sole factor, but that the characteristics of the Ga and S sources affect the protection of the cores. Although I have considered that the quantum size effect is not obvious in the $AgIn_xGa_{1-x}S_2$ system compared to that for CdSe and InP QDs, a recent paper reported PL peak shifts over 48 nm in $AgInS_2/GaS_y$ core/shell QDs when the core diameter was varied between 2.6 nm and 4.7 nm.[122] These results suggest that the size effect is not negligible for the cores around 4 nm, and thus the core size distribution should be as narrow as possible.

In contrast to the protective effect on the core, the use of chloride increased the size distribution of the core/shell QDs (1.4 nm, Figure 3-21) due to non-uniform shell growth (Figure 3-19d). On the other hand, the spectral FWHM of the band-edge PL becomes narrower. This trend is profoundly different from the CdSe- or InP-based QDs showing the PL peak shifts by the shell thickness.[123] I consider that the $AgInS_2$-based semiconductors are less amenable to quantum size effect, especially in the size region >5 nm, partly because their heavy hole mass reduces the exciton Bohr radius.[124–126] This feature seems favorable for controlling the bandgap by composition.

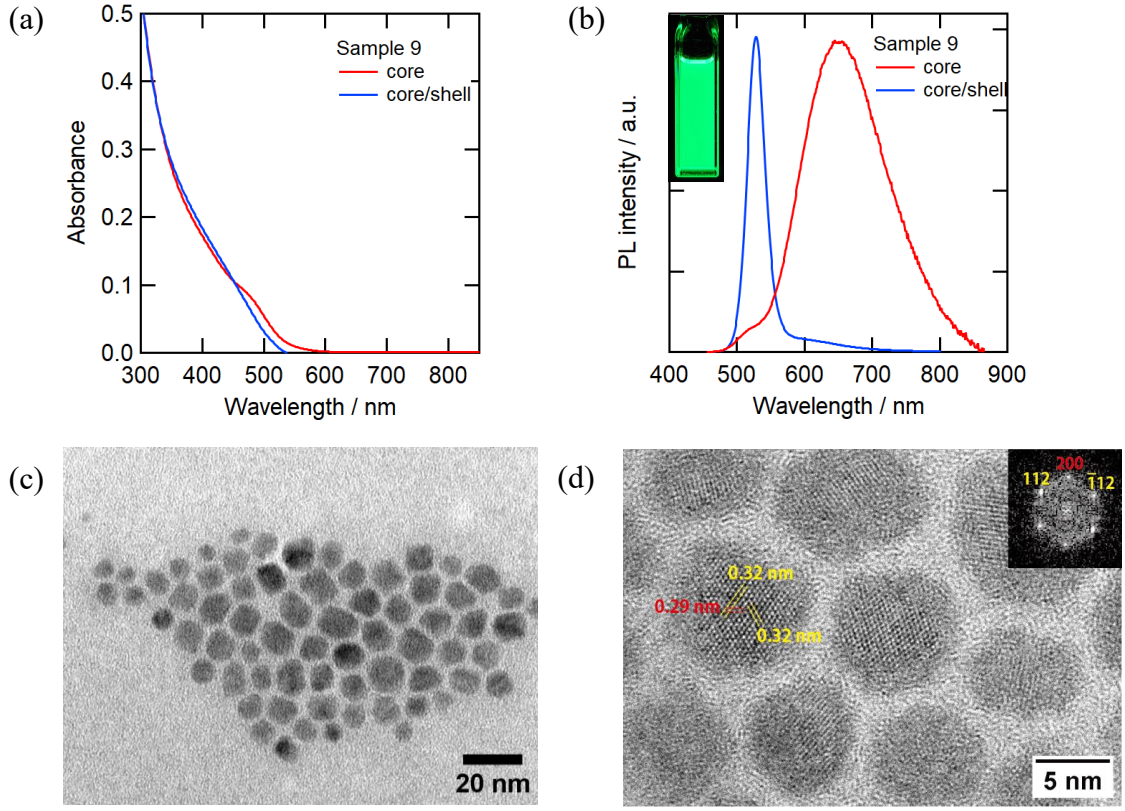

Figure 3-19 (a) UV–vis and (b) PL spectra (Ex = 390 nm) of (red) $AgIn_xGa_{1-x}S_2$ core and (blue) $AgIn_xGa_{1-x}S_2/GaS_y$ core/shell QDs synthesized under the condition for sample 9 in Table 3-1. (c) TEM and (d) HRTEM images of $AgIn_xGa_{1-x}S_2/GaS_y$ core/shell QDs with d-spacings and indexed fast Fourier transformation (FFT) image.

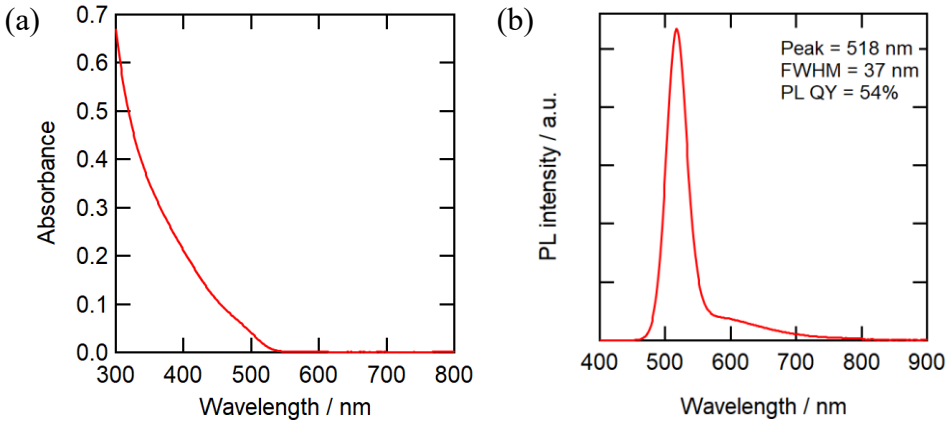

Figure 3-20 (a) UV-vis and (b) PL spectra (Ex = 390 nm) when the GaS_y shell is coated by using 0.15 mmol $Ga(acac)_3$, 0.15 mmol 1,3-dimethylthiourea (DMTU), and 0.05 mmol $Ga(DDTC)_3$ with $AgIn_xGa_{1-x}S_2$ cores injected at 160 °C. The cores were the same as that for sample 9 in Table 3-1.

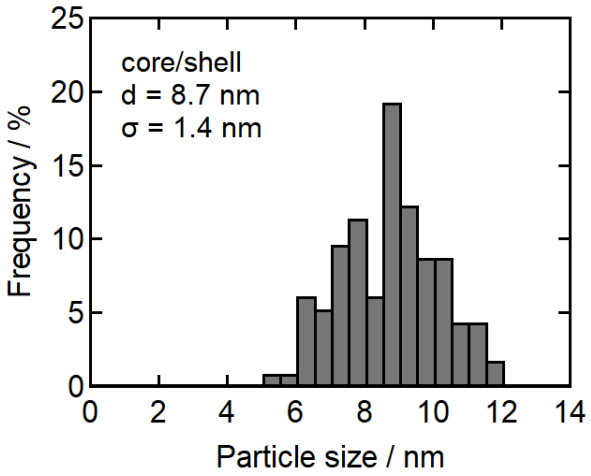

Figure 3-21 Size histograms of $AgIn_xGa_{1-x}S_2/GaS_y$ core/shell QDs synthesized using a mixture of $Ga(DDTC)_3$ and $GaCl_3$ (sample 9 in Table 3-1) corresponding to Figure 3-19.

3.4 Conclusion

Monodispersed $AgIn_xGa_{1-x}S_2$ quaternary QDs have been synthesized by a new approach utilizing the injection of an Ag precursor. In this strategy, the difference in the reactivity of groups 11 and 13 elements with chalcogen sources was overcome by temporally separating the two reactions: first, rapid nucleation of small Ag_2S nanoparticles, and second, the subsequent conversion to $AgIn_xGa_{1-x}S_2$ by alloying with In, Ga, and S. Remarkably, $AgIn_xGa_{1-x}S_2$ QDs could be generated without by-producing any precipitates. The product yield based on Ag was 60%, which significantly exceeds that of the previous approach performed by heating a mixture of the raw materials (5%–15%). After coating the $AgIn_xGa_{1-x}S_2$ nanoparticles with gallium sulfide (GaS_y) shells, the core/shell QDs exhibited an intense green-color band-edge emission with a tunable peak wavelength between 499 nm and 543 nm. Due to the prominent uniformity of the core nanoparticles in both size and composition, the FWHM of the band-edge emission was as small as 31 nm, and a near-unity PLQY value was demonstrated after the post-synthetic surface treatment. Both are record-high specifications among cadmium-free semiconductor QDs, indicating the high potential of the $AgIn_xGa_{1-x}S_2/GaS_y$ core/shell QDs as wavelength conversion materials in liquid crystal displays and micro light-emitting diode displays requiring high-color gamut.

Summary

In this dissertation, the PL performances of cadmium-free QDs including carbon dots and the groups 11–13–16 semiconductor QDs/GaS_y core/shell QDs were successfully improved utilizing surface modification approaches. The main results and conclusions of this study are summarized as follows:

In Chapter 1, it was described that a series of CDs were successfully synthesized by a solvothermal technique using citric acid and thiourea. After separation of each section by column chromatography, green and yellow CDs with average diameters of 8.3 and 7.0 nm, respectively, were obtained. Subsequent optical and structural characterizations indicated that the variation in the emission colour was caused by differences in surface functional groups rather than particle size. The photoelectrochemical properties were investigated by incorporating quinone derivatives and metal ions, which act as quenchers for the CDs. The photoluminescence quenching results showed the presence of anionic functional groups on the surface of the CDs. Furthermore, these functional groups interacted strongly with certain types of metal ions, suggesting that they could be used as metal ion sensors.

In Chapter 2, encapsulation of the $AgInS_2/GaS_y$ core/shell QDs in MOFs consisting of an indium fumarate ordered structure (InMOFs) was described. While damage to the shell may occur during the encapsulation reaction, the obtained composite retains a narrow band-edge emission that is nearly identical to the pristine $AgInS_2/GaS_y$ core/shell QDs with a PLQY of 12.6% after optimization of the precursor-solution pH. These encapsulation result allowed the spectral shape and PLQY of the composite to be maintained after 7 days, demonstrating the high stability of the QDs encapsulated in InMOFs.

In Chapter 3, development of a new method to synthesize AIGS QDs was described. This synthetic method utilized the high reactivity of silver ion with thiocarboxylate groups to promote the nucleation of Ag_2S. The preformed Ag_2S nanoparticles were subjected to the reaction with indium–gallium–sulfur species in situ

and then converted into the quaternary AIGS QDs without producing any precipitates. The product yield based on Ag was 60%, which is significantly higher than the method which was performed by heating the raw material mixture (5-15%).[77] The narrow band-edge emission was generated after GaS_y shell coating and the defect band emission was reduced by post-synthetic chloride treatment, which also resulted in an increase of PLQYs.

List of publications

1. Encapsulation of $AgInS_2/GaS_x$ core/shell quantum dots in In-fumarate metal–organic frameworks for stability

Manunya Tepakidareekul, Taro Uematsu*, Tsukasa Torimoto, and Susumu Kuwabata*

CrystEngComm, **2022,** *24*, 3715–3723

2. Synthesis of multicolor-emitting nitrogen–sulfur co-doped carbon dots and their photoelectrochemical studies for sensing applications

Manunya Tepakidareekul, Taro Uematsu*, and Susumu Kuwabata*

RSC Advances, **2022**, *12*, 20054–20061

3. Facile High-yield Synthesis of Ag–In–Ga–S Quaternary Quantum Dots and Coating with Gallium Sulfide Shells for Narrow Band-edge Emission

Taro Uematsu*, **Manunya Tepakidareekul**, Tetsuya Hirano, Tsukasa Torimoto, and Susumu Kuwabata*

Chem. Mater, **2023**, *35*, 1091–1106

References

1 Z. Yang, M. Gao, W. Wu, X. Yang, X. W. Sun, J. Zhang, H.-C. Wang, R.-S. Liu, C.-Y. Han, H. Yang and W. Li, *Materials Today*, 2019, **24**, 69–93.

2 A. I. Lakatos, *J Soc Inf Disp*, 2000, **8**, 1.

3 L. E. Brus, *J Chem Phys*, 1984, **80**, 4403–4409.

4 C. B. Murray, D. J. Norris and M. G. Bawendi, *J Am Chem Soc*, 1993, **115**, 8706–8715.

5 T. Lee, B. J. Kim, H. Lee, D. Hahm, W. K. Bae, J. Lim and J. Kwak, *Advanced Materials*, 2022, **34**, 2106276.

6 Y. Zhang, Y. Li and X.-P. Yan, *Small*, 2009, **5**, 185–189.

7 Y. Xia and C. Zhu, *Analyst*, 2008, **133**, 928–932.

8 A. M. Smith, H. Duan, A. M. Mohs and S. Nie, *Adv Drug Deliv Rev*, 2008, **60**, 1226–1240.

9 X. Xu, R. Ray, Y. Gu, H. J. Ploehn, L. Gearheart, K. Raker and W. A. Scrivens, *J Am Chem Soc*, 2004, **126**, 12736–12737.

10 S. Zhu, Y. Song, X. Zhao, J. Shao, J. Zhang and B. Yang, *Nano Res*, 2015, **8**, 355–381.

11 J. T. Margraf, V. Strauss, D. M. Guldi and T. Clark, *J Phys Chem B*, 2015, **119**, 7258–7265.

12 A. Cayuela, M. L. Soriano, C. Carrillo-Carrión and M. Valcárcel, *Chem. Commun.*, 2016, **52**, 1311–1326.

13 M. L. Liu, L. Yang, R. S. Li, B. Bin Chen, H. Liu and C. Z. Huang, *Green Chem.*, 2017, **19**, 3611–3617.

14 M. L. Liu, B. B. Chen, T. Yang, J. Wang, X. D. Liu and C. Z. Huang, *Methods Appl Fluoresc*, , DOI:10.1088/2050-6120/aa5e2b.

15 B. Bin Chen, R. S. Li, M. L. Liu, H. Z. Zhang and C. Z. Huang, *Chem. Commun.*, 2017, **53**, 4958–4961.

16 L. Bao, C. Liu, Z.-L. Zhang and D.-W. Pang, *Advanced Materials*, 2015, **27**, 1663–1667.

17 S. Qu, D. Zhou, D. Li, W. Ji, P. Jing, D. Han, L. Liu, H. Zeng and D. Shen, *Advanced Materials*, 2016, **28**, 3516–3521.

18 Y. Dong, H. Pang, H. Bin Yang, C. Guo, J. Shao, Y. Chi, C. M. Li and T. Yu, *Angewandte Chemie International Edition*, 2013, **52**, 7800–7804.

19 H.-X. Wang, J. Xiao, Z. Yang, H. Tang, Z.-T. Zhu, M. Zhao, Y. Liu, C. Zhang and H.-L. Zhang, *J. Mater. Chem. A*, 2015, **3**, 11287–11293.

20 D. Qu, M. Zheng, P. Du, Y. Zhou, L. Zhang, D. Li, H. Tan, Z. Zhao, Z. Xie and Z. Sun, *Nanoscale*, 2013, **5**, 12272–12277.

21 H. Ding, J.-S. Wei and H.-M. Xiong, *Nanoscale*, 2014, **6**, 13817–13823.

22 T. Torimoto, T. Adachi, K. Okazaki, M. Sakuraoka, T. Shibayama, B. Ohtani, A. Kudo and S. Kuwabata, *J Am Chem Soc*, 2007, **129**, 12388–12389.

23 T. Torimoto, T. Kameyama and S. Kuwabata, *J Phys Chem Lett*, 2014, **5**, 336–347.

24 M. J. Rao, T. Shibata, S. Chattopadhyay and A. Nag, *J Phys Chem Lett*, 2014, **5**, 167–173.

25 Y. Hamanaka, T. Ogawa, M. Tsuzuki and T. Kuzuya, *The Journal of Physical Chemistry C*, 2011, **115**, 1786–1792.

26 T. Ogawa, T. Kuzuya, Y. Hamanaka and K. Sumiyama, *J. Mater. Chem.*, 2010, **20**, 2226–2231.

27 S. L. Castro, S. G. Bailey, R. P. Raffaelle, K. K. Banger and A. F. Hepp, *J Phys Chem B*, 2004, **108**, 12429–12435.

28 T. Uematsu, K. Wajima, D. K. Sharma, S. Hirata, T. Yamamoto, T. Kameyama, M. Vacha, T. Torimoto and S. Kuwabata, *NPG Asia Mater*, 2018, **10**, 713–726.

29 L. Hu, C. Zhang, G. Zeng, G. Chen, J. Wan, Z. Guo, H. Wu, Z. Yu, Y. Zhou and J. Liu, *RSC Adv.*, 2016, **6**, 78595–78610.

30 J. Pan, D. Wan and J. Gong, *Chem. Commun.*, 2011, **47**, 3442–3444.

31 X. Kang, Y. Yang, L. Wang, S. Wei and D. Pan, *ACS Appl Mater Interfaces*, 2015, **7**, 27713–27719.

32 M. Tepakidareekul, T. Uematsu, T. Torimoto and S. Kuwabata, *CrystEngComm*, 2022, **24**, 3715–3723.

33 Y. Wang and A. Hu, *J. Mater. Chem. C*, 2014, **2**, 6921–6939.

34 B. De and N. Karak, *J. Mater. Chem. A*, 2017, **5**, 1826–1859.

35 W. U. Khan, D. Wang, W. Zhang, Z. Tang, X. Ma, X. Ding, S. Du and Y. Wang, *Sci Rep*, 2017, **7**, 14866.

36 H. Ding, Y. Ji, J.-S. Wei, Q.-Y. Gao, Z.-Y. Zhou and H.-M. Xiong, *J Mater Chem B*, 2017, **5**, 5272–5277.

37 Z. Qian, X. Shan, L. Chai, J. Ma, J. Chen and H. Feng, *ACS Appl Mater Interfaces*, 2014, **6**, 6797–6805.

38 M. A. Sk, A. Ananthanarayanan, L. Huang, K. H. Lim and P. Chen, *J Mater Chem C Mater*, 2014, **2**, 6954–6960.

39 M. Zhang, R. Su, J. Zhong, L. Fei, W. Cai, Q. Guan, W. Li, N. Li, Y. Chen, L. Cai and Q. Xu, *Nano Res*, 2019, **12**, 815–821.

40 E. Campbell, Md. T. Hasan, R. Gonzalez Rodriguez, G. R. Akkaraju and A. V Naumov, *ACS Biomater Sci Eng*, 2019, **5**, 4671–4682.

41 K. Jiang, X. Feng, X. Gao, Y. Wang, C. Cai, Z. Li and H. Lin, *Nanomaterials* , 2019, 9.

42 W. Shi, F. Guo, M. Han, S. Yuan, W. Guan, H. Li, H. Huang, Y. Liu and Z. Kang, *J. Mater. Chem. B*, 2017, **5**, 3293–3299.

43 S. Chandra, P. Patra, S. H. Pathan, S. Roy, S. Mitra, A. Layek, R. Bhar, P. Pramanik and A. Goswami, *J. Mater. Chem. B*, 2013, **1**, 2375–2382.

44 P. Ni, Q. Li, C. Xu, H. Lai, Y. Bai and T. Chen, *Appl Surf Sci*, 2019, **494**, 377–383.

45 D. Gao, Y. Zhang, A. Liu, Y. Zhu, S. Chen, D. Wei, J. Sun, Z. Guo and H. Fan, *Chemical Engineering Journal*, 2020, **388**, 124199.

46 Y. Zhang, P. Zhuo, H. Yin, Y. Fan, J. Zhang, X. Liu and Z. Chen, *ACS Appl Mater Interfaces*, 2019, **11**, 24395–24403.

47 S. Rai, B. K. Singh, P. Bhartiya, A. Singh, H. Kumar, P. K. Dutta and G. K. Mehrotra, *J Lumin*, 2017, **190**, 492–503.

48 P. Das, S. Ganguly, T. Agarwal, P. Maity, S. Ghosh, S. Choudhary, S. Gangopadhyay, T. K. Maiti, S. Dhara, S. Banerjee and N. C. Das, *Mater Chem Phys*, 2019, **237**, 121860.

49 X. Zhu, J. Wang, Y. Zhu, H. Jiang, D. Tan, Z. Xu, T. Mei, J. Li, L. Xue and X. Wang, *Microchimica Acta*, 2018, **185**, 510.

50 C. Ding, Z. Deng, J. Chen and Y. Jin, *Colloids Surf B Biointerfaces*, 2020, **189**, 110838.

51 Y. Chen, Y. Wu, B. Weng, B. Wang and C. Li, *Sens Actuators B Chem*, 2016, **223**, 689–696.

52 L. Sun, Y. Liu, Y. Wang, J. Xu, Z. Xiong, X. Zhao and Y. Xia, *Opt Mater (Amst)*, 2021, **112**, 110787.

53 Y. Sun, C. Shen, J. Wang and Y. Lu, *RSC Adv.*, 2015, **5**, 16368–16375.

54 X. Miao, X. Yan, D. Qu, D. Li, F. F. Tao and Z. Sun, *ACS Appl Mater Interfaces*, 2017, **9**, 18549–18556.

55 D. Qu, Z. Sun, M. Zheng, J. Li, Y. Zhang, G. Zhang, H. Zhao, X. Liu and Z. Xie, *Adv Opt Mater*, 2015, **3**, 360–367.

56 J. F. Moulder and J. Chastain, *Handbook of X-ray Photoelectron Spectroscopy: A Reference Book of Standard Spectra for Identification and Interpretation of XPS Data*, Physical Electronics Division, Perkin-Elmer Corporation, 1992.

57 F. Zu, F. Yan, Z. Bai, J. Xu, Y. Wang, Y. Huang and X. Zhou, *Microchimica Acta*, 2017, **184**, 1899–1914.

58 J. Lakowicz, *Principles of Fluorescence Spectroscopy*, 2006, vol. 1.

59 A. L. de Lacey, E. C. Hatchikian, A. Volbeda, M. Frey, J. C. Fontecilla-Camps and V. M. Fernandez, *J Am Chem Soc*, 1997, **119**, 7181–7189.

60 Dj. B. Raoof and S. M. Golabi, *Bull Chem Soc Jpn*, 1995, **68**, 2253–2261.

61 Y. Deng, J. Qian, Y. Zhou and Y. Niu, *RSC Adv.*, 2021, **11**, 10922–10928.

62 Q. Mei, Y. Shi, Q. Hua and B. Tong, *RSC Adv.*, 2015, **5**, 74924–74931.

63 N. R. Council, C. L. Sciences, B. E. S. Toxicology and C. C. D. Water, *Copper in Drinking Water*, National Academies Press, 2000.

64 P. M. Allen and M. G. Bawendi, *J Am Chem Soc*, 2008, **130**, 9240–9241.

65 T. Omata, K. Nose and S. Otsuka-Yao-Matsuo, *J Appl Phys*, 2009, **105**, 73106.

66 L. Li, A. Pandey, D. J. Werder, B. P. Khanal, J. M. Pietryga and V. I. Klimov, *J Am Chem Soc*, 2011, **133**, 1176–1179.

67 J. Park and S.-W. Kim, *J Mater Chem*, 2011, **21**, 3745–3750.

68 J.-H. Kim, D.-Y. Jo, K.-H. Lee, E.-P. Jang, C.-Y. Han, J.-H. Jo and H. Yang, *Advanced Materials*, 2016, **28**, 5093–5098.

69 C.-W. Chen, D.-Y. Wu, Y.-C. Chan, C. C. Lin, P.-H. Chung, M. Hsiao and R.-S. Liu, *The Journal of Physical Chemistry C*, 2015, **119**, 2852–2860.

70 L. Liu, R. Hu, W.-C. Law, I. Roy, J. Zhu, L. Ye, S. Hu, X. Zhang and K.-T. Yong, *Analyst*, 2013, **138**, 6144–6153.

71 M. Sandroni, K. D. Wegner, D. Aldakov and P. Reiss, *ACS Energy Lett*, 2017, **2**, 1076–1088.

72 D. A. Taylor, J. A. Teku, S. Cho, W.-S. Chae, S.-J. Jeong and J.-S. Lee, *Chemistry of Materials*, 2021, **33**, 4399–4407.

73 E. Jang, Y. Kim, Y.-H. Won, H. Jang and S.-M. Choi, *ACS Energy Lett*, 2020, **5**, 1316–1327.

74 Q. Ren, Y. Ma, S. Zhang, L. Ga and J. Ai, *ACS Omega*, 2021, **6**, 6361–6367.

75 H. He, Y. Lin, Z.-Q. Tian, D.-L. Zhu, Z.-L. Zhang and D.-W. Pang, *Small*, 2018, **14**, 1703296.

76 W. Hoisang, T. Uematsu, T. Yamamoto, T. Torimoto and S. Kuwabata, *Nanomaterials*, , DOI:10.3390/nano9121763.

77 W. Hoisang, T. Uematsu, T. Torimoto and S. Kuwabata, *Inorg Chem*, 2021, **60**, 13101–13109.

78 D. Yang, M. A. Ortuño, V. Bernales, C. J. Cramer, L. Gagliardi and B. C. Gates, *J Am Chem Soc*, 2018, **140**, 3751–3759.

79 E. Tsivion and M. Head-Gordon, *The Journal of Physical Chemistry C*, 2017, **121**, 12091–12100.

80 Y. Takashima, V. M. Martínez, S. Furukawa, M. Kondo, S. Shimomura, H. Uehara, M. Nakahama, K. Sugimoto and S. Kitagawa, *Nat Commun*, 2011, **2**, 168.

81 M. C. Das, Q. Guo, Y. He, J. Kim, C.-G. Zhao, K. Hong, S. Xiang, Z. Zhang, K. M. Thomas, R. Krishna and B. Chen, *J Am Chem Soc*, 2012, **134**, 8703–8710.

82 N. Zhang, D. Zhang, J. Zhao and Z. Xia, *Dalton Trans.*, 2019, **48**, 6794–6799.

83 J. Othong, J. Boonmak, V. Promarak, F. Kielar and S. Youngme, *ACS Appl Mater Interfaces*, 2019, **11**, 44421–44429.

84 D. Buso, J. Jasieniak, M. D. H. Lay, P. Schiavuta, P. Scopece, J. Laird, H. Amenitsch, A.

J. Hill and P. Falcaro, *Small*, 2012, **8**, 80–88.

85 L. Hamon, C. Serre, T. Devic, T. Loiseau, F. Millange, G. Férey and G. De Weireld, *J Am Chem Soc*, 2009, **131**, 8775–8777.

86 E. Stavitski, E. A. Pidko, S. Couck, T. Remy, E. J. M. Hensen, B. M. Weckhuysen, J. Denayer, J. Gascon and F. Kapteijn, *Langmuir*, 2011, **27**, 3970–3976.

87 T. K. Trung, P. Trens, N. Tanchoux, S. Bourrelly, P. L. Llewellyn, S. Loera-Serna, C. Serre, T. Loiseau, F. Fajula and G. Férey, *J Am Chem Soc*, 2008, **130**, 16926–16932.

88 J. Y. Kim, L. Zhang, R. Balderas-Xicohténcatl, J. Park, M. Hirscher, H. R. Moon and H. Oh, *J Am Chem Soc*, 2017, **139**, 17743–17746.

89 Y. Zhang, B. E. G. Lucier, S. M. McKenzie, M. Arhangelskis, A. J. Morris, T. Friščić, J. W. Reid, V. V Terskikh, M. Chen and Y. Huang, *ACS Appl Mater Interfaces*, 2018, **10**, 28582–28596.

90 K. Kumagai, T. Uematsu, T. Torimoto and S. Kuwabata, *CrystEngComm*, 2019, **21**, 5568–5577.

91 K. Kumagai, T. Uematsu, T. Torimoto and S. Kuwabata, *Chemistry of Materials*, 2021, **33**, 1607–1617.

92 D. C. J. Neo, C. Cheng, S. D. Stranks, S. M. Fairclough, J. S. Kim, A. I. Kirkland, J. M. Smith, H. J. Snaith, H. E. Assender and A. A. R. Watt, *Chemistry of Materials*, 2014, **26**, 4004–4013.

93 X. Dong, J. Xu, H. Yang, X. Zhang, Z. Mo, S. Shi, L. Li and S. Yin, *J Electron Mater*, 2018, **47**, 2241–2248.

94 P. L. Brown, J. Ellis and R. N. Sylva, *J. Chem. Soc.{,} Dalton Trans.*, 1982, 1911–1914.

95 B. Seoane, A. Dikhtiarenko, A. Mayoral, C. Tellez, J. Coronas, F. Kapteijn and J. Gascon, *CrystEngComm*, 2015, **17**, 1693–1700.

96 J. Yang, Q. Zhao, J. Li and J. Dong, *Microporous and Mesoporous Materials*, 2010, **130**, 174–179.

97 Y. Fang, J. Wen, G. Zeng, F. Jia, S. Zhang, Z. Peng and H. Zhang, *Chemical Engineering Journal*, 2018, **337**, 532–540.

98 W. Hoisang, T. Uematsu, T. Torimoto and S. Kuwabata, *Nanoscale Adv.*, 2022, **4**,

849–857

99 U. T. D. Thuy, N. Q. Liem, D. X. Thanh, M. Protière and P. Reiss, *Appl Phys Lett*, 2007, **91**, 241908.

100 U. T. D. Thuy, P. T. Thuy, N. Q. Liem, L. Li and P. Reiss, *Appl Phys Lett*, 2010, **96**, 73102.

101 M. V Artemyev, A. I. Bibik, L. I. Gurinovich, S. V Gaponenko and U. Woggon, *Phys. Rev. B*, 1999, **60**, 1504–1506.

102 A. Al Salman, A. Tortschanoff, M. B. Mohamed, D. Tonti, F. van Mourik and M. Chergui, *Appl Phys Lett*, 2007, **90**, 93104.

103 K. A. S. Usman, J. W. Maina, S. Seyedin, M. T. Conato, L. M. Payawan, L. F. Dumée and J. M. Razal, *NPG Asia Mater*, 2020, **12**, 58.

104 C. R. Marshall, S. A. Staudhammer and C. K. Brozek, *Chem. Sci.*, 2019, **10**, 9396–9408.

105 S. Turner, O. I. Lebedev, F. Schröder, D. Esken, R. A. Fischer and G. Van Tendeloo, *Chemistry of Materials*, 2008, **20**, 5622–5627.

106 C. Wiktor, S. Turner, D. Zacher, R. A. Fischer and G. Van Tendeloo, *Microporous and Mesoporous Materials*, 2012, **162**, 131–135.

107 W. Hoisang, T. Uematsu, T. Torimoto and S. Kuwabata, *Chem Lett*, 2021, **50**, 1863–1866.

108 H. Zhong, Y. Zhou, M. Ye, Y. He, J. Ye, C. He, C. Yang and Y. Li, *Chemistry of Materials*, 2008, **20**, 6434–6443.

109 T. Kameyama, M. Kishi, C. Miyamae, D. K. Sharma, S. Hirata, T. Yamamoto, T. Uematsu, M. Vacha, S. Kuwabata and T. Torimoto, *ACS Appl Mater Interfaces*, 2018, **10**, 42844–42855.

110 T. Uematsu, T. Doi, T. Torimoto and S. Kuwabata, *J Phys Chem Lett*, 2010, **1**, 3283–3287.

111 P. D. Paulson and V. Dutta, *Thin Solid Films*, 2000, **370**, 299–306.

112 M. D. G. Potter, D. P. Halliday, M. Cousins and K. Durose, *Thin Solid Films*, 2000, **361–362**, 248–252.

113 M. G. Panthani, J. M. Kurley, R. W. Crisp, T. C. Dietz, T. Ezzyat, J. M. Luther and D.

V Talapin, *Nano Lett*, 2014, **14**, 670–675.

114 J. D. Major, M. Al Turkestani, L. Bowen, M. Brossard, C. Li, P. Lagoudakis, S. J. Pennycook, L. J. Phillips, R. E. Treharne and K. Durose, *Nat Commun*, 2016, **7**, 13231.

115 M. L. H. Green, *J Organomet Chem*, 1995, **500**, 127–148.

116 N. Kirkwood, J. O. V Monchen, R. W. Crisp, G. Grimaldi, H. A. C. Bergstein, I. du Fossé, W. van der Stam, I. Infante and A. J. Houtepen, *J Am Chem Soc*, 2018, **140**, 15712–15723.

117 J. J. Calvin, J. K. Swabeck, A. B. Sedlak, Y. Kim, E. Jang and A. P. Alivisatos, *J Am Chem Soc*, 2020, **142**, 18897–18906.

118 W. Hoisang, T. Uematsu, T. Torimoto and S. Kuwabata, *Nanoscale Adv*, 2022, **4**, 849–857.

119 N. Hollingsworth, A. Roffey, H.-U. Islam, M. Mercy, A. Roldan, W. Bras, M. Wolthers, C. R. A. Catlow, G. Sankar, G. Hogarth and N. H. de Leeuw, *Chemistry of Materials*, 2014, **26**, 6281–6292.

120 S. G. Kwon and T. Hyeon, *Small*, 2011, **7**, 2685–2702.

121 J. Park, J. Joo, S. G. Kwon, Y. Jang and T. Hyeon, *Angewandte Chemie International Edition*, 2007, **46**, 4630–4660.

122 T. Thi Thu Huong, N. T. Loan, T. D. T. Ung, N. T. Tung, H. Han and N. Q. Liem, *Nanotechnology*, 2022, **33**, 355704.

123 L. Liu, R. Hu, W.-C. Law, I. Roy, J. Zhu, L. Ye, S. Hu, X. Zhang, K.-T. Yong, C.-W. Chen, D.-Y. Wu, Y.-C. Chan, C. C. Lin, P.-H. Chung, M. Hsiao, R.-S. Liu, J.-H. Kim, D.-Y. Jo, K.-H. Lee, E.-P. Jang, C.-Y. Han, J.-H. Jo, H. Yang, J. Park, S.-W. Kim, L. Li, A. Pandey, D. J. Werder, B. P. Khanal, J. M. Pietryga, V. I. Klimov, T. Omata, K. Nose, S. Otsuka-Yao-Matsuo, P. M. Allen and M. G. Bawendi, *J Am Chem Soc*, 2011, **28**, 6144–6153.

124 A. S. Baimuratov, I. V Martynenko, A. V Baranov, A. V Fedorov, I. D. Rukhlenko and S. Yu. Kruchinin, *The Journal of Physical Chemistry C*, 2019, **123**, 16430–16438.

125 J. Liu and E. Hua, *Mater Sci Semicond Process*, 2015, **40**, 446–452.

126 J. Liu, S. Chen, Q. Liu, Y. Zhu and Y. Lu, *Comput Mater Sci*, 2014, **91**, 159–164.

Acknowledgement

First and foremost, I would like to express my sincerest gratitude to my supervisor, Professor Susumu Kuwabata, Department of Applied Chemistry, Graduate School of Engineering, Osaka University for his invaluable guidance and support throughout my PhD. Thanks go to Kuwabata sensei for encouraging me to pursue a PhD and for giving me the opportunity to work within his research group, it really has been a precious experience. I would like to thank to Professor. Ken-ichi Nakayama and Professor Akinori Saeki for their reviewing this thesis with helpful comments and suggestions,

I would also like to express my special thanks to Associate Professor Taro Uematsu for his helpful guidance, encouragement, significant discussion throughout this work and kindly support in every way he can support me during my Ph.D. I would like to thank Professor Tetsuya Tsuda for his valuable suggestions and support. I would like to thank our secretaries, Ms, Miyuki Takahama and Ms. Michiko Ebukuro for their kind help and heartful supports for my laboratory life. A big thank you also goes to all Kuwabata laboratory members, both past and present, who have not only taught me so much but have also been great fun to work with.

Finally, I would like to thank my beloved Papa, Mama, Can, Grannies and all friends for the love, encouragement and support that helped me throughout all these years.

Manunya Tepakidareekul